
Dissertations, Theses, and Masters Projects

Theses, Dissertations, & Master Projects

1998

Wind interaction with buoyant plumes on the inner continental shelf

Sarah E. Rennie

College of William and Mary - Virginia Institute of Marine Science

Follow this and additional works at: <https://scholarworks.wm.edu/etd>



Part of the [Oceanography Commons](#)

Recommended Citation

Rennie, Sarah E., "Wind interaction with buoyant plumes on the inner continental shelf" (1998).
Dissertations, Theses, and Masters Projects. Paper 1539616822.
<https://dx.doi.org/doi:10.25773/v5-j584-ct28>

This Dissertation is brought to you for free and open access by the Theses, Dissertations, & Master Projects at W&M ScholarWorks. It has been accepted for inclusion in Dissertations, Theses, and Masters Projects by an authorized administrator of W&M ScholarWorks. For more information, please contact scholarworks@wm.edu.

INFORMATION TO USERS

This manuscript has been reproduced from the microfilm master. UMI films the text directly from the original or copy submitted. Thus, some thesis and dissertation copies are in typewriter face, while others may be from any type of computer printer.

The quality of this reproduction is dependent upon the quality of the copy submitted. Broken or indistinct print, colored or poor quality illustrations and photographs, print bleedthrough, substandard margins, and improper alignment can adversely affect reproduction.

In the unlikely event that the author did not send UMI a complete manuscript and there are missing pages, these will be noted. Also, if unauthorized copyright material had to be removed, a note will indicate the deletion.

Oversize materials (e.g., maps, drawings, charts) are reproduced by sectioning the original, beginning at the upper left-hand corner and continuing from left to right in equal sections with small overlaps. Each original is also photographed in one exposure and is included in reduced form at the back of the book.

Photographs included in the original manuscript have been reproduced xerographically in this copy. Higher quality 6" x 9" black and white photographic prints are available for any photographs or illustrations appearing in this copy for an additional charge. Contact UMI directly to order.

UMI

A Bell & Howell Information Company
300 North Zeeb Road, Ann Arbor MI 48106-1346 USA
313/761-4700 800/521-0600

WIND INTERACTION WITH BUOYANT PLUMES
ON THE INNER CONTINENTAL SHELF

A Dissertation Presented to
The Faculty of the School of Marine Science
The College of William and Mary in Virginia

In Partial Fulfillment of the Requirements
for the Degree of Doctor of Philosophy

by
Sarah E. Rennie
1998

UMI Number: 9823462

UMI Microform 9823462
Copyright 1998, by UMI Company. All rights reserved.

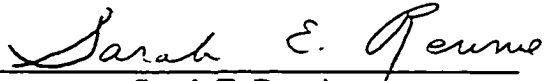
**This microform edition is protected against unauthorized
copying under Title 17, United States Code.**

UMI
300 North Zeeb Road
Ann Arbor, MI 48103

APPROVAL SHEET

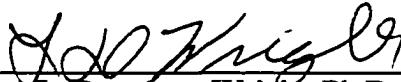
This dissertation is submitted in partial fulfillment of
the requirements for the degree of

Doctor of Philosophy



Sarah E. Rennie

Approved, 31 March, 1998



L. Donelson Wright, Ph.D.
Committee Co-Chairman / Advisor



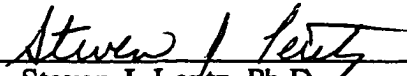
John M. Brubaker, Ph.D.
Committee Co-Chairman / Advisor



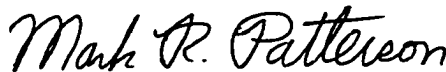
Carl T. Friedrichs, Ph.D.



John L. Largier, Ph.D.
University of Capetown, South Africa and
Scripps Institute of Oceanography, LaJolla, California



Steven J. Lertz, Ph.D.
Woods Hole Oceanographic Institution
Woods Hole, Massachusetts



Mark R. Patterson, Ph.D.

TABLE OF CONTENTS

ACKNOWLEDGMENTS.....	v
LIST OF TABLES	vi
LIST OF FIGURES	vii
LIST OF SYMBOLS	xi
ABSTRACT	xii
1 INTRODUCTION	2
1.1 Coastal ocean regimes	2
1.2 Regional Middle Atlantic Bight circulation	5
1.3 Buoyant plumes	6
1.3.1 Observations	6
1.3.2 Observations of the Chesapeake outflow	8
1.3.3 Models	10
1.3.4 Classification schemes	13
1.4 Objectives and Outline	15
2 CoOP FIELD PROGRAM and DATA PROCESSING	19
2.1 Site location	19
2.2 Instrumentation	20
2.2.1 Across-shelf moorings	20
2.2.2 Shipboard survey	21
2.2.3 Along-shelf moorings	23
2.2.4 Supplemental data	23
2.3 Data processing	24
2.3.1 Time series from moorings	24
2.3.2 Shipboard data processing	25
3 ALONGCOAST PROPAGATION OF PLUMES	29
3.1 Introduction	30
3.2 Typical Upwelling and Downwelling events	32
3.3 Cross-shore spatial structure	35
3.4 Alongcoast propagation speed and wind effects	40

3.5	Currents	47
36	Summary and Conclusions	51
4	SOURCE OF PLUMES	70
4.1	Introduction	71
4.2	Freshwater inflow	72
4.3	Meteorological Control of Bay/Shelf exchange:	73
4.3.1	Observations	74
4.3.2	Background	81
4.3.3	Spectral analysis	84
4.3.4	Barotropic model of estuary/ocean interaction	89
4.3.5	Model Behavior with varying parameters	92
4.3.6	Contribution of the across-shore wind	94
4.3.7	Summary	95
4.4	Downcoast freshwater flux	99
5	DISPERSAL OF PLUMES	122
5.1	Offshore movement: background	123
5.2	Timing and patterns of offshore movement	125
5.2.1	Moored salinity time series	125
5.2.2	Shipboard salinity observations	129
5.2.3	Overall statistics	131
5.3.	Theory for wind-driven offshore movement	131
5.3.1	Response to along-shore winds: Shortest time scales:	132
5.3.2	Response to along-shore winds: Intermediate time scales:	134
5.3.3	Response to along-shore winds: Frictional equilibrium	138
5.3.4	Role of cross-shore winds:	140
5.4	Geostrophic Adjustment	142
5.5	Tides	145
5.6	Summary	147
6	SYNOPSIS	165
61	Alongshore propagation	165
62	Source variability	167
63	Offshore movement of plumes	169
	LITERATURE CITED	171

ACKNOWLEDGMENTS

I wish to thank all of my committee for their support throughout this work, especially my co-advisors, Dr. Don Wright and Dr. John Brubaker. Much is owed to the insights of Dr. John Largier, whose interest and curiosity were always inspiring. He and Dr. Steven Lentz generously provided much of the data analyzed here, as well as thoughtful guidance. Whenever I needed patient encouragement, Dr. Carl Friedrich's door was always open.

The success of the field experiment was due to the efforts of many people. I must thank the captain and crew of the R/V Cape Hatteras for their excellent work, along with the shipboard efforts of Walt Waldorf, John Brubaker, Cheryl Greengrove, and Jay Austin. Robert Guza and Steve Elgar graciously provided their nearshore data. Dr. Cheryl Ann Butman's friendly guidance made the CoOP effort all come together. The CoOP field work was supported by the U. S. National Science Foundation under grants OCE-92-21615, OCE 91-23513, and OCE-92-21614.

Acknowledgment is due Dr. William Boicourt, whose thoughts were seminal to the work presented here. The friendship of Dr. Linda Frizzell-Makowski, who showed me that it could be done, has meant a great deal.

Most importantly, I could not have started or completed this undertaking without the love and support of my husband, Ephraim Rubenstein, and patient daughters, Amelia and Madeleine. Words cannot express.

This research was supported by an Augmentation Award for Science and Engineering Research Training (AASERT) from the Office of Naval Research.

LIST OF TABLES

1.1	Summary of Plume Classification Parameters.....	13
4.1	Area assigned to each waterlevel gauge in Bay.....	74
4.2	Times of volume flux peaks and intrusion arrivals.....	77
4.3	Freshwater flux estimates for each plume event.....	100
5.1	Speed of offshore movement of plumes.....	127
5.2	Amplitudes and phases of tidal currents.....	146

LIST OF FIGURES

1.1	Site map of field location.	17
1.2.	Conceptual diagram of rotationally dominated plume.	18
2.1.	Cross-shelf mooring array with instrumentation.	27
2.2.	Instrument Location Map.	28
3.1.	Complete hourly salinity time series.	54
3.2.	Three week time series of along-shore wind and salinity.	55
3.3.	Surface and bottom salinity and along-shore current.	56
3.4.	Cross-shore sections of CTD salinity with ADCP velocities.	57
3.5.	Three week time series of surface and bottom currents.	58
3.6.	A) Thickness of plume. B) % time plume water is present.	59
3.7.	A) Thickness of plume; and B) strength of the stratification; and C) width of plume <i>versus</i> along-shore wind stress.	60
3.8.	Histogram of FRF wind direction.	61
3.9.	Position of southward propagating front of low salinity intrusion <i>versus</i> time in days since reaching sensor J0.	62
3.10.	Observed propagation speed (C_{adj}) compared with theoretical linear internal wave phase speed (C_{int})	63
3.11.	Velocity (over-ground) of low salinity intrusion <i>versus</i> recent wind stress (average of previous 10 hours).	64
3.12.	A) Observed propagation speed C_{adj} <i>versus</i> alongshelf distance. B) Minimum observed salinity for each event.	65
3.13.	Relative along-coast propagation speed <i>versus</i> ΔSal	66
3.14.	Timeseries of surface stress, bottom stress and along-shore baroclinic pressure gradient.	67
3.15.	Map of ADCP surface velocities and 30 psu isohaline.	68

3.16.	Surface salinity, and along-shore component of ADCP velocity (greyscale contours) overlaid with salinity contours.	69
4.1.	Streamflow into the Chesapeake Bay.	103
4.2.	Location of water level stations in the Chesapeake Bay.	104
4.3.	Low pass filtered time series: a) Subtidal volume flux and time rate of change of the north-south winds. b) Salinity c) Total volume. d) Winds from Chesapeake Light Tower.	105
4.4.	Power spectra of volume flux, coastal wind stress components and tributary inflow.	106
4.5.	Alongcoast position of southward-propagating intrusion <i>versus</i> time in days measured from the passage by sensor J1. ...	107
4.6.	Correlation between along-shore wind stress and a) along-shore current or b) salinity <i>versus</i> lag in hours.	108
4.7.	Diagram of remote vs local effect of meteorological forcing on the Chesapeake Bay.	109
4.8.	Coherence and phase relationships for crossspectra between coastal wind stress components and volume flux.	110
4.9.	Time series of measured and estimated current through the Bay mouth (1982).....	111
4.10.	a) Spectra of volume flux and measured current and salinity from Stn40 for July to October, 1982. b) Coherence and phase between volume flux and currents. c) Coherence and phase between current and salinity.....	112
4.11.	a) Spectra of volume flux and wind stress components from July to October, 1982. b) Coherence and phase between north-south wind and volume flux. c) Coherence and phase between east-west wind and volume flux.	113
4.12.	Power Spectra of waterlevels from head and mouth of Bay.	114
4.13.	Coherence and phase of cross spectrum between volume flux and the salinity at location J1.	115
4.14.	Diagram of analytical model setup. (after Garvine (1985),Fig 1.) ..	116

4.15.	Amplitudes of surface elevations due to along-shore wind in two different length basins. Lower panels: Current.	117
4.16.	a) Amplitude of surface elevation at head of Bay. b) Phase between wind forcing and surface elevation. c) Amplitude of total current at mouth,with ratio of local to remote contributions. d) same as c for linearly decreasing α	118
4.17.	Transfer function between along-shore wind stress and a) waterlevel from mouth and b) waterlevel from head.	119
4.18.	Amplitude of total current at mouth with wind stress varied over direction. a) fixed $\alpha = 1.8e-4$; b) case for decreasing α	120
4.19.	Freshwater flux estimates.	121
5.1.	Lower panel : near-surface salinities. Upper panel : wind components with waterlevel overlaid.	149
5.2.	Salinity and cross-shore velocity profiles, anchor station 4.	150
5.3.	Surface salinity traces from shipboard underway mapping system. Lower panel: Ship track.	151
5.4.	Salinity transects from LN5 and SSB2, Oct 18 and 19, 1994	152
5.5.	Surface salinity from shipboard underway mapping system taken on successive cross-shelf transects (October, 1994).	153
5.6.	Offshore movement of salinity front.	154
5.7.	Offshore position of high-gradient region of salinity <i>versus</i> a) along-shore wind stress and b) cross-shore wind stress.	155
5.8.	Time-evolving solution to along-shore wind.	156
5.9.	Salinity and ADCP velocities from transect across central line, during mild upwelling winds.	157
5.10.	a) Inertial oscillations in stratification-limited flow. b) steady stratification-limited flow. c) flow in bottom Ekman layer	158
5.11.	Two-layer coastal jet solution: a) cross-shore flows b) along-shore flows.	159

5.12.	Summary of theoretical offshore velocities.	160
5.13.	Amplitude of complex demodulation of inertial frequency	161
5.14.	Sheared cross-shelf wind-driven flow compared with pressure-gradient flow.	162
5.15.	Observed shear <i>versus</i> predicted shear due to cross-shore density gradient (thermal wind relationship).	163
5.16.	Shape of the density front after geostrophic adjustment.	164

LIST OF SYMBOLS

A_v	kinematic eddy viscosity in vertical direction
C	barotropic linear wave speed
C_{abj}	observed wave speed adjusted for ambient shelf flow
C_{int}	internal linear wave speed
C_d	bottom drag coefficient
C_{obs}	observed wave speed
D_{ek}	Ekman depth
f	Coriolis parameter
g	acceleration due to gravity
h_{plume}	thickness of plume (top layer in two-layer system)
H_{total}	total depth of water column
η	surface elevation
K	Kelvin number
N	Brunt-Vaisala frequency
ρ	density of sea water
R_{ext}	external (barotropic) Rossby radius of deformation, $R_{ext} = \frac{\sqrt{g h}}{f}$
R_{int}	internal (baroclinic) Rossby radius, $R_{int} = \frac{\sqrt{\frac{\rho_{top} - \rho_{bot}}{\rho_{bot}} g h}}{f}$
S_{Bu}	Burger number
τ_x	cross-shore shear stress (+ applied in offshore direction)
τ_y	alongshore shear stress (+ applied in alongshore direction)
u	horizontal velocity (+ in offshore direction)
u^*	friction or shear velocity ($u^* = \sqrt{\frac{\tau}{\rho}}$)
U_{ek}	Ekman transport
v	horizontal velocity in alongshore direction
w	complex horizontal velocity
x	rectangular position coordinate in offshore direction
y	rectangular position coordinate in alongshore direction
z	vertical coordinate

ABSTRACT

The characteristics and effects of intrusions of estuarine outflow over the inner shelf were examined, based on hydrographic and meteorological observations obtained during the "Coastal Ocean Processes" (CoOP'94) field experiment located off the Outer Banks at Duck, North Carolina. The episodic presence of distinct low salinity water masses issuing from the Chesapeake Bay created an intermittent baroclinic coastal current along the North Carolina coast. Under low wind conditions, this current occupied the upper half of the water column within 9 km of the coast. The plume was bounded by a distinct southward-propagating front, a region offshore of high horizontal salinity and velocity gradients, and a strong pycnocline underneath. The intrusion traveled along the coast at a speed comparable to the linear internal wave speed of a two-layer system. Intrusions were generally associated with southward winds (downwelling conditions); however, several observed events opposed northward wind-driven flow.

The geometry and dynamics of the low salinity plume were strongly controlled by the local winds. Northward (upwelling) winds caused the plumes to widen offshore and thin vertically. Southward (downwelling) winds acted initially to speed the intrusions' alongcoast movement and cause them to narrow and deepen. Under strong downwelling winds, however, the intrusions contacted the bottom. This greatly decreased their speeds and caused diffusive widening. Propagation speeds of all plumes were seen to slow steadily through the study region. This was attributed to the observed mixing with ambient water along the path of the intrusion which increased its salinity, thereby reducing the buoyancy forcing.

Under the continued influence of upwelling winds, the low salinity intrusions moved rapidly away from the coast and formed shallow lenses floating over the ambient shelf water. These generally dissipated in 1 to 2 days. The theoretical offshore transport response to wind forcing was investigated, illustrating two dynamical behaviors of the plumes, depending on whether they occupied the entire water column or were vertically segregated by stratification.

The meteorological control of Bay/shelf exchange was examined to better comprehend the pulsed timing of the low salinity intrusions, which occurred every 2 to 8 days. Estimates of volume flux were derived from temporal variations of waterlevel measurements within the Chesapeake Bay. The volume flux time series exhibited strong peaks of outflow, which preceded the low salinity events off Duck, N.C. by an average of 1.1 days, a time lag consistent with the observed alongcoast propagation speeds.

**Wind Interaction with Buoyant Plumes
on the Inner Continental Shelf**

Chapter 1. Introduction

The coastal ocean contains the majority of our important maritime resources and we, the human population, have a great impact on that region in turn. The high biological productivity of the coastal ocean is enhanced by nutrients derived from terrestrial sources. However, increasingly the coastal ocean ecosystem may also be stressed by anthropogenic inputs of pollutants. One major mode of delivery of these inputs to the ocean is the outflow from estuaries. Along the east coast of the United States, a 170,000 km² watershed drains portions of six states into the Chesapeake Bay. The Bay outflow is the largest point source of freshwater south of the Gulf of Maine, contributing over half of the runoff delivered directly to the Middle Atlantic Bight (Boicourt, 1973). This thesis will examine the source variability, along-coast evolution, and eventual dispersal of this low salinity outflow over the inner shelf.

1.1 Coastal Ocean Regimes

The Middle Atlantic Bight (Figure 1.1), being adjacent to a heavily populated, urbanized area, has been among the most studied of coastal regions, especially in the last twenty-five years. Concerns over declining fisheries, ocean waste dumping and shoreline erosion, as well as the needs of commercial shipping and recreational interests, have motivated

research efforts that have greatly increased our understanding of the complex processes controlling the circulation on the continental shelf.

Most of these efforts have focused on the middle and outer shelf where frictional effects are confined to surface and bottom boundary layers, with the much of the water column constituting an interior region where inviscid dynamics prevail (Allen et al.,1980). The dominant dynamics of these deeper regions have fairly large horizontal scales: a homogeneous ocean subjected to wind forcing adjusts to the presence of the coastline over the length scale given by R_{ext} , the external Rossby radius of deformation. In the Middle Atlantic Bight, the external Rossby radius is on the order of 100 km and thus encompasses the entire shelf width.

At the other extreme is the nearshore or surfzone where the physics are dominated by the effects of breaking surface gravity waves. The generation of longshore currents by gradients in radiation stress, and the cross-shore 'undertow' circulation resulting from wave-driven mass transport are important in regions where shoaling water depths cause wave steepening and dissipation. The width of this region varies with the sea state, but is usually confined to the shoremost several hundred meters.

Between these regimes lies the inner shelf, where, in the Middle Atlantic Bight, depths are less than 30 m. This region, usually within 10 km of the coastline, has also been termed the 'shoreface' by geologists or the 'coastal boundary layer' by physical oceanographers. Dynamically, the inner shelf is an area where overlapping Ekman boundary layers interact (Lentz, 1995). The increasing interaction of the surface and bottom frictional layers with decreasing depth results in the progressive blocking of the Ekman transport (Mitchum and Clarke, 1986), with increasingly

more of the surface stress transmitted directly to the bottom. The resulting cross-shore gradients in bed stress are identified by coastal geologists as an important determinant in sediment transport patterns. The area of maximum divergence in the cross-shore Ekman transport defines the location of the strongest upwelling, which is of primary importance to the biology of the region.

The degree of interaction between the surface and bottom Ekman layers depends critically on the vertical stratification within the water column, since that controls the thickness of each layer. Variation in stratification over the inner shelf is particularly sensitive to atmospheric inputs of wind and heat, as all the energy is absorbed into very shallow depths. Tidal and surface gravity wave motions can also modify the stratification of the inner shelf.

It is into this complex inner shelf region that the outflow from the Chesapeake Bay intrudes. This brackish plume generally has an initial salinity between 16 to 26 psu, compared with the ambient shelf salinity of 32 to 34 psu, resulting in a density deficit of 6 to 12 kg/m³. The density contrast provides a buoyancy forcing, and the plume's large scale makes the buoyancy-forced motion subject to the earth's rotation. These factors combine to produce a buoyancy current that turns to become rotationally trapped against the coast, flowing southward as far as Cape Hatteras, North Carolina (Boicourt, 1973). The fundamental length scale resulting from the balance between the density stratification and the Coriolis force is the internal, or baroclinic, Rossby radius, R_{int} , resulting in a width scale for the buoyant current of approximately 5 km. The nutrients, pollutants, estuarine biota or sediment carried by the plume will be delivered largely to this inner shelf region. And, perhaps most importantly, the stability of

the water column will be strongly affected by the export of positive buoyancy from the estuary, altering the inner shelf's response to other forcings.

1.2 Regional Middle Atlantic Bight Circulation.

Observations by Boicourt and Hacker (1976), and Noble and Butman (1979), along with modeling efforts such as those of Stommel and Leetma (1972), established a picture of the large scale circulation over the eastern U.S. continental shelf. Most of the subtidal current fluctuations in the Middle Atlantic Bight are driven directly by the regional wind stress field, especially in the meteorological synoptic (3 to 10 day) time scale. Another contribution comes in the form of energy that appears to be freely propagating along the shelf. The response, which is dominantly barotropic, and so influences the full shelf width, is spatially coherent over very large distances in the alongshelf direction. These observations are unified in continental shelf wave theory where the sloping bottom topography along the continental margin acts as a wave guide. This theory is most applicable in the long wave form (Gill and Schumann, 1974) which results in the across-shelf momentum balance being geostrophic, as has been repeatedly observed for the mid shelf (Pettigrew, 1981). Free waves propagate with the coastline on the right (southward in the Middle Atlantic Bight) and have been shown to contribute up to 30% of the energy at times in the southern Middle Atlantic Bight (Noble et al., 1983). However, the dominant response in the Middle Atlantic Bight is a

frictional steady-state, where the damped ("arrested") forced wave remains in phase with the wind forcing (Csanady, 1978a).

In contrast to the wind-driven synoptic response, there exists a mean southwestward flow for time scales of longer than a month of 5 to 9 cm/s that opposes the mean wind stress, which is north or northeastward during the summer, and largely offshore during the winter (Beardsley and Boicourt, 1981). Work by Csanady (1978a), Beardsley and Winant (1979), and Semtner and Mintz (1977), among others, suggest that this mean flow is driven by an along-shore pressure gradient imposed on the shelf by large scale oceanic patterns, rather than by pressure gradients produced by fresh water outflow along the east coast. The Chesapeake plume's natural direction of travel is equatorward (with the coastline on the right) due to Coriolis deflection, and this ambient shelf flow will enhance that southward tendency.

1.3 Buoyant Plumes

In order to provide a framework in which to characterize the Chesapeake Bay outflow, the major observational and modeling efforts that have shaped our understanding of buoyant plumes are briefly summarized here.

1.3.1 Buoyant Plumes: Observations

Among the largest freshwater discharge systems that have been studied extensively are the Mississippi (Wright and Coleman, 1971), and the

Amazon (Geyer et al., 1991, Lentz and Limeburner, 1995). The Mississippi empties into the Gulf of Mexico, where tide and wave energy are minimal and do not disturb the buoyant outflow which spreads as a distinct surface layer over a strong pycnocline, with lateral circulation patterns developing. The Amazon also forms a fresh layer which encounters significant semi-diurnal tidal mixing and entrains large volumes of oceanic water as it is swept to the northwest by the trade winds and the North Brazil Current. Examples of much smaller discharges which also remain highly stratified are the Connecticut River (Garvine, 1974) and Koombana Bay in Western Australia (Luketina and Imberger, 1987). These small buoyant plumes are observed to spread radially, with converging flow at the leading edge producing a deeper "roller" region.

The freshwater discharge into the South Atlantic Bight occurs not as a single point source, but from a series of small inlets. The resulting coastal current is vertically well mixed by tidal currents (Blanton and Atkinson, 1983). The frontal region outside of this low salinity zone is strongly influenced by the local winds: northward along-shore wind stress causes the front to slope seaward, whereas southward stress confines the front to a narrow zone close to the coast, with strong horizontal salinity gradients. Munchow and Garvine (1993a) describe the discharge from the Delaware river forming a buoyant coastal current that occupies the full water depth of the inner shelf. The outflow from the Rhine, which turns to flow northeastward for over 100 km along the Dutch coast (de Ruiter et al., 1992), occupies the entire water column during strong spring tides, but remains in a stratified surface layer during neap tides (Simpson et al., 1993).

Although large variations in buoyant outflow are expected on seasonal time scales, reflecting annual cycles of freshwater input; and also at high frequencies due to the control of diurnal or semi-diurnal tides, most of these observational studies also exhibit significant temporal variability from the fortnightly spring-neap tidal time scale down to wind-driven variations occurring over the period of a day or two.

1.3.2 Buoyant plumes: Observations of the Chesapeake Bay Outflow

The Chesapeake Bay is a large estuary that acts as a reservoir within which the tributary inflow mixes significantly with saltier shelf water before discharging. This creates a brackish outflow to the shelf with a density deficit that is significant but smaller than the nearly fresh discharge of the Mississippi or Amazon. The classical picture of gravitational circulation in a partially-mixed estuary such as the Chesapeake Bay was established by Pritchard (1956), who described a two-layer pattern with the low salinity upper layer flowing seaward, underlain by a higher salinity return flow. Boicourt (1973) observed that the exchange between the Chesapeake Bay and the shelf waters does not always exhibit a steady two-layer structure, but can be dominated by wind-driven outflow surges. The outflow occurs largely through the southern portion of the Bay mouth, with the high-salinity inflow concentrated in the deep part of the main channel, or over the northern shoals. Boicourt mapped the Chesapeake Bay plume making a wide anticyclonic turn in a bulge region offshore and south of the mouth. South of the turning region, the low salinity outflow appeared as trapped against the righthand coast as a high-velocity jet. This is illustrated conceptually in Figure 1.2.

Other observational studies of the Chesapeake Bay plume, including SuperFlux (Campbell and Thomas, 1981) and MECCAS (Boicourt et al., 1987), focused largely on the near-field turning region, and included biological measurements to determine the export of nutrients and primary production from the Bay. These studies sought to clarify the complicated relationship between the near-field plume behavior and freshwater source strength, wind stress and coastal circulation conditions. Use of remote sensing, along with higher resolution salinity measurements, allowed SuperFlux researchers to map the strong front defining the outer edge of the plume. A sharp halocline was measured underlying the outflow, usually at a depth of 5 to 8 m. The MECCAS observations showed plumes in the turning region/coastal jet configuration, but also observed outflow that was spread east offshore of the mouth by the Ekman effect of northward winds, with higher salinity water upwelled between the plume and the coast. Continued observations showed that a plume was reestablished against the coast rapidly after the northward winds ceased.

A more recent field program (Berger et al., 1995) sited farther south, off the coast of North Carolina, included observations of the Chesapeake outflow which were analyzed for its contribution to the hydrography of the Middle Atlantic bight. They found evidence of buoyancy-driven flows over the inner shelf as far south as Cape Hatteras. Observations over two years revealed strong interannual differences, with buoyancy flows much more prevalent in the year of higher river runoff (1993). Drifters deployed over the inner shelf (within several kilometers from shore) showed enhanced southward velocities as well as convergence towards the offshore salinity front.

1.3.3 Buoyant Plumes: Models

Until very recently, the Chesapeake Bay plume has inspired more modeling efforts than observational studies. Beardsley and Hart(1978) developed an analytical model to describe a steady estuarine outflow. They assumed linear dynamics in a one- and two-layer framework driven by a point mass source and sink. The solution showed two-layer oppositely-directed flows along the shelf. Anticyclonic turning at the mouth was generated only in the one-layer case and attributed to effects of the offshore sloping bottom. Concluding that the non-linear terms were important in the turning behavior of the exiting plume, Chao and Boicourt (1986) developed a three-dimensional primitive equation model set up with scales appropriate to the Chesapeake region that produced turning with right-bounded propagation for both flat and sloping shelf bottoms. Two-layer flows were confined to the bulge region immediately outside of the mouth, while currents in the along-coast density intrusion were unidirectional. The sloping shelf reduced the seaward extension of the bulge due to the additional potential vorticity constraint, and limited the extent of the return undercurrent due to the additional barotropic component (Chao, 1988a).

These non-linear numerical models, along with aspects of laboratory work from Stern et al. (1982) and Griffiths and Hopfinger (1983) better match the Chesapeake observations, where there are distinct near-field (turning bulge with undercurrent) and far-field (unidirectional coastal jet) solutions, with a sharp transition between them (Figure 1.2). Yankovsky and Chapman (1997) proposed that the dynamics of the

turning region are described by a cyclostrophic balance. When the low salinity water occupies only the surface layers, the laboratory experiments, as well as Chao's numerical model, show that the plume advances along the righthand coast as a bore intrusion with the rear advancing faster than the nose. Convergence in the intruding upper layer flow forces downwelling, producing a nose that is deeper than the neck behind it. Lateral detrainment is observed along the seaward side of the nose. The width of the coastal jet is comparable to the baroclinic Rossby radius, with the current set up behind the passage of the head adjusting to a quasi-geostrophic balance (Kao, 1978).

To focus on the importance of the plume fronts, Garvine (1982) and O'Donnell (1988) moved away from general circulation models and developed two-layer reduced gravity models that allow the inclusion of fronts as discontinuities with appropriate jump conditions, including interfacial friction and mass entrainment. These models look at the dynamics of a buoyant surface layer that is shallow compared to the total water depth. For outflows where rotation is important, Garvine (1987) reveals two fronts with different functions: the discharge front at the turning region and a coastal front that changes from an interior to boundary front as it migrates downstream. It then evolves into what Garvine terms a depth-discontinuity type of front (where isopycnals are near-vertical). The extent to which the plume mixes with the inner shelf waters depends on the timing and mechanisms of frontal dissipation.

The extreme sensitivity of numerical buoyant plume model behavior to the parameterization of vertical mixing was examined by Ruddick et al. (1997). An increase in the vertical mixing coefficient in Chao's models removed the vertical stratification and produced a plume

with smaller seaward excursion of the bulge, and a wider, slower, coastal flow. Chapman and Lentz (1994) explored the behavior of surface-to-bottom plumes as they are influenced by bottom topography. The offshore transport in the bottom boundary layer advects freshwater offshore. The plume then widens until the front reaches the isobath where the vertical shear through the water column is just enough to cause a change in sign of the across-shelf flow at the bottom. Yankovsky and Chapman (1997) devised a theory whereby, given information on the buoyant outflow velocity and density anomaly, along with knowledge of the bottom slope, one can determine whether the outflow will form a surface-to-bottom, or a surface-trapped plume.

Further numerical experiments with the addition of wind forcing allowed Chao (1987, 1988b) to examine the wind-driven motion of the plume front. The response was dominated by the surface Ekman drift with strongly asymmetric results: downwelling winds narrow the buoyant current against the coast, deepening and accelerating it, while upwelling transport moves the surface-trapped plume offshore, thinning it and opposing its southward momentum. However, Chao's model indicates that it is unlikely that upwelling winds could turn the current against its natural direction of propagation. Indeed, very few field surveys have observed plume deflection to the north of the Bay mouth.

More recent model experiments by Kourafalou et al. (1996) continue exploring the variation of plume behavior under differing buoyancy source strengths, turbulent mixing regimes, bottom slopes, and wind stress. These results show that while moderate to strong upwelling winds could induce down-wind currents within the low salinity waters, the major transport was strongly offshore under these conditions.

1.3.4 Classification Schemes

In order to merge the information gained from these observational and modeling efforts into a more cohesive framework, researchers have proposed several classification schemes for buoyant plumes. By identifying the pertinent factors that strongly influence the development of a plume, a variety of responses can be organized into a more insightful structure. These scalings are summarized in Table 1.1 and described below.

Parameter#	Compares	Formed from	Small values indicate domination by
Rosby# R_o	inertial/rotation	$C_{obs}/(f*L_{obs})$	by rotation
Froude# F (internal)	inertial/ stratification	C_{obs}/C_{int}	by stratification
Froude# (empirical)	inertial/ gravity	$U_{discharge}/C_{obs}$	by gravity
Burger# S_{bu} $= (R_o/F)^2$	stratification / rotation	$(R_{int}/L_{obs})^2$	by rotation
Kelvin # $= (1/S_{bu})^2$	rotation/ stratification	L_{obs}/R_{int}	by stratification
Ekman#	friction/rotation	$\sqrt{2A_v}/f / H_{total}$	by rotation over friction

Table 1.1
Summary of Plume Classification Parameters.

The parameter that most effectively distributes plume behavior into a dynamical hierarchy has been identified as the Kelvin number, $K = \frac{L_{obs}}{R_{int}}$, the ratio of the width of the plume (usually impressed upon the outflow by the dimension of the mouth of the river or estuary) to the internal Rossby radius (Krauss, 1973). The ratio reveals the dynamical importance of the Coriolis force on the plume structure (Garvine ,1995). For plumes

with small values of K , the path of the outflow will be controlled more by the ambient shelf flow, or by the influence of along-shore wind stress. The ratio K can be small due to a small outflow size (e.g. the Connecticut River); or a large outflow constrained by a small topographic opening (e.g. the Mississippi, where the mouth of the river is not more than 100 m across). The value of K will also become small in low latitudes where the vanishing Coriolis force produces a very large Rossby radius (e.g. the Amazon). Large K plumes are dominated by rotation and will always travel along-shore in the down-coast direction (in the direction of Kelvin wave propagation). Examples of these flows include the Norwegian (Rey, 1981) and the Scottish coastal currents (Hill and Simpson, 1988).

An alternative version of the Kelvin number is the Burger number, $S_{Bu} = \left[\frac{R_{int}}{L_{obs}} \right]^2 = \frac{1}{K^2}$. The Burger number can be formed from a combination of the Rossby number and the internal Froude number, two non-dimensional parameters which are commonly used to measure the relative contribution of non-linear advection to rotation and to stratification, respectively (Cushman-Roisin, 1994). The Burger number expresses the influence of stratification relative to rotation. Garvine (1995) analyzed observations from a dozen plume studies and noted that those with K or S_{Bu} of $O(1)$, for which both stratification and rotation are important, have the most dynamically complex behavior.

Chao (1988b) characterized a set of modeling results for plumes with $K = O(1)$ according to two additional dimensionless parameters. The values of these parameters determines the plume's shape and offshore extent. The first is an empirical Froude number, defined as the ratio of the speed of the buoyant discharge, $U_{DISCHARGE}$, at the estuary's mouth to the observed intrusion speed, C_{obs} , just down-coast of the turning region.

Chao determined that modeled plumes for which this ratio is > 1 (termed "supercritical") are characterized by turning regions that bulge far out from the mouth. The seaward extent of the bulge is much reduced for subcritical plumes with empirical Froude numbers less than unity. A second parameter, the ratio of C_{obs} to C_{int} (the linear internal gravity wave speed), describes the behavior of the coastal jet portion. For $C_{obs}/C_{int} \ll 1$, which Chao termed "diffusive", the coastal jet widens beyond R_{int} , indicating increasing dissipation.

In an analysis of the Delaware coastal current, Munchow and Garvine (1993) proposed the use of three parameters to classify plume behavior: the Burger number and a Rossby number (or alternatively, an internal Froude number) to summarize the respective importance of stratification, rotation and non-linear inertial forces; plus the vertical Ekman number, $E = \left(\frac{\delta}{h}\right)^2$, where $\delta = \sqrt{\frac{2A_z}{f}}$ is the Ekman layer thickness, to describe the frictional forces. The first two parameters determine the plume's formation and evolution patterns in the source region, while the Ekman number performs the role of Chao's diffusive parameter in determining the development of the coastal jet.

1.4 Objectives and Outline of Dissertation

Using field observations taken during the summer and fall of 1994, this thesis examines the far field characteristics and behavior of the Chesapeake plume as it makes its way down the North Carolina coast. The spatial and temporal characteristics of the low salinity intrusion are determined, along with the associated coastal buoyancy currents, focusing

on patterns of variability occurring within a 1 day to 1 week time scale. Over this time scale wind forcing is seen to exert a major influence on the plume. How these observations fit into the classification schemes described above is considered, and an extension of the classification scheme to account for wind effects is discussed.

In the next chapter, the field program is described, as are the methods of processing the recorded data. The objective of chapter 3 is to determine the along-coast propagation behavior of the plume. The general spatial characteristics of the plume are delineated, and the influence of the wind on its shape is investigated. Wind effects on the propagation speed are also estimated. Evidence for mixing between the plume and the ambient shelf water is quantified, as well as the effect that this dilution has on the along-coast propagation speed.

Chapter 4 will identify the controlling processes that determine the timing of the intermittent presence of low salinity intrusions observed. The meteorological control of the patterns of outflow of estuarine water from the Chesapeake Bay will be examined using both the 1994 data set and an additional one from 1982. In addition, an analytical modeling exercise allows the examination of two separate, opposing forcing mechanisms, whose effects are combined in the observations. Chapter 5 focusses on the processes that cause the dispersal of the plume offshore during upwelling conditions, as this appears to be the main mode for the delivery of estuarine water to the mid-shelf.

Figure 1.1 Site map of field location: Duck, North Carolina in the Middle Atlantic Bight

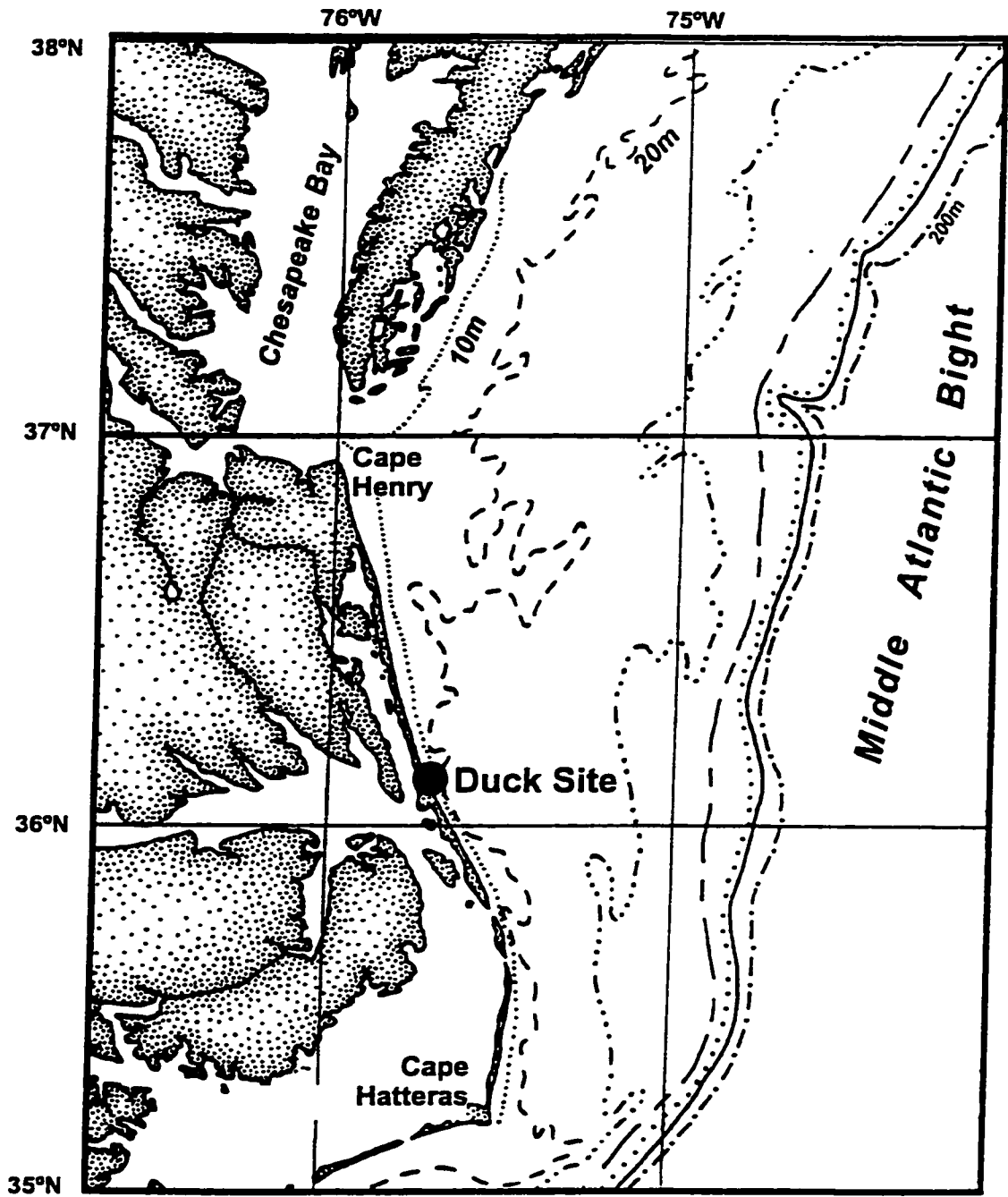


Figure 1.1 Study site.

Figure 1.2 Conceptual diagram of rotationally dominated plume shown in map view.

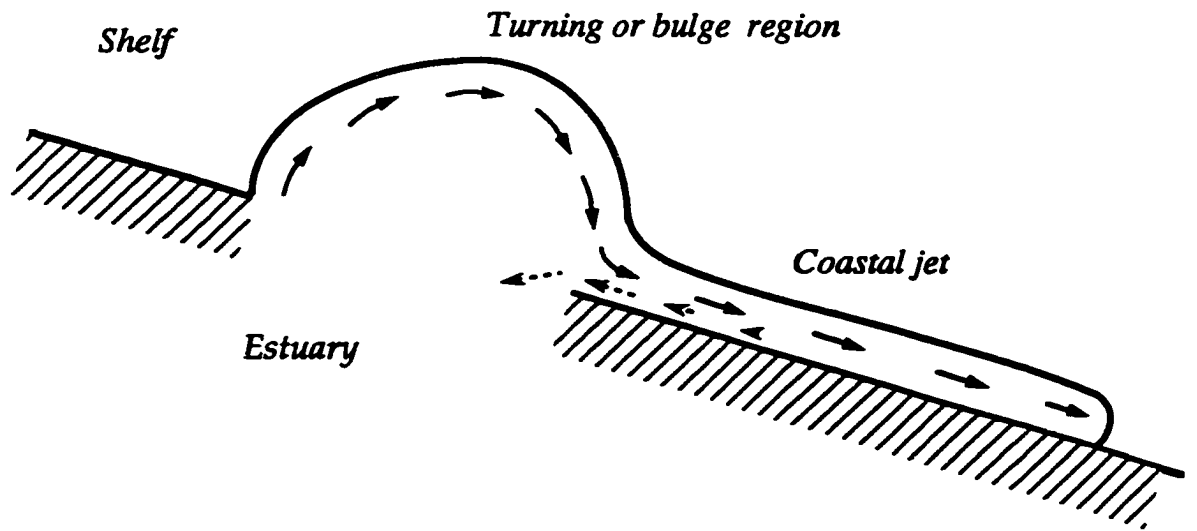


Figure 1.2. Conceptual diagram of a rotationally dominated buoyant plume (dashed arrows indicate bottom layer return flow).

Chapter 2 CoOP Field Program and Data processing

As part of the interdisciplinary National Science Foundation "Coastal Ocean Processes" (CoOP) program, a study entitled "Suspension, across-shelf Transport and Deposition of Planktonic Larvae of Inner Shelf Invertebrates" was undertaken. The field work consisted of two month-long intensive field expeditions in August and October of 1994, centered on the inner shelf off of the Outer Banks at Duck, North Carolina (Figure 1.1). This site is located approximately 85 km downstream from the mouth of the Chesapeake Bay. The focus of this project was to understand the dispersal and then resettlement patterns of the larvae of nearshore/shoreface-dwelling benthic invertebrates (Butman, 1994). During their planktonic stage, which lasts on the order of a month, the larvae are presumed to act as passive particles carried by horizontal currents. However, their swimming speeds could allow them to control their vertical position in the water column, and thereby exploit the vertical segregation of the across-shelf flows over the inner shelf in order to control their horizontal position. The observational program was designed to examine the inner shelf circulation on time scales of days to weeks, and to resolve vertical and cross-shore structures.

2.1 Site Location

This site was chosen because of its simple topography; the isobaths parallel the relatively straight shoreline out to a depth of 20 m.

With minimal along-shore topographic variations, the study could focus on the across-shelf flow structure. The intermittent passage of the Chesapeake Bay plume water through the study region proved to be the most significant contribution to the along-shore structure, necessitating at times a three-dimensional view.

The CoOP study was centered offshore of the US. Army Corps of Engineers CERC Field Research Facility (FRF) at Duck, North Carolina. This facility provided the CoOP researchers with supplementary wind, tide, and wave measurements, in addition to logistical support. Previous research at the FRF has documented the general setting of this inner shelf region. The tides are predominately semi-diurnal with a spring range on the order of a meter. The bottom deepens to ~14 m at 2 km away from the coast (slope of 0.007), then slopes away more gently to reach a depth of 20 m at ~ 5 km offshore. The shoreface bottom sediments are sandy, overlying relict lagunal peats which emerge near 20 m depth. Offshore of 20 m there is a series of relict ridges of sand and gravel.

2.2 Instrumentation

2.2.1 Across-Shelf Moorings

Because the focus of the CoOP program was the structure of the cross-shore flows, the core instrumentation of the field study was an across-shelf array of moorings that collected time-series of physical, biological and meteorological data (Figure 2.1). This array crossed the inner shelf from the surf zone out to 25-m depth. In the nearshore region of the central line, current meters on towers were sited at 4-m and 8-m

depths by the ONR Duck94 field program. Surface/subsurface mooring pairs were deployed by Wood Hole Oceanographic Institute which supported VMCM current meters and SeaBird SeaCATs at 4 to 6 vertical levels. These were located in water depths of 13-m (1.5 km offshore), 20-m (5.3 km offshore) and 25-m (17 km offshore). In addition, a meteorological buoy was deployed at the 20-m mooring with Vector Averaging Wind Recorder at a height of 3 m above the surface. Full suites of meteorological measurements including air temperature, radiation, relative humidity and barometric pressure were recorded. These instruments were also maintained over the intervening month of September, although a storm on 4 September caused the loss of the upper current meters at the 20-m mooring. They were redeployed at the beginning of October. On October 12th, the upper portion of the 13-m mooring was also lost to rough weather. A full report of these measurements is provided by Alessi et al. (1996).

2.2.2 Shipboard Survey

Shipbased surveying was done aboard the R/V Cape Hatteras to define the conditions in a region 50 km to the north (just south of Cape Henry) and 50 km to the south (just south of Oregon Inlet) of the central mooring line (Figure 2.2). The ship survey extended as far as 50 km offshore, with most stations concentrated within 20 km of the coast. The sampling was organized into cross-shore transects with stations positioned 2 to 5 km apart. In addition, several times the ship was anchored at one location for a 24-hour period to observe temporal changes, with profiles

taken at half-hour intervals. Over 800 stations were occupied in August and close to 700 in October.

The shipboard observations included Conductivity-Temperature-Depth (CTD) casts with simultaneous Acoustic Doppler Current Profiler (ADCP) sampling and pumping for nkton. The CTD data were collected with a SeaBird 911Plus instrument with dual temperature and conductivity sensors which were calibrated daily against water samples. The ADCP data were collected by a RDI 1.2MHz narrowband instrument supported by a catamaran that held the transducer at 0.4 m below the sea surface. Velocity profiles with 1m vertical resolution were recorded at 1 to 2 Hz while the ship held a stationary position for the CTD cast. At each station the ADCP sampled for at least 4 minutes, usually continuing for 8 to 12 minutes. The catamaran was held just aft of the beam of the ship by a 6 m rigid arm, which increased the instrument's susceptibility to ship roll. Therefore for 14% of the stations, rough weather prevented the use of the ADCP. These CTD and ADCP data are reported in Waldorf et al. (1995, 1996).

In addition to the station data, surface water temperature and salinity were monitored along with position fixes at 15 second intervals while the ship was underway. On occasion, when this surface underway system revealed the presence of sharp salinity fronts typical of the offshore edge of the buoyant plume, the ADCP was towed across the frontal region at speeds of no more than 4 knots.

The R/V Hatteras data was constrained to the region offshore of 1 km from the coast. Supplementing this was near-shore hydrographic data taken from the R/V Moby Duck, a small boat launched from the beach at Duck. CTD transects were taken during 44 days of the three

month study period, including during the month of September, when the Hatteras was not on site. A full report of this data set is presented by Largier and Millikan (1996).

2.2.3 Along-Shelf Moorings

Much of the information regarding the along-coast movement of the plume was derived from an array of five pressure/temperature/conductivity SeaGauge sensors deployed along the 5-m isobath (Figure 2.2). Instruments were located ~1 m above the bottom at sites 17 and 32 km to the north (J0 and J1), and 16 and 25 km to the south (J3 and J4) of the central line. Combined with a SeaCAT mounted on the FRF pier at 4 m above the bottom in 8 m of water, these measurements cover 60 km along-coast for nearly 3 months. At the outer edge of the plume's domain were two surface and bottom SeaCAT/SeaGauge moorings maintained at the 20-m isobath 30 km north (N20) and south (S20) of FRF. Most of these measurements were continuous from early August through the end of October, except for the southern two sensors which were buried during mid-October.

2.2.4 Supplemental Data Sources

In addition to the meteorological measurements made at the 20-m mooring, the FRF maintains an anemometer at a height of 19 m on the end of their pier 500 m offshore. These wind measurements were used when the 20-m mooring ones were not available. The FRF also monitors waterlevels for the NOS tide survey. Additional waterlevel information

was obtained from NOS for several stations within the Chesapeake Bay (see chapter 4). Freshwater flow from the tributaries of the Chesapeake Bay is monitored by USGS.

2.3 Data Processing

Following a protocol agreed upon by all CoOP participants, all velocity measurements, including currents and winds, were rotated 20° counterclockwise with respect to true north to an along- and cross-shore frame of reference. The along-shore axis y is positive towards 340° and the cross-shore axis x is positive towards 70°. Offshore distance at the central transect was referenced from a shore location of -75.7518 longitude and 36.1865 latitude, and was adjusted for coastal curvature to the north and south.

All time information in this document refers to Greenwich Mean Time (GMT). To resolve subtidal patterns, the hourly time series were convolved with the low-pass filter PL64 (Beardsley and Rosenfeld, 1983). This has a half-power point of 38 hours.

2.3.1 Time Series from Moorings

All mooring velocity time series were sampled originally at 4 minute intervals which were then combined into 1 hour averages. To produce density time series, the temperature and salinity measurements were linearly interpolated to the vertical position of the current meters, and combined into density using UNESCO '81 formula (Fofonoff and Millard, 1983).

2.3.2 Shipboard Data Processing

The CTD samples were processed using the SeaBird software which filtered out the ship roll and then averaged the data into 0.25 m bins. Calibration work determined the accuracy in temperature to be 0.003°C and 0.002 psu in salinity. For comparison to the ADCP values (which were determined in overlapping 1 meter bins), a triangular weighting scheme, which mimics the RDI ADCP processing, was applied to produce CTD values at 1 m intervals. This assures that computation of the gradient Richardson number (see chapter 5) has comparable vertical scales for both the numerator and denominator.

The ADCP was always operated in bottom-tracking mode which, on the shallow inner shelf, always gave good returns. The internal pitch and roll corrections were not applied because of possible contamination from wave accelerations. Comparisons between the internal compass and the ship's gyro revealed good agreement. The 1 Hz data were averaged over 15 seconds, a period longer than most of the wind wave and swell energy. These 15 second averages were then passed through a quality control algorithm before being combined into 4 minutes averages. Our data quality analysis revealed that extreme velocity values were not related to high "error" velocities (computed from the redundant vertical velocity of the 4-beam solution), but rather were correlated with a low "percent good" condition (where the acoustic return fell below a set signal-to-noise threshold). Therefore we adopted a post-processing scheme that screens out all data with a "percent good" of less than 85%. For stations

recording more than 4 minutes, an algorithm was developed that searched for the window of 4 consecutive minutes that had the fewest number of rejected samples. If fewer than 2.5 minutes out of 4 had acceptable conditions, the velocity vector at that depth was omitted from further analysis.

When the lower frequency circulation patterns were of primary interest, the tidal signal was removed from the ADCP measurements using a least-squares fit to the tidal constituents as determined from the mooring time series. The M2 semidiurnal and K1 diurnal constituents were found to be the dominant contributors to tidal motion (Shay et al., 1997). The two tidal constituents were allowed to vary linearly in the across-shelf direction only, as the alongshelf tide wavelength was determined to be extremely large (Carr and Lentz, 1996). The amplitude of cross-shore component of the total tidal velocity ranged from 1 cm/s near the coast to 4 cm/s at 20 km offshore. The along-shore component was slightly larger, ranging from 4.5 cm/s nearshore to over 6.6 cm/s offshore.

Figure 2.1. Cross-shelf mooring array with instrumentation.

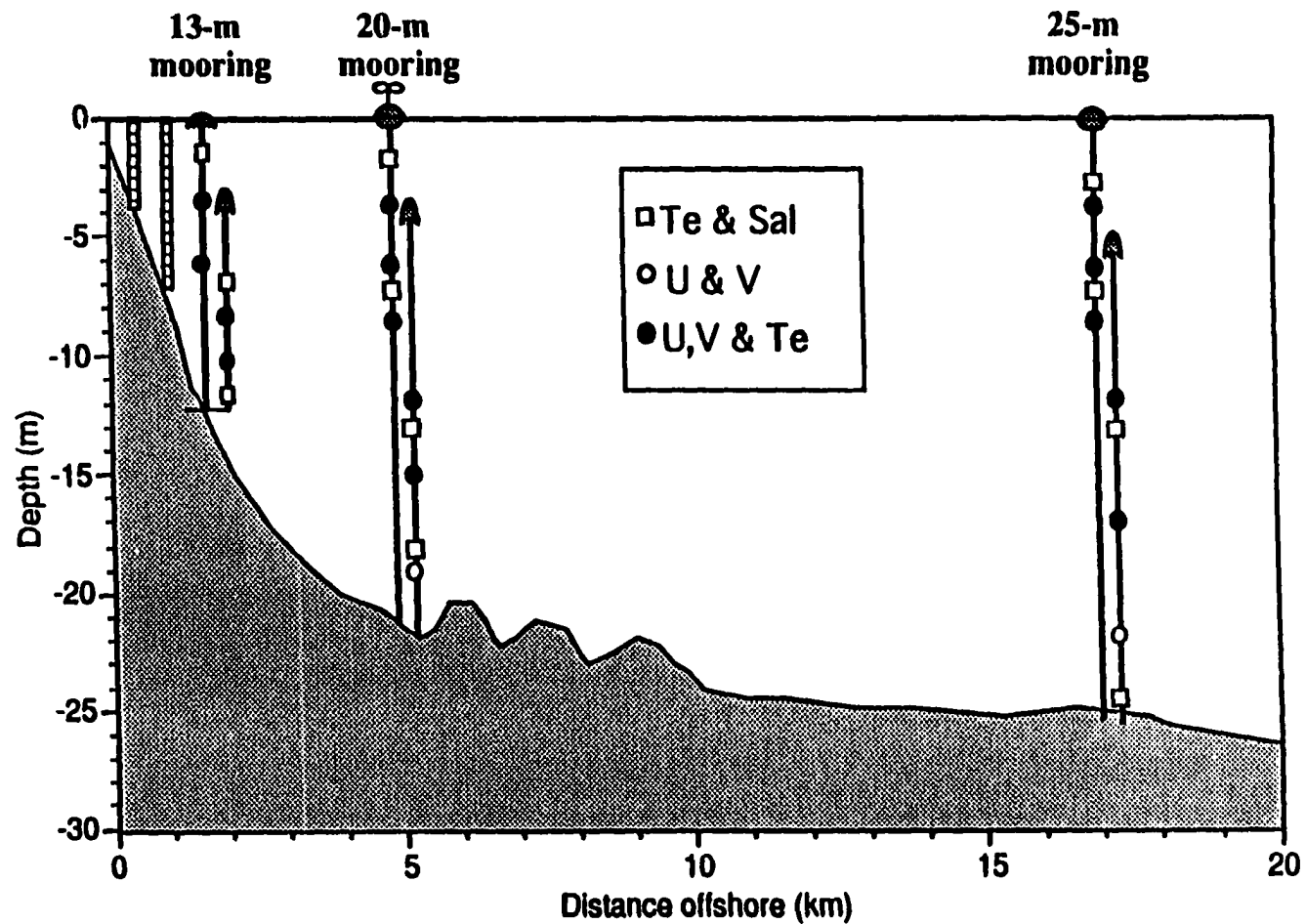


Figure 2.1. Diagram of the across-shelf mooring array (adapted from Alessi *et al* (1996), Figure 5.)

Figure 2.2. Instrument Location Map.

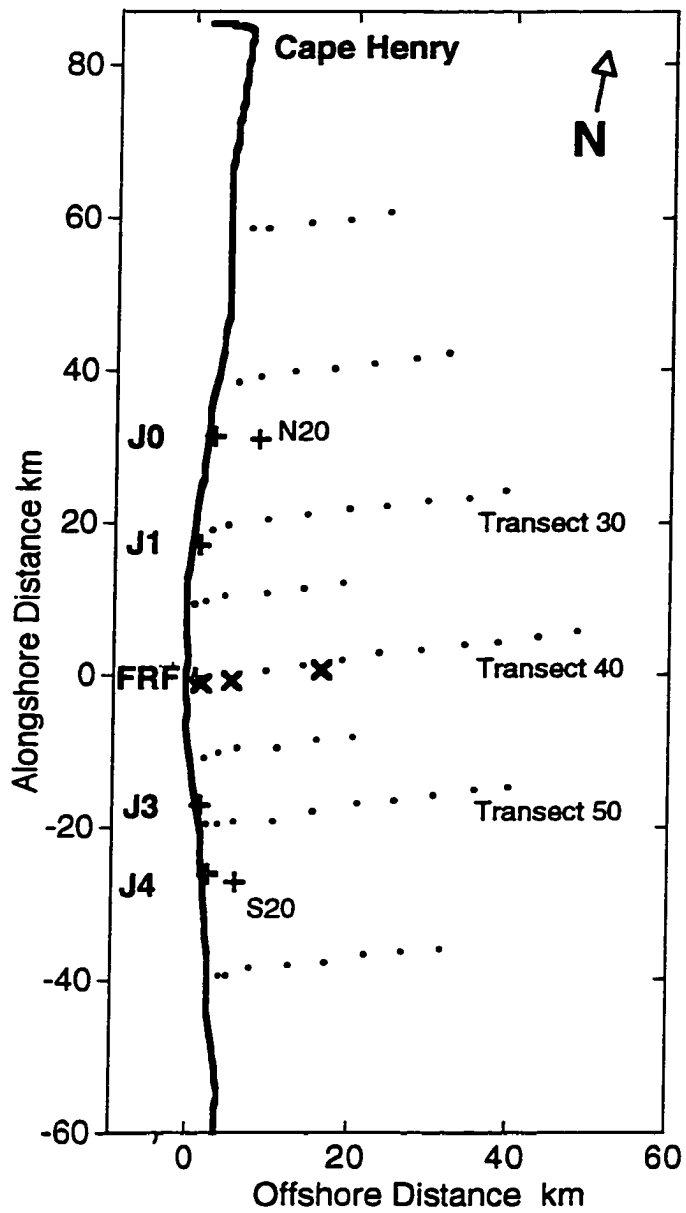


Figure 2.2. Instrument Locations

Chapter 3. Along-coast Propagation of the Plume

The arrival of low salinity water along the North Carolina coast 100 km south of the mouth of the Chesapeake Bay was observed during the summer and fall of 1994. The presence of the plume was episodic, with a new pulse occurring every 2 to 8 days. The low salinity intrusions propagated along the coast at speeds comparable to linear internal wave phase speed, except when strong downwelling wind conditions affected the intrusions and caused them to be in contact with the bottom. When not affected by upwelling winds, the fresher water was confined to within 7-9 km of the coast and constituted a surface layer about 8 m deep. Downwelling winds caused the plume to narrow and deepen whereas upwelling winds caused it to thin and spread offshore, eventually detaching from the coast. This buoyancy source was balanced by an along-shore current with a southward velocity of 30 to 70 cm/s, bounded by a region of high horizontal velocity shear at the offshore salinity front. The intrusions slowed during their passage through the study region, as mixing with ambient shelf water reduced the density contrast. The currents at the time of the intrusion arrival were consistent with properties of an internal gravity current under rotation.

In this chapter the along-coast propagation behavior is determined from detailed observations of the plume's density and velocity structure. The spatial characteristics of the low salinity intrusion are delineated and the influence of the wind on its shape is considered. Wind effects on the propagation speed are also estimated. Evidence for mixing between the plume and the ambient shelf water is presented, as well as the effect that this dilution has on the along-coast propagation speed. The last section focuses on the currents that are accelerated by the arrival of this buoyant water mass, and the velocity structure of its associated coastal current.

3.1 Introduction

The presence of estuarine water along the North Carolina coast is an episodic phenomenon. Figure 3.1 shows the complete hourly salinity time series from the 5-m isobath bottom-mounted SeaGauges along with the FRF pier salinity measurements and the local winds. The coordinate conventions used are positive northwards (towards 340° , v , y) and offshore (u , x). The salinity measurements alternately indicated values of 32 to 34 psu, which are representative of the Middle Atlantic Bight shelf waters (Boicourt, 1973), and those with a significant percentage of fresher Chesapeake Bay water included (26 to 30 psu). The times of lowest salinities were associated with periods of winds towards the south. There is variation at the semi-diurnal tidal frequency (e.g., J0 & J1 during 19-22 September) and at the 20-hour inertial frequency (e.g., 12-15 September); however the focus here is on sub-inertial variability - particularly on the meteorological synoptic time scale.

Over the three month study about 15 distinct low salinity events were observed, occurring at an average interval of 5 (± 2.6) days. This 2 to 8 day variability in the delivery of estuarine water to the North Carolina inner shelf is not explained by variations in tributary inflow to the Bay, which will be discussed in chapter 4. Pulses in the low salinity intrusion relate to fluctuations in the wind direction. In particular, Figure 3.1 shows that southward (downwelling) winds are associated with the presence of a low salinity plume, whereas northward (upwelling) winds are associated with the absence of low salinity water along the coast. The manner in which the Bay-shelf exchange is controlled by meteorology is explored in

chapter 4, while the wind-forced cross-shore movement of the intrusions is the subject of chapter 5.

The arrival of a new pulse of low salinity water moving southward along the coast is signaled by an abrupt drop in salinity at successive sensors. The time lag in arrivals at successive along-shore sensors is clearly illustrated in Figure 3.2. There are 6 discernible low salinity events (labeled A-F) during this August time period. These low salinity water masses are observed at the FRF pier 7 to 9 hours after their arrival at the J1 sensor, 17 km to the north. The initial appearance of the southward propagating front is manifest as a sudden drop of 2 to 3 psu within an hour. Subsequent freshening continued for a day or two, resulting in a total lowering of 4 to 6 psu from ambient shelf salinities.

Most of the low salinity intrusions which arrived during downwelling winds were preceded by a small drop in salinity. As soon as the winds turned to southward, there was a gradual lowering of salinity (about 0.2 psu hr^{-1}) due to downwelling of fresher surface water. This small drop in salinity due to onshore advection contrasted with the rapid $2\text{-}3 \text{ psu hr}^{-1}$ drop in salinity due to the along-shore movement of a new pulse of plume water. A few substantial drops in salinity (the most noticeable one on 12 September) were determined, by an examination of timing, to be due to onshore movement of a previous plume rather than due to the arrival of a new pulse.

The upper panel of Figure 3.2 shows the along-shore component of the local winds as recorded at the 20-m mooring on the central line. In these examples it is clear that some low salinity pulses traveled southward against opposing winds (event B, latter parts of A and E), while others were dispersed or pushed offshore before reaching the southern part of the

study region (event D). The strength and duration of the presence of fresher water was controlled by the wind, with downwelling conditions resulting in a sustained low salinity plume against the coast (event C).

In contrast to the progression in time of salinity decreases, large increases in salinity occurred simultaneously at all sensor locations. These salinity increases are interpreted as being due to upwelling. Ekman transport resulted in shoaling and offshore movement of the low salinity water, and will be examined in chapter 5. This Ekman transport appears to be the most effective mechanism by which the estuarine water is moved offshore and mixed with the shelf water. This is described further in the following section, where the anatomy of typical upwelling and downwelling scenarios is presented through a sequence of events in late August.

3.2. Description of Typical Upwelling and Downwelling Events

In Figure 3.3 the salinities and currents observed across the central line are detailed for a no-wind plume (event B), and a downwelling event (C), separated by a period of upwelling. Moderate winds blew for several days before 18 August, after which the wind relaxed through 20 August (Figure 3.3 middle panel). Late on 19 August, 11/2 days after the northward winds relaxed, a sudden salinity decrease was recorded at the J1 sensor located on the 5-m isobath, 16 km north of the FRF at Duck. Eight hours later, this low salinity water mass arrived at the FRF pier. Salinity dropped simultaneously at the pier and at the near-surface and mid-depth recorders of the 13-m mooring (1.5 km offshore), indicating a surface-trapped intrusion with a defined salinity front and a blunt shaped head.

The low salinity water did not extend out to the 20-m mooring 5.3 km offshore of Duck, although it did reach the 20-m mooring found 30 km to the north (see N20 in Figure 2.2). This buoyant surface layer moved southward rapidly. Current velocities as high as 0.8 m/s were recorded by the near-surface instrument on the 8-m tower and the 13-m mooring. Near-bottom currents were less than 0.3 m/s. No salinity or velocity signal associated with the plume were observed at the 20-m mooring on 20 August. Panel A of Figure 3.4 is a contoured salinity section from CTD profiles taken across Transect 50 located 20 km south of Duck. Overlaid are velocity vectors from simultaneous ADCP profiles, with the vectors oriented in plan view. The nearshore low salinity region has the same shape and velocity structure as that inferred from the moorings above. This narrow and shallow low salinity plume was continuous through the 60 km along-shore array of coastal sensors and, presumably, northward to its source at the mouth of the Chesapeake Bay.

Later in the afternoon of 20 August, the light winds became northward at 5 m/s and surface water velocities began to decrease immediately. A few hours later, surface salinities at the 20-m mooring dropped suddenly, indicating that the outer salinity front of the coastal plume had moved offshore beyond 5.3 km. The plume was shallower here, with no signal observed at the 7.6 m depth. The simultaneous, but gradual, increase in nearshore salinity (top panels of Figure 3.3) is consistent with this low salinity surface layer detaching from the coast and moving offshore. Panel B of Figure 3.4 from a CTD transect across the central line shows this thinner plume reaching 11 km offshore early on 21 August, with the lowest salinity water in the outer portion. By mid-day on 21 August, the near-surface salinity at the 25-m mooring decreased (not

shown), indicating that the plume water had moved over 17 km offshore. Late on 21 August, nearshore waters were destratified (Figure 3.4, panel C) and low temperatures indicated that this water had upwelled as the plume moved offshore. Consistent with an upwelling scenario, northward velocities were observed nearshore.

The onset of southward (downwelling) winds on 23 August produced a low salinity intrusion with somewhat different characteristics: a southward current was set up with the wind and an immediate small decrease in nearshore salinity occurred. This salinity decrease was observed also at depth on the 13-m mooring and is due to the onshore movement and downwelling of lower salinity surface water left a short distance offshore by the previous mild upwelling conditions. This downwelling circulation, which can be seen clearly in the cross-shore velocity components presented in the upper panel of Figure 3.5, led to a decrease in near-bottom salinity at the 20-m mooring later on 23 August.

Shortly after noon on 23 August (over a day after the northward winds ceased) a much larger and more sudden decrease in salinity occurred as a new intrusion of low salinity water propagated down-coast from the Chesapeake Bay. As before, the salinity dropped simultaneously at the pier and the 13-m mooring. In this case, however, the low salinity water extended to the bottom at the 13-m isobath. At the same time, the southward current accelerated suddenly, attaining a speed of 90 cm/s near-surface. The downwelling circulation pattern seen in the cross-shore velocities (Figure 3.5) was disrupted at the arrival of the plume, as buoyancy-driven dynamics dominated the flow. The arrival of new low salinity water re-established stratification that had been eroded by the previous downwelling circulation (Figure 3.3, upper panels). Low salinity

water was not observed at the 20-m mooring until 24 August following a decrease in the southward wind. A number of salinity increases and decreases were observed at the near-surface sensor on the 20-m mooring and at the near-bottom sensor on the 13-m mooring over the next two days. These fluctuations in shape of the plume may have been directly forced by the wind, or they could be symptomatic of the meandering of the outer edge of the plume as the wind forcing decreased. During these two days, with persistent southward winds, the nearshore salinity steadily decreased, reaching a minimum of 28 psu. With the reversal in wind direction on the morning of 26 August, the southward currents decreased rapidly and the nearshore salinity increased. In this case there was a definite lag between salinity increases (and in the velocity reversal) recorded at the 8-m, 13-m and 20-m isobaths.

3.3. Cross-shore Spatial Structure

Summarizing from analyses of each event, similar to those described above, an estimate is made of the cross-shore dimensions of the plume off Duck, a distance of 84 km south of the source. The near-surface salinity sensor on the 13-m mooring nearly always showed a freshening very similar in intensity and timing to that on the pier. However, the sensor at 7.6-m depth on this mooring usually recorded a weak to moderate freshening, unless the low salinity intrusion was backed by downwelling conditions. The near-surface sensor on the 20-m mooring seldom recorded a strong lowering of salinity until a later stage. Thus there is a general picture of a low salinity water mass that, at the time of its arrival, was confined to less than 8 m depth and 5 km width, unless

significantly modified by the wind. Downwelling winds act to narrow and deepen the plume whereas upwelling winds tend to widen and thin this plume, eventually detaching it from the coast.

The spatial resolution of the mooring time series can be improved by incorporating the shipboard CTD and underway system data. In Figure 3.4a&b the salinities from nine CTD casts taken across plume 'B' are shown. The plume is delimited in the vertical by a pycnocline (halocline) region where the stratification is several times stronger (here buoyancy frequency $N=0.12 \text{ s}^{-1}$) than either in the low salinity intrusion above, or in the ambient water underneath. The offshore extent of the plume was similarly delimited by a maximum in the horizontal density (salinity) gradient, recorded in the underway surface data. These fronts were often visible owing to surface expressions such as foam lines. The low salinity water inshore of the front and above the pycnocline exhibited strong southward velocity, as recorded by the concurrent ADCP measurements. The variation of density at the inshore stations was controlled completely by salinity; the plume showed no thermal signal.

The average thickness of the plume was determined by the depth of the pycnocline for all CTD casts that had a surface salinity less than S_{maxplume} , the maximum salinity associated with the plume intrusions. S_{maxplume} had a decreasing value with time, being defined as

$$S_{\text{maxplume}} = 31.8 - 0.018 * (\text{days since Aug 1}^{\text{st}})$$

which averages 31.5 psu in August, decreasing to 30.5 psu in October. Only profiles from transects where low salinity water was present at the shore-most station were used, i.e. occasions when the plume was attached to the coast (lenses of detached low salinity water separated from the coast, e.g. Figure 3.4c, were not included). There was a weak tendency for

shallower plumes to prevail in the northern (upstream) part of the study area; however all CTD casts from the 100 km along-shore survey region are combined and presented in Figure 3.6a. This clearly shows a tendency for the plumes to be thicker nearer to the coastal boundary.

These buoyant intrusions occupy the upper water over the inner shelf only part of the time. How commonly this structure occurs can be determined by the percent of time that the instruments on the cross-shore moorings record salinities less than S_{maxplume} (Figure 3.6b). During the entire three month study period, a low salinity plume was present in the surface layers of the very inner shelf (within 5km of the shore) over half the time. Deep plumes, reaching close to the bottom, occurred only a quarter of the time.

A seasonal difference in the plume thickness is revealed in Figure 3.6a, with deeper pycnoclines evident in October. Approximately 20% of the October profiles indicate that the low salinity plume filled the water column inshore, as opposed to less than 10% in August. The average plume thickness was 6.4 m in the summer (August) and 8.2 m in the fall (October). The effectiveness of wind control on the plume thickness is reflected in Figure 3.7a. Under upwelling conditions, the plume is generally less than 8 m deep, whereas under downwelling conditions the plume is typically thicker than 10 m. Also during upwelling, the stratification in the underlying pycnocline is enhanced, as shown in Figure 3.7B, where the buoyancy frequencies of the pycnoclines are plotted against recent along-shore wind stress. The increased pycnocline strength for the thinner plumes indicates that during this stage, wind-driven advection is dominating over mixing in determining the disposition of

the plume. Weak downwelling wind stress both deepens the plume and weakens the stratification.

These wind effects suggest that seasonal difference in plume thickness could be attributable to the seasonal difference of the winds: the Middle Atlantic Bight experiences southwesterly (upwelling) winds during the summer, switching to stronger northeasterlies (downwelling) in the fall. Figure 3.8 is the histogram of winds recorded at the FRF during the CoOP program, where the magnitude within directional (true) bins is weighted by frequency of occurrence. The wind is polarized in a NE-SW manner, so that winds from the north tend to have an onshore component, while those from the south are associated with offshore winds. These cross-shore components reinforce, through direct frictional effects, the Ekman-driven downwelling and upwelling patterns.

The width of the plume was determined from the position of the seaward salinity front which was crossed repeatedly during ship surveys. Transects taken in the southern reaches of the study region; or those taken across the head of an arriving intrusion indicated narrower plumes than those sampled farther to the north, or well behind the leading portion. In Figure 3.7c, attention is given to the control of the plume width by the wind. During upwelling winds the plume widens substantially, attaining widths of well over 15 km, even for mild upwelling winds. Note from Figure 3.7a that all these wide plumes were also relatively thin (< 8 m). Again, only plumes that were still in contact with the coastline (have not separated to form a lens) are included in this plot. During downwelling winds the plume is typically less than 9 km wide. The plume width response to the input of along-shore wind stress will be modeled in sections 5.3 and . Note that the tendency for narrower plumes under

stronger downwelling winds reverses as the wind stress increases over -0.1 Pa. These plumes had likely been downwelled to contact the bottom and have entered a diffusive phase.

Under weak downwelling conditions a wide range of pycnocline depths were recorded (Figure 3.7a). This variability in thickness could have been due to a variation in upstream source strength (see chapter 4). Under strong downwelling conditions, however, all plumes were deep and narrow, frequently reaching to the bottom. The average cross-sectional area implied by all the depth-width pairs was about $64,000 \text{ m}^2$.

The pycnocline marking the lower boundary underlying the plume had an average stability frequency of $N_{\text{max}} = 0.1 \text{ s}^{-1}$ in August (period of ~ 1 minute) and $N_{\text{max}} = 0.08 \text{ s}^{-1}$ in October, comparable to a salinity increase of 1.5 psu across one meter depth. While this is not as strong as highly stratified plumes such as those of the Amazon or Mississippi, it may be sufficient to consider this as a two-layer system, in spite of the shallowness of the region. In that case the theoretical width scale of the plume, indicating an inviscid balance between buoyancy and rotation, would be the internal radius of deformation, R_{int} (Gill, 1976),

$$R_{\text{int}} = \sqrt{\frac{g \Delta \rho H_{\text{plume}} (H_{\text{total}} - H_{\text{plume}})}{\rho H_{\text{total}}}} \frac{1}{f} \quad (\text{eq. 3.1})$$

where H_{plume} is the plume thickness and f is the Coriolis parameter. An alternate formulation more appropriate to the deeper plumes (where $H_{\text{plume}} > H_{\text{total}}/2$), would be $R_{\text{int}} = (N_{\text{av}}/f) * H_{\text{total}}$, with the buoyancy frequency N_{av} computed from the top to bottom density difference, ($N_{\text{av}} = \sqrt{\frac{g \Delta \rho}{\rho H_{\text{total}}}}$). The average R_{int} computed from the CTD profiles (one estimate for each cross-plume transect) indicates a 4.1 km e-folding

width, which compares reasonably with the total average observed width, based on concurrent offshore frontal measurements, of 9.1 km.

The ratio (squared) of the internal radius R_{int} to the observed width forms the Burger number $S_{Bu} = \left[\frac{R_{int}}{L_{obs}} \right]^2 = \frac{1}{K^2}$, described in section 1.3.4 as a measure of the influence of buoyancy in a rotating system. Garvine (1995), using a form of the Burger number to classify coastal plumes, points out that those with S_{Bu} of order unity have the most complicated dynamics, both stratification and rotation being important. The CoOP observations yielded an average $S_{Bu} = 0.37$, ratios having been computed individually for each transect. The Chesapeake plume observed here was moderately stratified, with Burger numbers about twice as large as those calculated for the downstream coastal jet region of the Delaware plume (Münchow and Garvine, 1993). Münchow and Garvine conclude that the Delaware plume is continually widened by the diffusion of relative vorticity through bottom friction, whereas the CoOP width measurements indicate a tendency for narrower plumes to be observed in the farthest downstream region of the study area. An examination of the range of S_{Bu} in CoOP shows that the lower values are correlated with upwelling winds, consistent with the observation that it is the surface stress which modifies the width of the plume off Duck. This relationship is explored further in section 5.3.

3.4. Along-coast Propagation Speed and Wind Effects.

Over the 3 months of observations, 15 low salinity fronts were tracked traveling down the coast (Figure 3.1). The along-shore positions of

these intrusions are plotted in Figure 3.9 as a function of time, using as $t=0$ the moment of arrival of the initial large drop in salinity at sensor J0. From the frontal travel times between successive sensors, the along-coast propagation speed over ground, C_{obs} , can be calculated. In order to estimate the rate of frontal movement relative to the ambient water, the concurrent shelf flow velocities, measured just outside of the plume region, are subtracted from C_{obs} to estimate the relative propagation speed, C_{adj} . The ambient shelf flow was estimated taking 6 hour averages from the current meter in the middle of the water column at the 13-m mooring (prior to any acceleration due to the buoyancy). The hypothetical position of a front traveling at a steady speed of 55 cm/s is also plotted in Figure 3.9.

The linear internal wave speed ($C_{int} = N_{av} * H_{total}$ or $\propto \sqrt{g \frac{\Delta\rho}{\rho} H}$) was calculated for each event, based on the density differences $\Delta\rho$ observed at the 13-m mooring during the passage of the intrusion front. C_{int} estimates were also made by assuming that the $\Delta\rho$ recorded during a front arrival at the 5-m sensors was a reasonable representation of a top to bottom $\Delta\rho$, as well as from the pycnocline $\Delta\rho$ measured by a few CTD profiles taken in the head of an intrusion (eq 3.1). These estimates of C_{int} are compared with the observed C_{adj} in Figure 3.10. The observed along-coast relative propagation speeds, C_{adj} , appear to scale with the predicted $\sqrt{g \frac{\Delta\rho}{\rho} H}$ velocities and range from 50% to 120% of the C_{int} magnitude. From the mooring estimates, an average C_{int} of 55 cm/s was obtained. This is compared with the observed C_{adj} between J1 and J3 of 38 cm/s (49 cm/s in the northern region and 28 cm/s in the southern region). The ratio of C_{adj}/C_{int} , proposed by Chao (1988a) as a measure of dissipation, has a mean value of 0.7. As for the Burger Number, this ratio can indicate the

relative importance of frictional effects. Within Chao's plume classification scheme, the plume observed at Duck would fall in the non-diffusive category. However, in the southern, downstream portion of the study region, the observed propagation speed becomes an increasingly smaller fraction of the internal wave phase speed, indicating that the buoyancy terms are losing their dominance to frictional terms (note J3 and J4 locations in Figure 3.9).

The observed intrusion speeds, C_{adj} , do not agree well with the numerical experiments of Chao (Chao and Boicourt, 1986, Chao 1987, 1988a), or with Kourafalou et al. (1996). All these models show progression of the low salinity intrusion along the shelf at speeds no greater than 10 to 17 cm/s, even for plumes with fresher salinities than were observed here, and for the full range tested of vertical mixing and bottom friction parameterizations. These model plumes would take over 4 days to reach Duck from the mouth of the Chesapeake Bay, rather than the 1 1/2 to 2 day travel time implied by the CoOP'94 observations. This is most likely due to the models' inability, given limited vertical resolution, to reproduce the strong pycnocline that was commonly observed separating the plume from the underlying waters. This intense stratification probably insulates the intrusion from the effects of bottom stress, allowing the nearly inviscid propagation speeds observed in the northern part of the study region, where the observations indicate that C_{adj}/C_{int} is close to unity. For most of the plumes modeled by Chao, that ratio is less than 0.25 (Chao, 1988a), indicative of a diffusive character.

An additional possibility is that the meteorologically-controlled surge-like nature of the Bay-shelf exchange, which is examined in chapter 4, produces intermittent periods of enhanced buoyant discharge larger

than the moderate levels tested by the modelers. These numerical experiments also do not include the effects of wind on the plume, while the majority of the observed events experienced southward directed wind stress. Adjusting the measured propagation speeds by the ambient shelf flows corrects for this to some extent, but there could be preferential acceleration of the surface-trapped plume layer by the wind (see section 5.3).

Downwelling winds should accelerate the plume both through direct frictional effects and by the increased layer thickness contribution to the buoyancy forcing (larger H_{plume}). The additional southward velocity produced by an assisting wind would be sheared, providing enhanced delivery of the surface-most water towards the front, where it can replenish the density deficit that drives the gravity current, which is continually being eroded by detrainment near the nose (Stern et al., 1982). To examine the wind effects on Cobs, Figure 3.11 presents the over-ground velocities of the intrusion front against the effective wind stress (calculated according to Large and Pond, 1981). For low to moderate wind stress ($< 0.1 \text{ Pa}$), the water column remained stratified, as was seen in Figure 3.7b. The magnitude of Cobs increased with southward directed wind stress, and decreased with opposing winds, as was expected. However, for strong southward directed winds, the frontal propagation speeds were noticeably slower. As discussed in section 3.3 above, these strongly downwelled plumes fill the water column; they are not as decoupled from the bottom stress by stratification and consequently their dynamics are more controlled by friction. A two-layer model scenario is not appropriate for these cases. Looking at the relative propagation speeds, C_{adj} , these intrusions travel at less than 20 cm/s above ambient shelf flow

speeds, indicating the diminished importance of the buoyancy. During these events the fresher water appears less as a sharp front, its more gradual arrival due partly to southward advection by wind-driven flow in high-energy conditions.

If one examines the relative along-coast propagation speeds as they proceed through the study region (Figure 3.12A), leaving out the strong downwelling events dominated by bottom friction, there is a clear slowing trend as the intrusion moves farther away from its source. This tendency appeared in Figure 3.9 as increasing travel times for the southern sensors, J3 and J4. Damping by bottom friction is a possible explanation for the observed decrease in speed. This behavior was noted in Chao's models (1988a), where he related it to the exponential decay of intrusion speeds observed in laboratory gravity current studies (Griffiths and Hopfinger, 1983) which attributed the momentum loss to inertial wave radiation for small Ekman number intrusions, and to frictional dissipation for larger Ekman numbers. These laboratory studies also report on the mixing along the gravity currents' path, indicating the concomitant dilution and reduction in buoyancy forcing as the intrusion slows.

The evidence for dilution of the plume's estuarine water with shelf water is presented in Figure 3.12B. The minimum salinity observed at each 5-m isobath sensor for each event is plotted. These salinity measurements reveal that the minimum plume salinity observed for most events increases with distance down-coast. The average rate of increase was 0.052 psu per km ($\pm 0.027\sigma$). Since the sensors are 1 m from the bottom, it is possible that they are measuring a turbulent layer that is more subject to mixing than the core of the plume proper; however, this does not appear to be a large effect as surface observations from the along-

shore mooring array show similar increases. The salinity deficit of the intrusions entering the study area has a wide range which could be due both to differences in freshwater flux from the Bay and to mixing conditions encountered upstream. However the rate of increase within the Duck region is steady. Over the 1 1/2 day passage through the study area, a typical plume rises from a salinity of 25.5 to 29 psu. With an ambient shelf salinity of 33 psu, this indicates a dilution of 1:1 over the 60 km path. The relationship between salinity contrast and propagation speed for the observations are shown in Figure 3.13. In spite of the scatter, the trend shows slower C_{adj} corresponding to increasingly diluted plume intrusions. Overlaid on Figure 3.13 is the theoretical phase speed of a linear internal wave in a two-layer system where the density difference is due solely to the salinity contrast $C_{int} = \sqrt{\frac{g \Delta \rho}{\rho} H_{plume}}$ where $\Delta \rho = \beta \Delta Sal$ and $\beta = 0.764$ is a representative value of the contraction coefficient of salinity for this range of temperature (Fofonoff and Millard, 1983). Note with regard to the next section, that this is also the velocity scale exhibited by baroclinic gravity currents (Benjamin, 1968).

During downwelling, the erosion of stratification by this dilution would be enhanced both by the more energetic wave regime associated with the onshore wind component and by bottom-generated turbulence where the low salinity layer deepened to reach the bed. Strongly downwelled plumes have lower dilution rates than the other events, perhaps having been more strongly mixed upstream of the study region. In some moderate downwelling events, the plume appears to shift between the two dynamical modes (from two layer to an unstratified plume in contact with the bottom) during its passage through the study region. During the event of 22-25 August (Event C in Figure 3.2) relative

propagation speeds decrease from nearly 40 cm/s in the northern part down to less than 4 cm/s by J4 - barely faster than the ambient shelf flow . The decrease in salinity observed at J4 is noticeably more gradual than at sensors farther north for this event. The front presumably had been eroded by the enhanced mixing of increased downwelling conditions.

To estimate the varying relative contributions of terms in the along-shore momentum balance one might start with the assumption that on the inner shelf the dominant balance will be between wind stress, τ_S , and bottom stress, τ_B . Indeed, estimates for these terms calculated from local winds (Large and Pond, 1981) and near-bottom currents (using a quadratic formulation with $C_d=0.002$) are correlated with an $r^2 = 0.61$, with a best fit if τ_B is lagged 5 hours behind the wind. This relationship was stronger during times that the plume is not present: the r^2 increases to 0.74 when we exclude pairs corresponding to times when FRF salinity is less than $S_{\max\text{plume}}$. To examine the relative contribution of the plumes' buoyancy, we estimate the baroclinic pressure gradient as $\frac{gH_{\text{plume}}^2}{2\rho_0} \frac{\partial\rho}{\partial y}$ with H_{plume} fixed at 8 m . The density time series from the sensors at J1 and FRF was used to calculate the along-shore density gradient, using their along-coast separation (16 km) as the length scale. While the absolute magnitude of these dynamical terms are dependent on several poorly known parameters, one can compare how the friction and buoyancy terms vary during the field study (Figure 3.14). The friction terms are dominant and the expected balance between surface and bottom stress is clear in September and especially in October. However, there are events when the buoyancy term is making a comparable contribution, and even times (23 Aug., 2 Sep.) when the bottom stress appears to be balancing a combination

of wind and buoyancy (downwelled plume "C" and the first part of event "F"). The surface-trapped plumes (e.g. 16, 20 & 31 Aug.) show no response in bottom stress and are balanced by acceleration (Figure 3.5, lower panels). These momentum balances are examined in greater detail by Lentz et al., (1998).

3.5. Currents

Having established the characteristics and structure of the low salinity water mass, I now focus on the details of the current associated with its presence. When the gravitational spreading of a buoyant water mass under rotation is constrained by a lateral boundary, a boundary current must develop in which the offshore pressure gradient is balanced against the onshore Coriolis term (Gill, 1976). The presence of the coastline to the right of the flow (in the northern hemisphere) results in a coastal jet that can transport the estuarine outflow long distances from its source (Csanady, 1976). During the CoOP'94 field work, strongly enhanced southward currents were commonly observed at the inshore stations and were associated with low salinities. Figure 3.15 is a map of ADCP and CTD data during a late October survey where the velocities inshore of the 30 psu surface isohaline are 2 to 3 times faster than the ambient shelf flow. Winds during the preceding day had been moderate towards the southwest; throughout the survey they were light and variable. This survey highlights the inability of ship-based measurements to capture, synoptically, the rapidly evolving plume behavior -- this plume event entered the study region while the ship was in the southern portion, and was not encountered until the middle transect. Figure 3.4B presents an

example where southward flow is maintained within the plume while the rest of the inner shelf is turning to the north under the influence of upwelling winds. The horizontal shear across the offshore frontal region was frequently as high as 40 cm/s per km.

In Figure 3.5 are plotted the hourly along-shore and cross-shore components of velocity measured at the 13-m mooring located on the central line at Duck and the along-shore component from the 8-m tower during the same 3 week period as in Figure 3.2, where the salinities are shown. For clarity, only the surface and bottom current meters are displayed. The arrival of the head of each low salinity intrusion (marked as events labeled A-F as in Figure 3.2) was associated with accelerating southward surface velocities growing by 30 to 40 cm/sec within an hour time. These strong accelerations were also observed inshore at the 4-m tower (not shown). The enhanced southward velocities continue throughout the periods of low salinities.

The flow during the plume arrival displays non-linear features consistent with an along-shore momentum balance at the nose between inertia and buoyancy (Griffiths and Hopfinger, 1983). The maximum hourly average velocities measured by the 8-m and 13-m surface current meters on the central line during the plume arrivals commonly exceeded the over-ground along-shore frontal propagation speeds C_{obs} by 15 to 30%. In Figure 3.16 two example patterns in velocity and salinity are shown. Fluid velocities greater than the rate of advance of the feature imply convergence towards the front which initially deepens the head, forming the head wave or roller region identified in numerical gravity current models (Kao et al., 1977) and in field observations (Luketina and Imberger, 1987). These higher velocities were confined to the very surface and near-

coast region. For a few shallow and narrow plume events, the high velocities were observed only at the 8-m isobath. They persisted for over 1 to 3 hours, or, at average propagation speeds, for a distance of several kilometers behind the nose, implying an extensive convergence zone. This surface convergence requires downwelling with flow reversal at the bottom (the "top-spin" at the nose described by the Chao and Boicourt (1986) model), in addition to lateral detrainment and widening. The gravity current laboratory experiments show this lateral detrainment taking place largely in the form of billow and eddies shed from the seaward side of the nose (Stern et al., 1982). The vertical resolution of the mooring time series does not allow us to evaluate whether a head wave deeper than the following plume was a common feature of these intrusions, however, several ADCP/CTD transects recorded a deeper faster plume in earlier downstream crossings of an arriving plume, compared to those taken an hour or so later slightly farther upstream. Widths inferred from both the moorings and underway system indicate that the head has a somewhat narrower cross-shore extent than the coastal current behind it, consistent with the laboratory observations.

Other evidence in support of this model of behavior is the reverse deeper currents excited by the passage of the head of the intrusion. In contrast to the southward acceleration of the surface velocities observed in Figure 3.5, the bottom sensors record a brief northward pulse at the moment of passage. These "backwards" accelerations were clearest for depths that showed a slight freshening, in keeping with the top-spin model of nose advancement. At or just before the frontal passage, an offshore pulse of flow was recorded at all depths. This is qualitatively consistent with a model of seaward lateral detrainment at the nose. Both

the offshore and deeper northward flow are observed only at the moment of frontal passage -- once the head has passed, a southward current exhibiting strong vertical shear is set up.

Several cross-sections of the along-shore jet associated with a plume event were recorded during a ship survey in late October (Figure 3.16). The middle panel (Transect 35) is located approximately 14 km behind the southward-propagating nose; the bottom panel (Transect 30) is taken farther north and several hours later when the nose would be about 29 km to the south. The salinity contours are based on CTD profiles (positions marked with arrows). The velocity contours in the lower panel are from an ADCP tow averaged to 1 minute intervals, which gives a horizontal resolution of 0.25 km. In the upper panel, ADCP profiles were taken at the CTD locations. In the transect closer to the head (middle panel) the velocity maximum was found at the innermost profile. Farther upstream (bottom panel), the current broadened and the core was located between 2 to 3 km offshore, coincident with the freshest portion of the plume. The core of the southward-flowing jet remained inshore of the frontal region as defined by either the CTD or surface salinities (Figure 3.16, top panel). For a fully geostrophically-adjusted coastal current, the fastest velocities would be in the frontal region where the horizontal gradients are strongest. This pattern was frequently observed in the CoOP'94 transects that recorded arriving plumes: the velocity maximum would be located well inshore of the front, closest to the minimum salinity .

The observed southward velocities were maintained over the inner shelf in the low salinity water mass until the salinities rose as the plume moved. Even after the plume detaches from the coast, southward momentum persisted within the low salinity water mass for up to a day.

In Figure 3.4C this is detected as a region of depressed northward velocities.

When the plume arrives during winds from the north (e.g. events C and F), the pronounced downwelling pattern in the cross-shore components is disrupted (Figure 3.5, top panel). The new plume re-imposes strong stratification on the water column that had been vertically mixed by the previous downwelling circulation. It should be noted that the presence of a large source of fresher surface water, as was provided by the previous plume event B, caused the inner shelf to destratify very rapidly at the onset of downwelling winds, and resulting in the strong bottom currents observed on 23 August (Figure 3.3). The largest resuspension event in August was observed at this time.

CTD transects taken during strong plumes that oppose upwelling winds (e.g. event A or B) display upraised isotherms just offshore of the salinity front, which then flatten shoreward under the plume water (Waldorf et al., 1995, p 177, 237). Thus the arrival of a plume intrusion is seen to modify the cross-shore circulation patterns, as well as the along-shore, displacing both upwelling and downwelling flows over the inner shelf.

3.6. Summary and Conclusions

Field observations recorded during the summer and fall of 1994 show that the episodic presence of low salinity water masses from the Chesapeake Bay created an intermittent baroclinic coastal current along the North Carolina coast. Under low wind conditions, this current

occupied the upper half of the water column within 7 to 9 km of the coast. The plume was bounded by a distinct southward-propagating front, a region offshore of high horizontal salinity and velocity gradients, and a strong pycnocline underneath. The intrusion traveled along the coast at a speed proportional to the linear internal wave speed or $\sqrt{g \frac{\Delta\rho}{\rho} H}$. This is also the pertinent velocity scale for baroclinic gravity currents (Benjamin, 1968). The width of the arriving head of the intrusion was somewhat narrower than the coastal current region behind it. Southward winds acted to narrow and deepen the intrusion, causing it then to contact the bottom. This contrasts with the Delaware plume, which Münchow and Garvine (1993) concluded filled the entire water column unless significant northward winds forced it to shoal. Comparison of observed widths and speed to theoretical values indicate that the Chesapeake plume here is not as subject to dissipative bottom friction or mixing as either the Delaware plume or numerically modeled low salinity intrusions of the Middle Atlantic Bight.

The inner shelf flow is largely controlled by wind forcing, as is the shape, position, and propagation speed of the plume. Within this wind-dominated context, the buoyancy forcing associated with the arrival of a low salinity intrusion makes a significant contribution to the surface inner shelf currents. Several events in August and September displayed buoyancy currents which prevailed against the ambient wind-driven flow. Increased wind and wave energy in later autumn result in a diminished role for the buoyancy forcing. The plume events generally last for 1 to 4 days and occur at intervals of 2 to 8 days; accordingly, low salinities were recorded near shore during 50% of the field program.

Propagation speeds were seen to slow during the passage of each intrusion through the study region. It is proposed that this is due to the mixing with ambient water along the path of the intrusion which steadily increased its salinity, thereby reducing the density contrast that drives it. Deep, downwelled plumes had particularly slow propagation speeds due to increased control by bottom friction.

Figure 3.1. Complete hourly salinity time series from sensors along the 5 m isobath, with wind vectors from FRF (vector pointing up indicates stress directed towards 340° true).

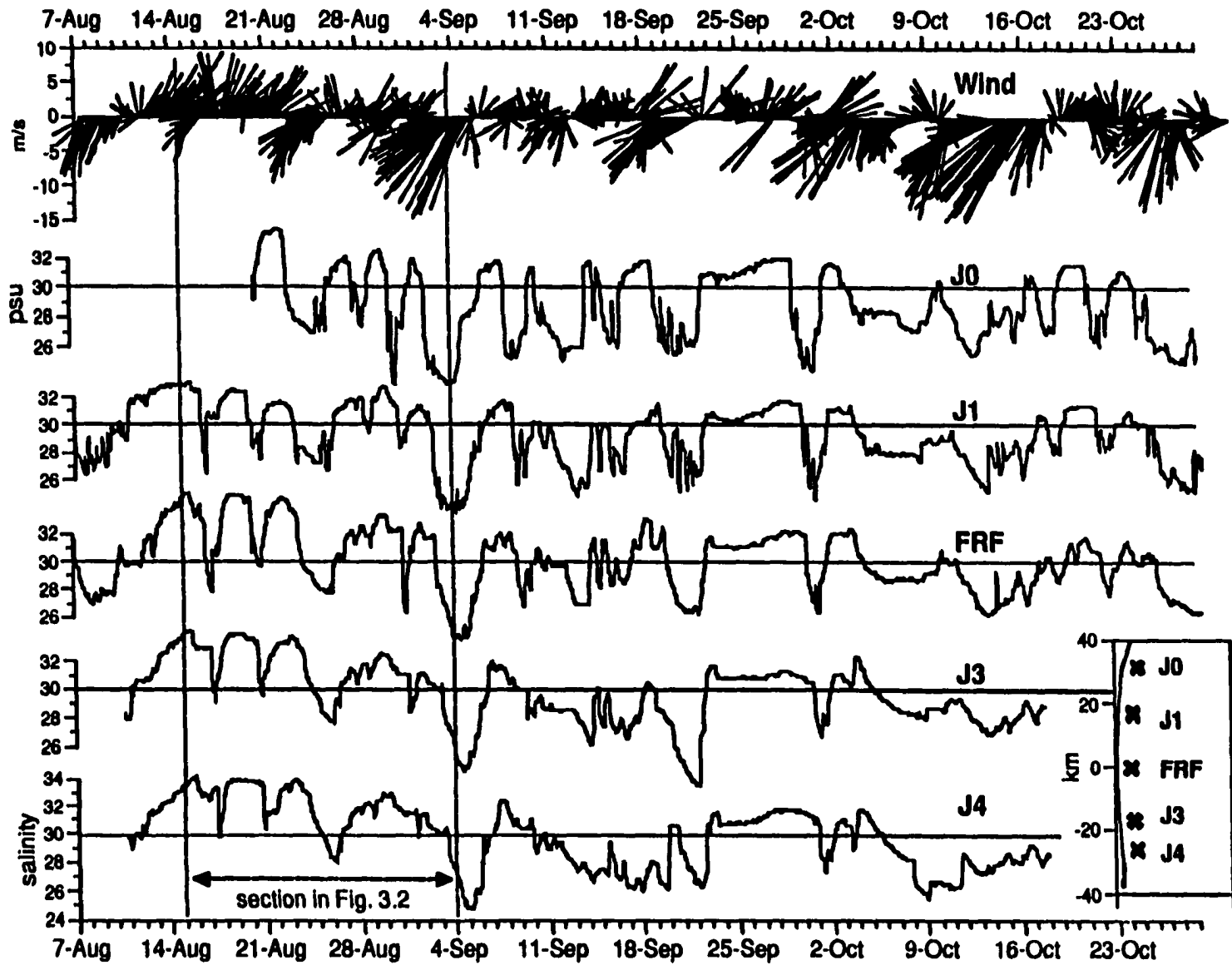


Figure 3.1. Complete salinity time series from sensors along 5 m isobath, with wind vectors from FRF in direction of stress.

Figure 3.2. Hourly time series of (upper panel) along-shore wind measured at a height of 3 m on the surface buoy of the 20 m isobath mooring, and (lower panel) salinity measurements from SeaCATs mounted at 1 m above the bottom along the 5 m isobath, along with salinity from 4 m depth at the FRF pier

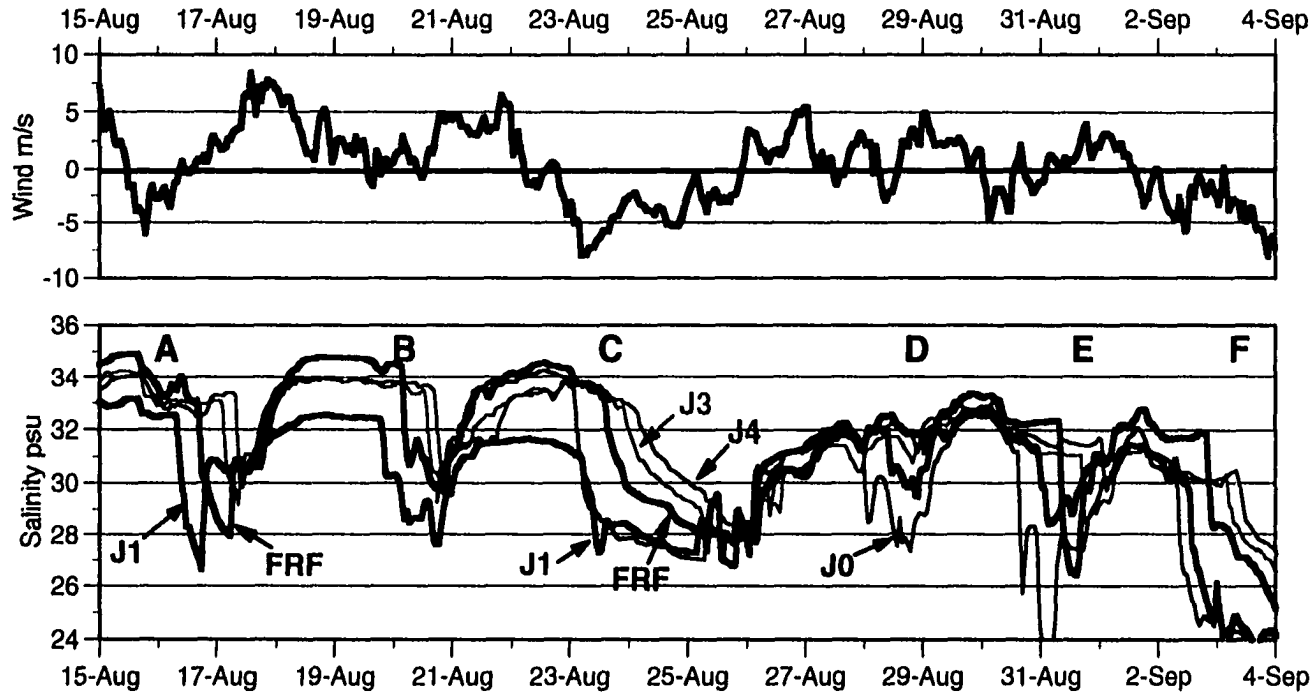


Figure 3.2. Hourly time series of (upper panel) alongshore wind measured at a height of 3m on the surface buoy of the 20m isobath mooring, and (lower panel) salinity measurements from SeaCATs mounted at 1m above the bottom along the 5m isobath, along with salinity from 4m depth at the FRF pier.

Figure 3.3. Surface and bottom salinity and along-shore current from the 8-m, 13-m, and 20-m moorings. Winds from meteorological buoy on 20-m mooring.

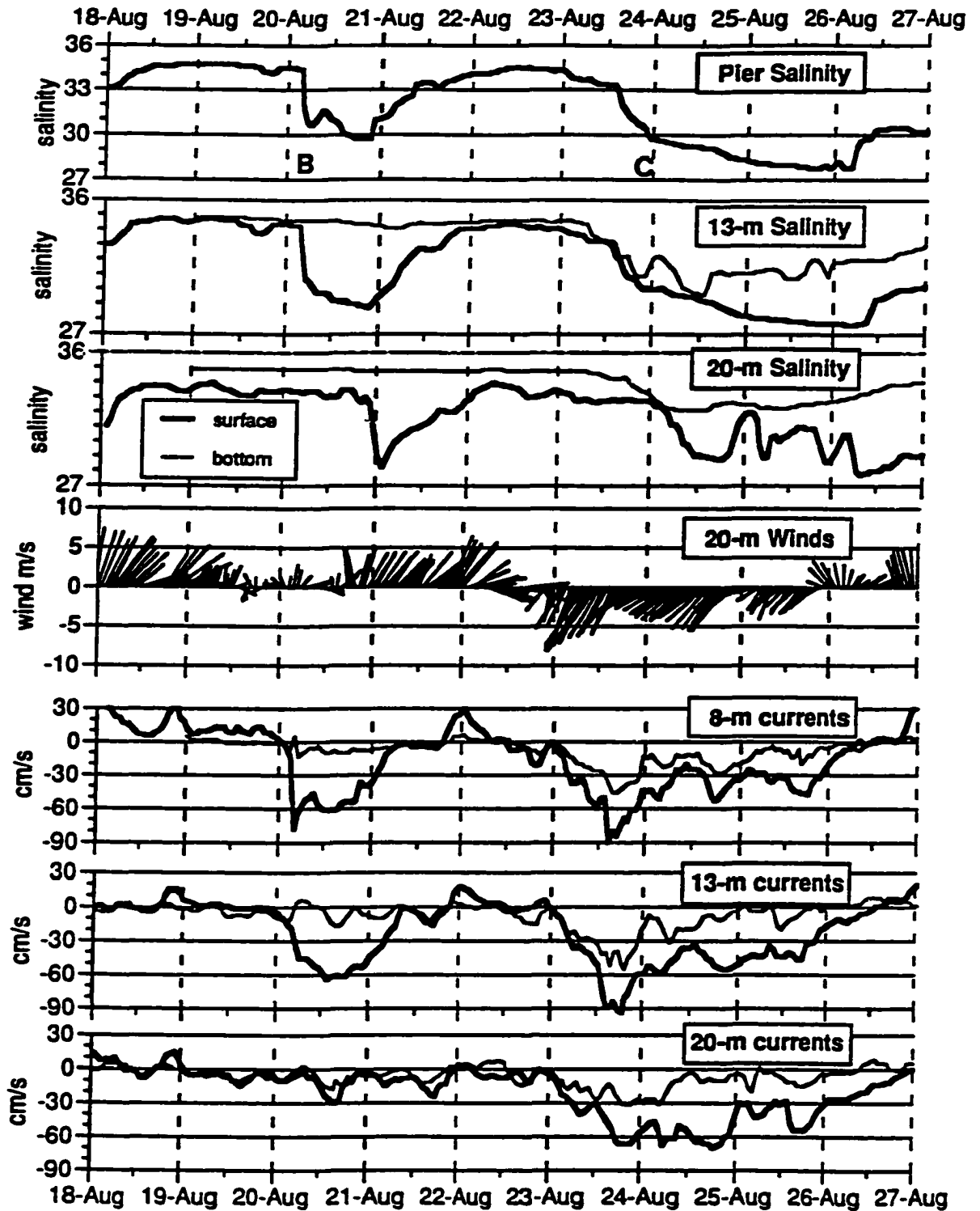


Figure 3.3. Surface and bottom salinity and alongshore current from the 8-m, 13-m, and 20-m moorings. Winds from meteorological buoy on 20-m mooring.

Figure 3.4. Vertical cross-shore sections of CTD salinity (colorscale) overlaid with detided ADCP velocity vectors from Transect 50 (panel A) and Transect 40 (panels B and C). Velocity vectors are oriented as in plan (map) view, with the velocity scale indicated by the arrow in the lower left-hand corner of each plot.

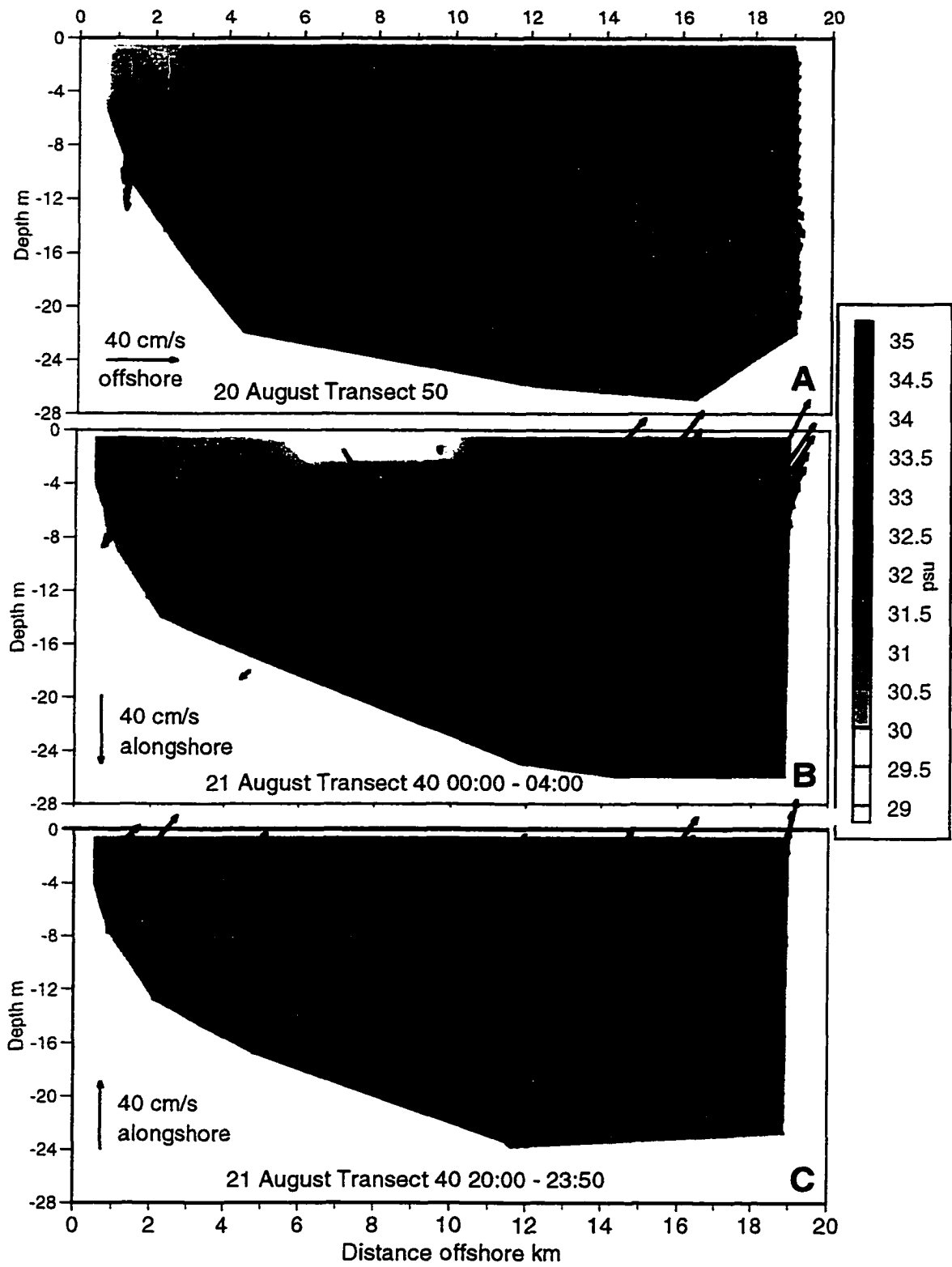


Figure 3.4. Vertical cross-shore sections of CTD salinity overlaid with detided ADCP velocity vectors from Transect 50 (panel A) and Transect 40 (panels B and C). Velocity vectors are oriented as in plan view.

Figure 3.5. Hourly currents from same 3 week period as Figure 3.2 measured at the 8-m tower and 13-m mooring: Cross-shore components from surface and bottom (top panel), along-shore components (lower two panels).

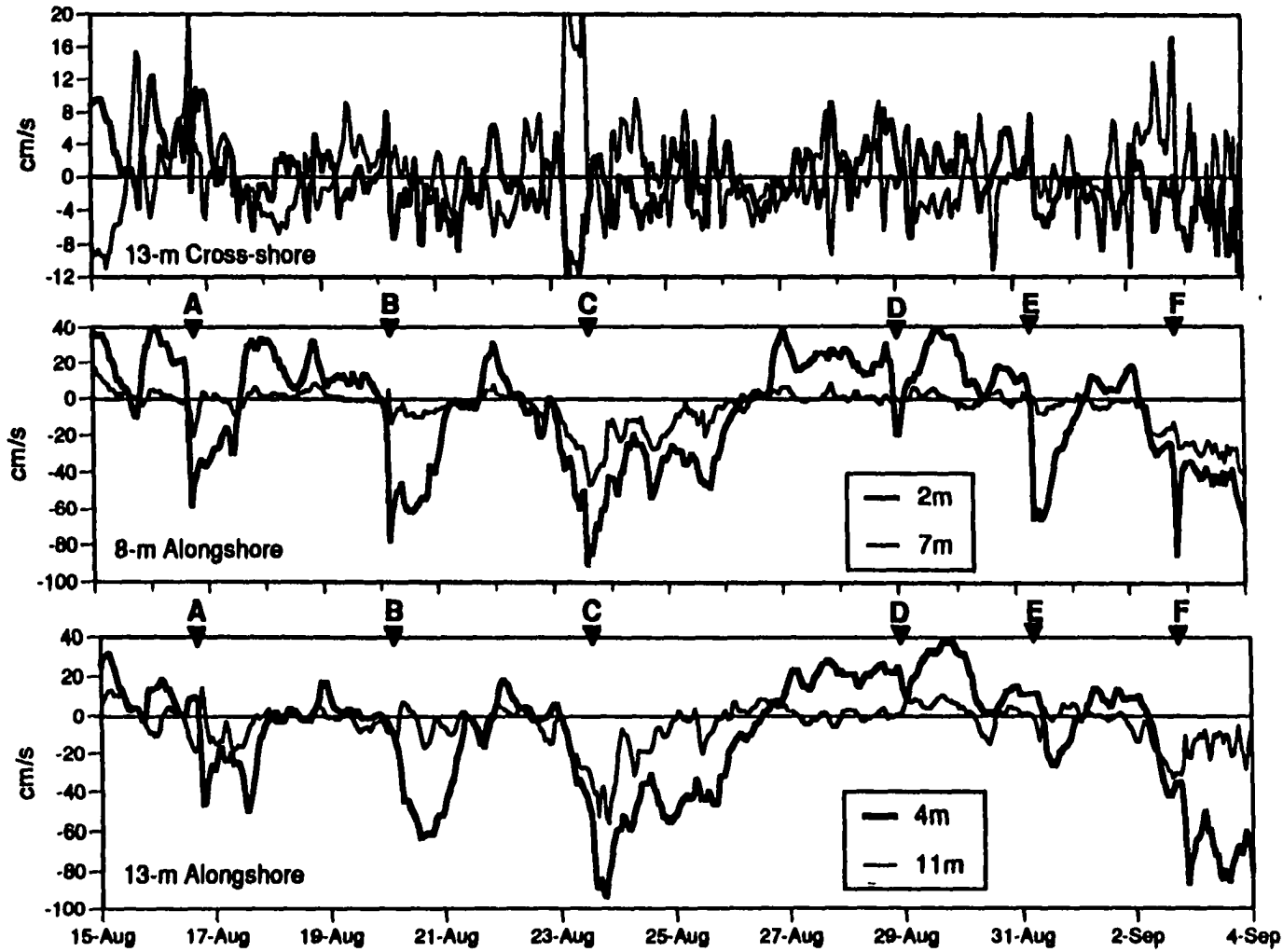


Figure 3.5. Hourly currents from same 3 week period as Figure 3.2 measured at the 8-m tower and 13-m mooring: Cross shore components from surface and bottom (top panel), alongshore components (lower two panels).

Figure 3.6. A) Thickness of plume (depth of maximum pycnocline from all CTD profiles where the surface salinity $< S_{\text{maxplume}}$). B) %time plume water is present at moorings.

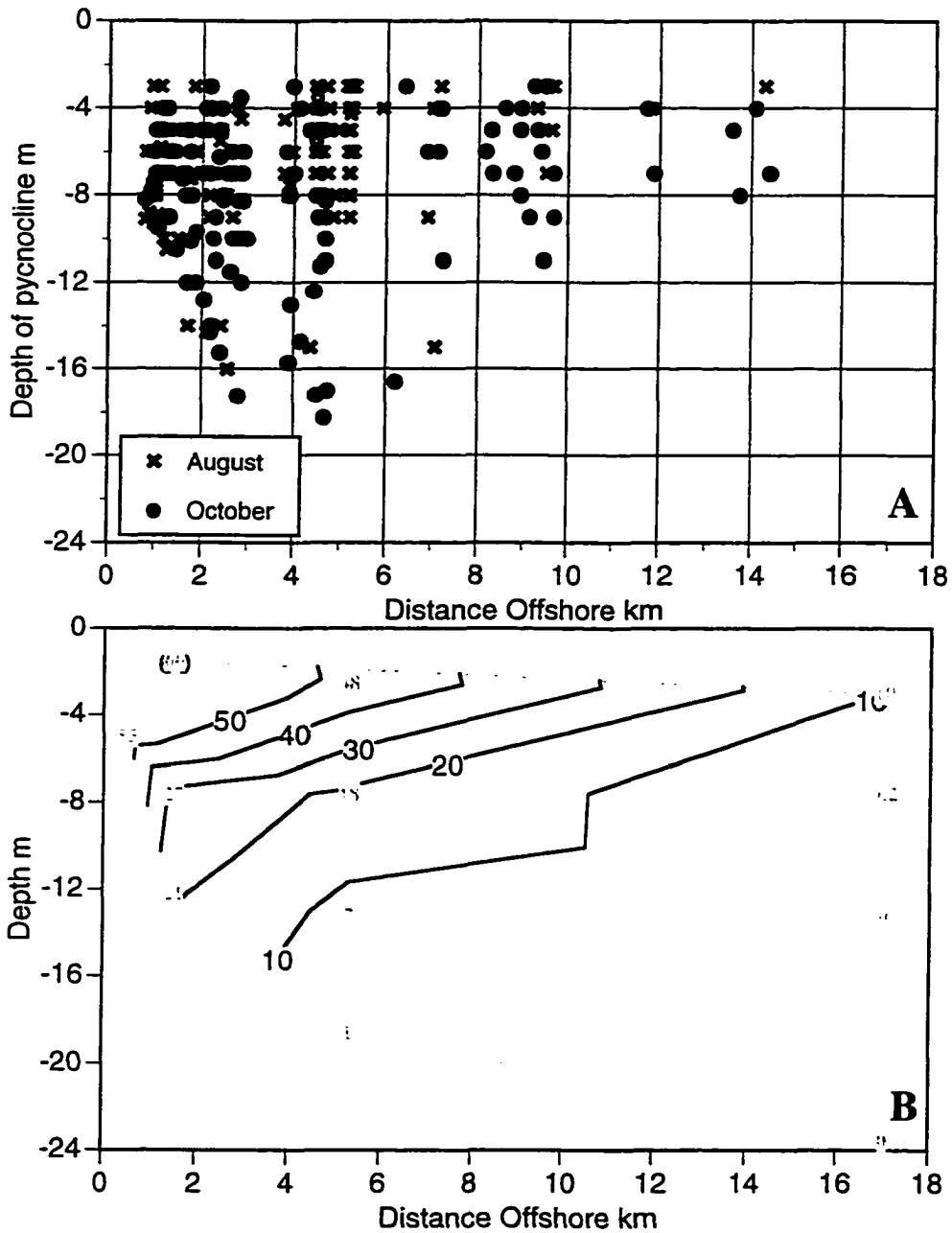


Figure 3.6. A) Thickness of plume (depth of maximum pycnocline from all CTD profiles where the surface salinity $< S_{maxplume}$). B) Percent of time that low salinity water was present.

Figure 3.7. A) Thickness of plume as determined by depth of maximum pycnocline (from stn 2) and B) strength of the stratification in the underlying pycnocline (maximum buoyancy frequency) ; and C) width of plume as determined by offshore locations of high surface salinity gradients from shipboard underway observations *versus* recent along-shore wind stress (average of previous 6 hours).

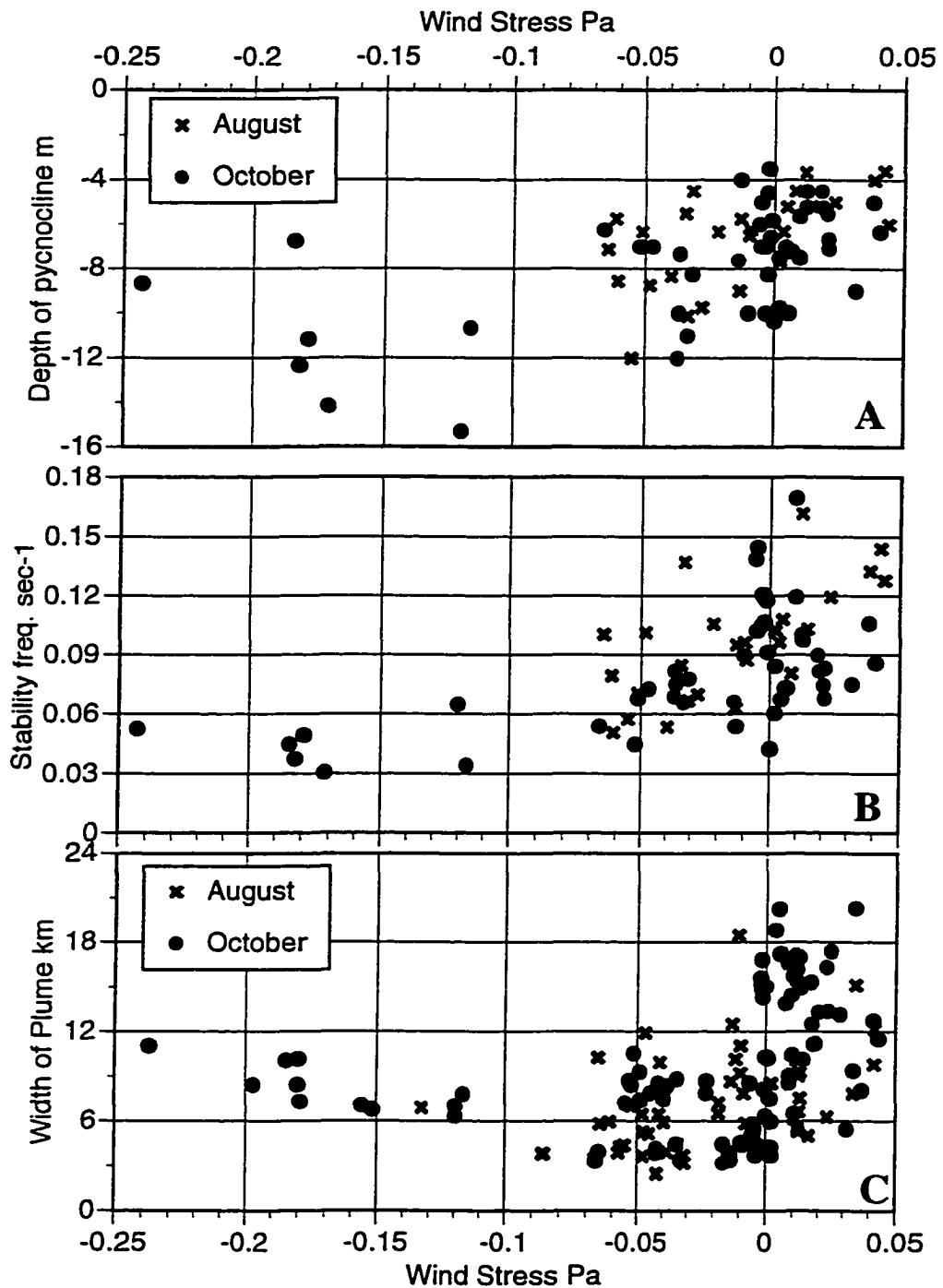


Figure 3.7. Alongshore wind stress (average of previous 6 hours) *versus*
 A) Thickness of plume as determined by depth of maximum pycnocline (at stn 2);
 B) strength of the stratification in the underlying pycnocline (maximum buoyancy
 frequency) ; and C) width of plume as determined by offshore locations of high
 surface salinity gradients from shipboard underway observations.

Figure 3.8. Histogram of FRF wind direction (true) weighted by magnitude. The coastline near Duck is oriented approximately 340° - 160° .

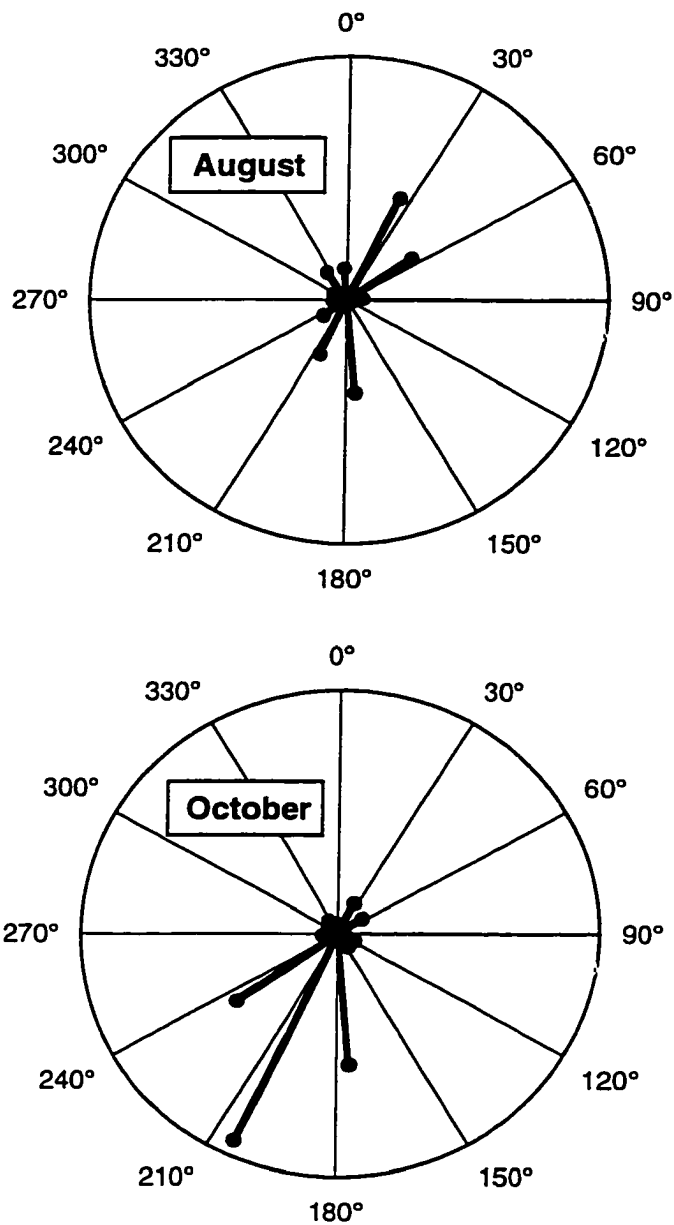


Figure 3.8. Histogram of FRF wind direction (true) weighted by magnitude. The coastline near Duck is oriented approximately 340° - 160°.

Figure 3.9. Position of southward propagating front of low salinity intrusion *versus* time in days since reaching sensor J0. Travel times were computed as relative to ambient flow. Solid line indicates position of a disturbance traveling at a constant phase speed of 55 cm/s. Dashed lines indicate ranges for phase speeds of 75 cm/s and 35 cm/s.

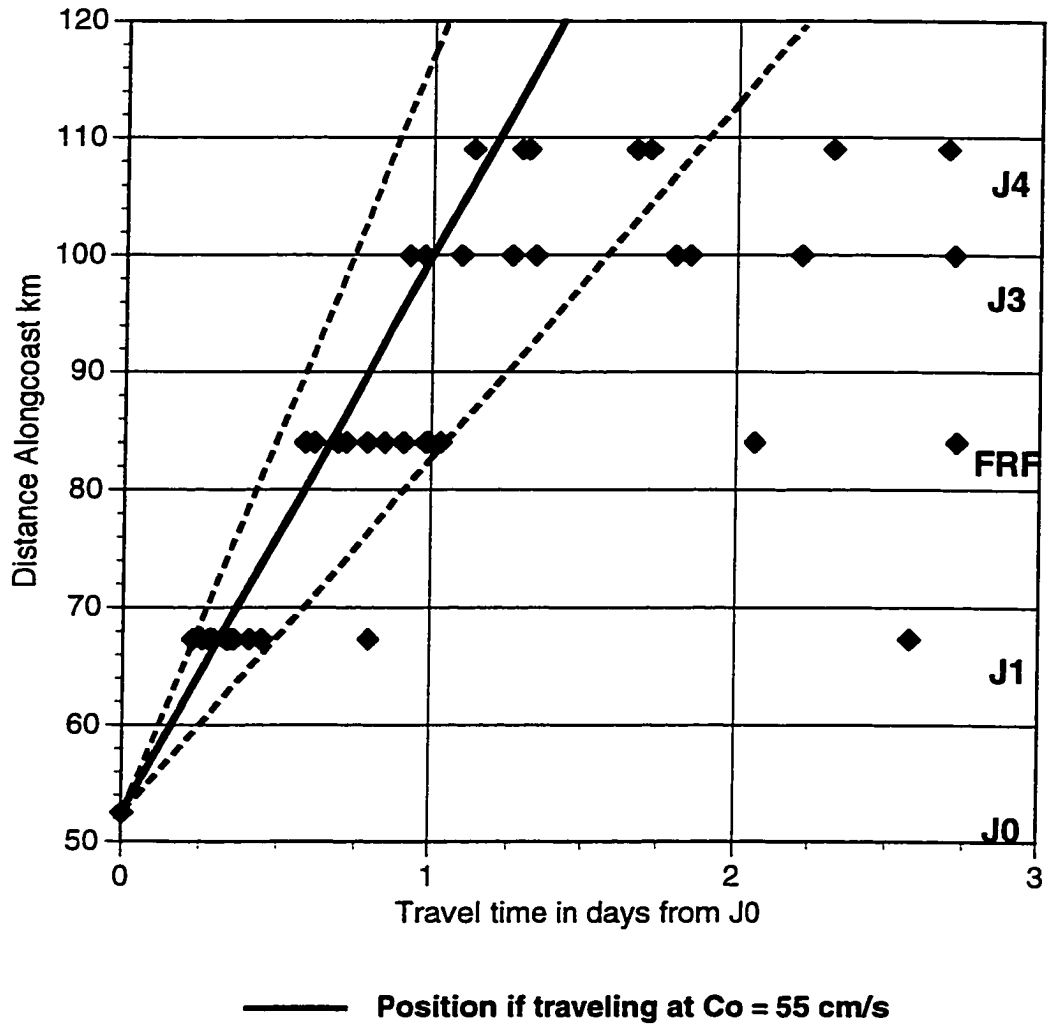


Figure 3.9. Position of southward propagating front of low salinity intrusion *versus* time in days since reaching sensor J0. Travel times were computed as relative to ambient flow. Solid line indicates position of a disturbance traveling at a constant phase speed of 55 cm/s. Dashed lines indicate ranges for phase speeds of 75 cm/s and 35 cm/s.

Figure 3.10. Observed propagation speed (C_{adj}) compared with theoretical linear internal wave phase speed (C_{int})

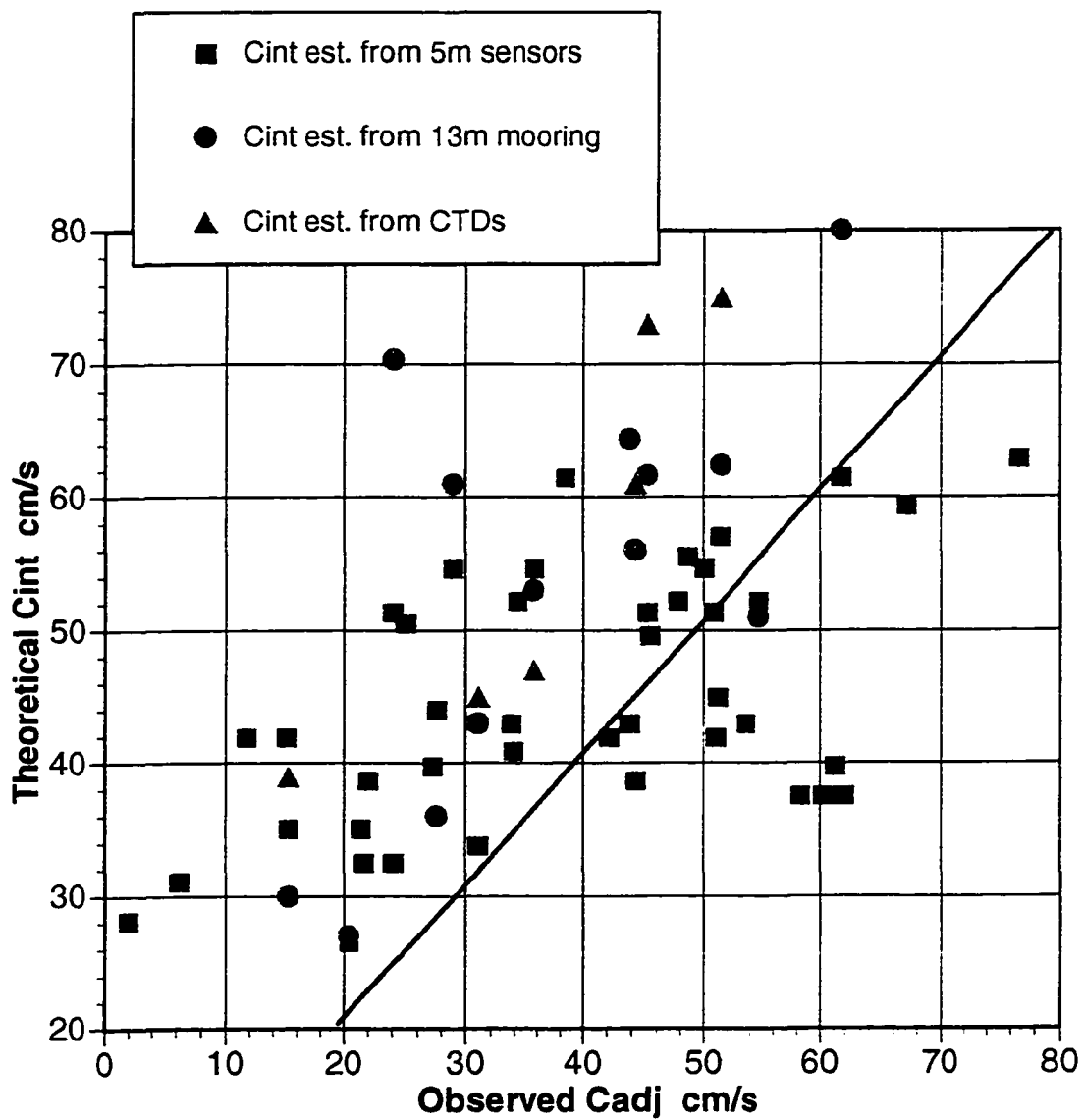


Figure 3.10. Observed Propagation speed of intrusion (C_{adj}) adjusted for ambient flow compared with theoretical linear internal wave phase speed scale (C_{int}).

Figure 3.11. Velocity (over-ground) of low salinity intrusion *versus* recent wind stress (average of previous 10 hours). Symbols indicate pairs of sensors between which the intrusion speeds were determined: box = J0 to J1; circle = J1 to FRF; triangle = FRF to J3; diamond = J3 to J4.

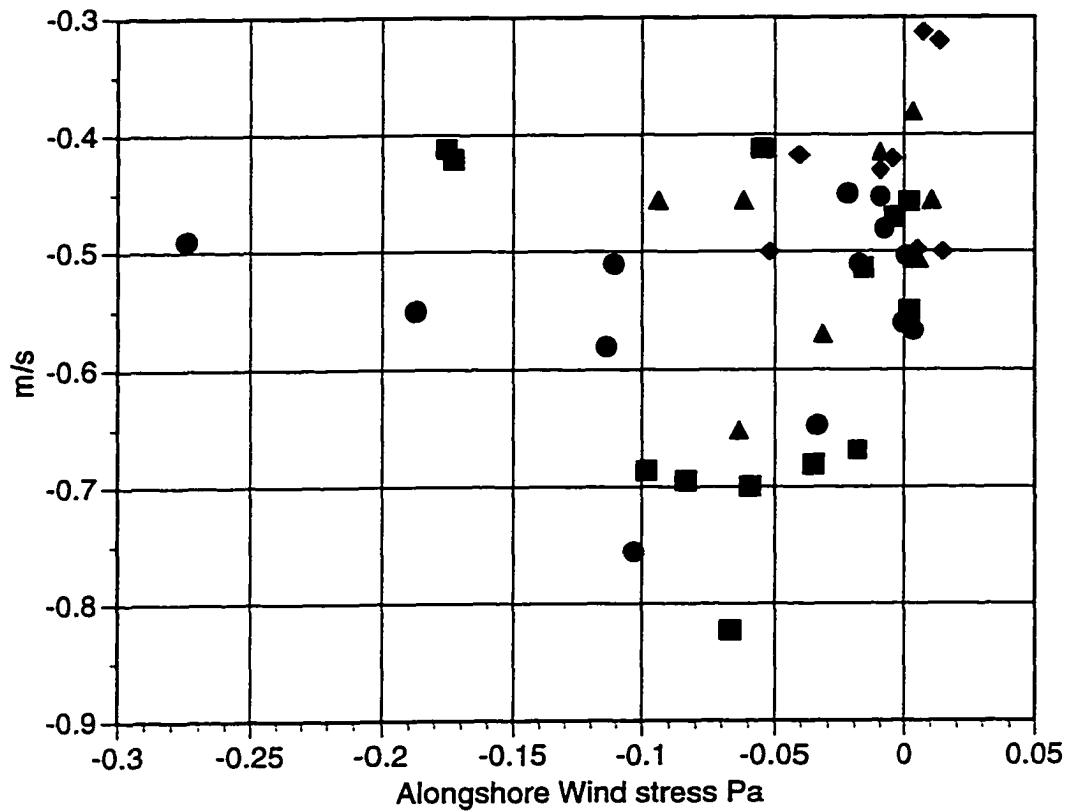


Figure 3.11. Velocity (over-ground) of low salinity intrusion *versus* recent wind stress (average of previous 10 hours). Symbols indicate pairs of sensors between which the intrusion speeds were determined: box = J0 to J1; circle = J1 to FRF; triangle = FRF to J3; diamond = J3 to J4.

Figure 3.12. A) Observed propagation speed C_{adj} (determined incrementally between pairs of salinity sensors and adjusted for ambient shelf flow) *versus* alongshelf distance from Chesapeake Bay. B) Minimum observed salinity for each event at each along-coast sensor.

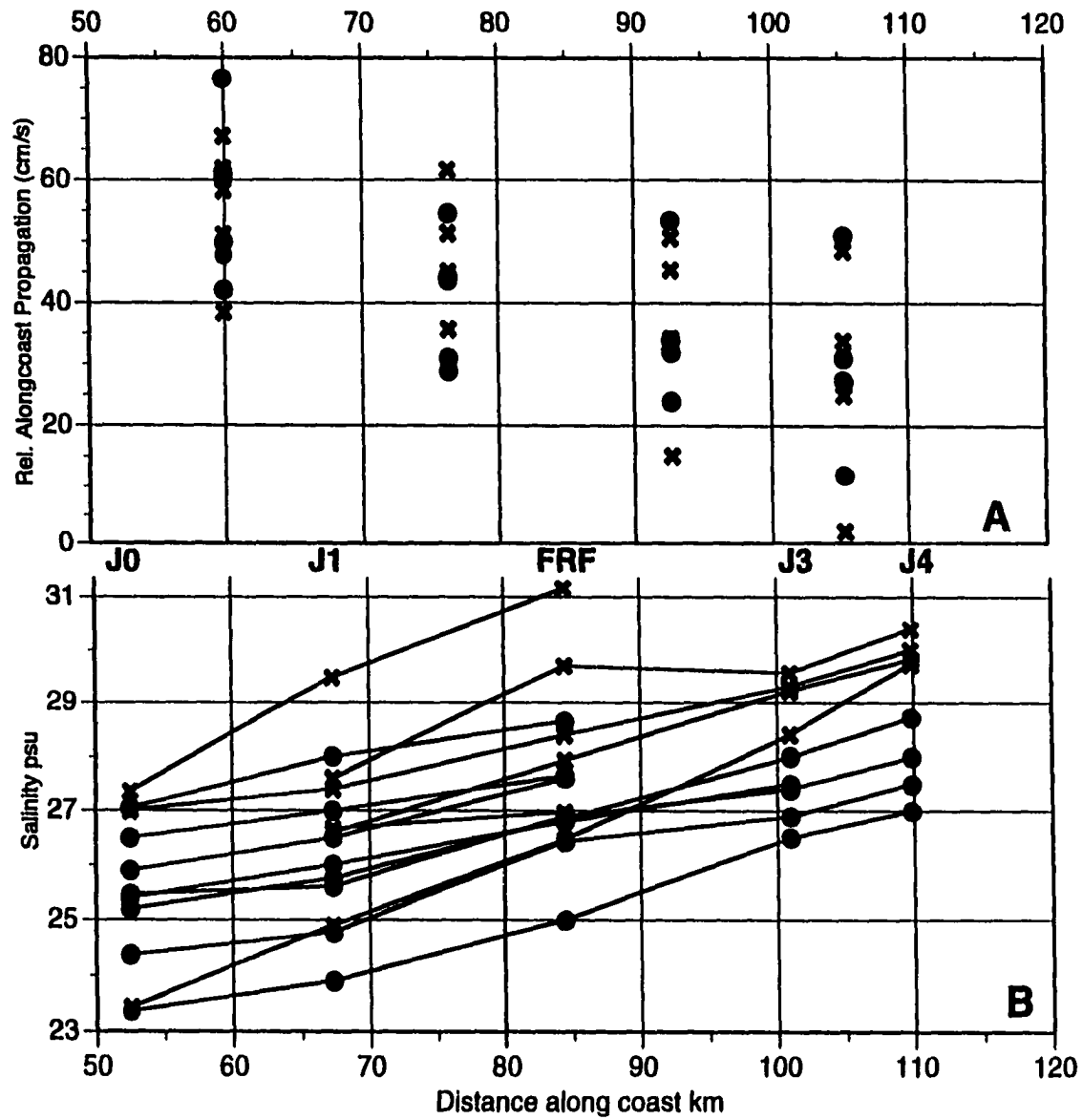


Figure 3.12. A) Observed propagation speed C_{adj} versus alongshelf distance from Chesapeake Bay. B) Minimum observed salinity for each event at each alongcoast sensor.

Figure 3.13. Relative along-coast propagation speed versus ΔSal , the decrease in salinity observed at the arrival of the plume. Solid line is linear internal wave speed $C_{\text{int}} = \sqrt{\frac{g \Delta\rho}{\rho} H_{\text{plume}}}$ where $\Delta\rho = \beta \Delta\text{Sal}$ and $\beta = 0.764$ is the contraction coefficient of salinity. (The average H_{plume} of 7m was used.)

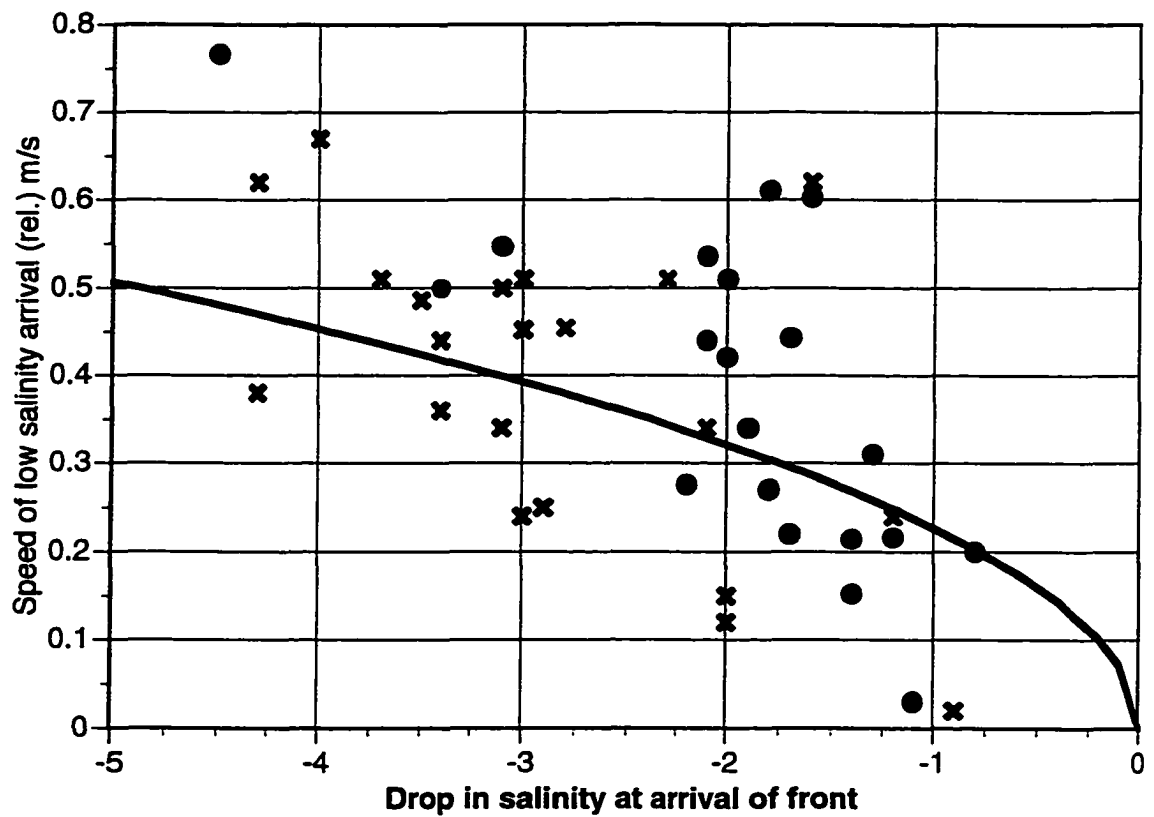


Figure 3.13. Relative alongcoast propagation speed C_{adj} versus ΔSal (the decrease in salinity observed at the arrival of the plume). Solid line is linear internal wave speed $C_{int} = \sqrt{(g \cdot \beta \cdot \Delta Sal / \rho) \cdot H_{plume}}$ where ρ is the ambient water density and the salinity contraction coefficient $\beta = 0.764$.

Figure 3.14. Time series of surface stress, bottom stress and along-shore baroclinic pressure gradient.

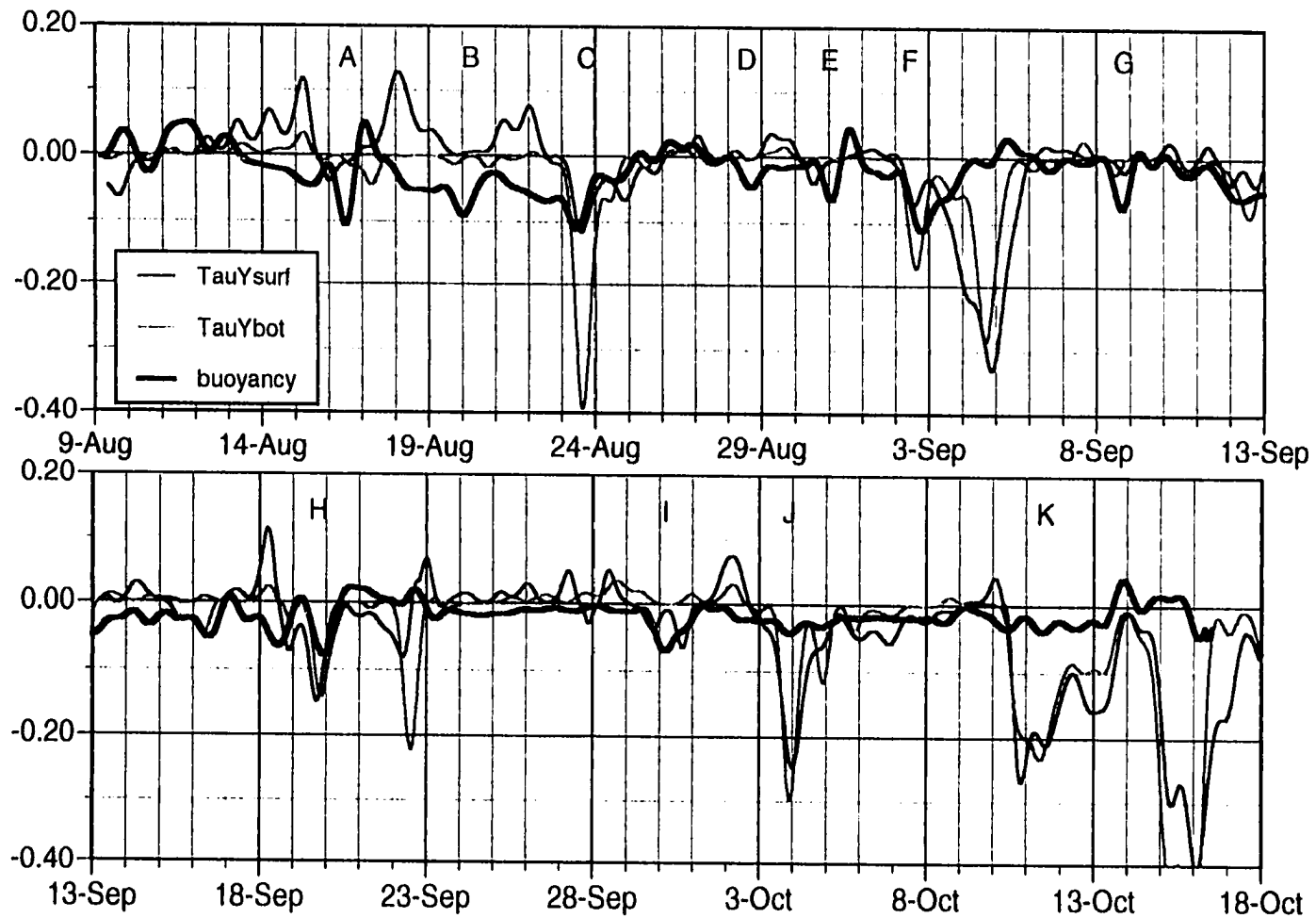


Figure 3.14. Estimates of surface stress, bottom stress and buoyancy term in alongshore momentum balance.

Figure 3.15. Map of ADCP surface velocities and 30 psu isohaline from shipboard underway surface mapping system, October 22, 1994.

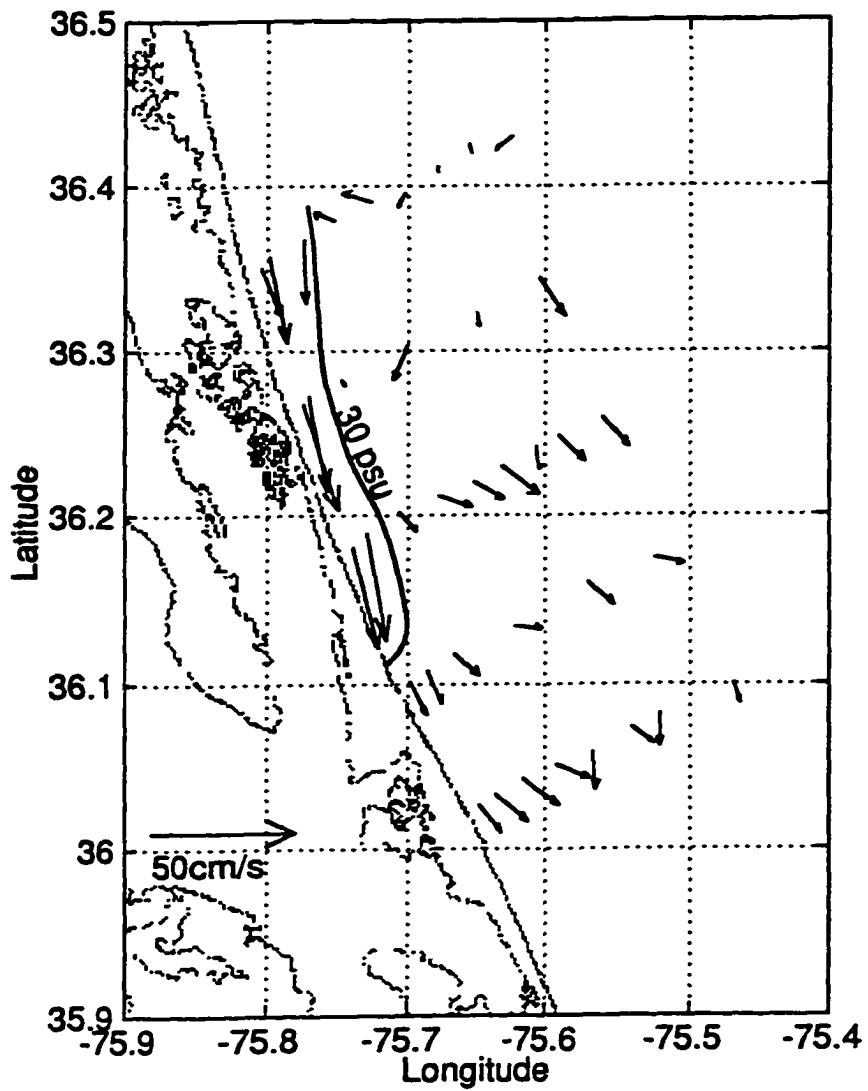


Figure 3.15. Map of ADCP surface velocities, and 30 psu isohaline from shipboard underway surface mapping system.

Figure 3.16. Upper panel: surface salinity cross-shore profiles from Transect 35 (dotted) and Transect 30 (solid). Middle panel: Along-shore component of ADCP velocity (greyscale contours) overlaid with salinity contours from Transect 35. Lower panel: same as middle panel for Transect 30.

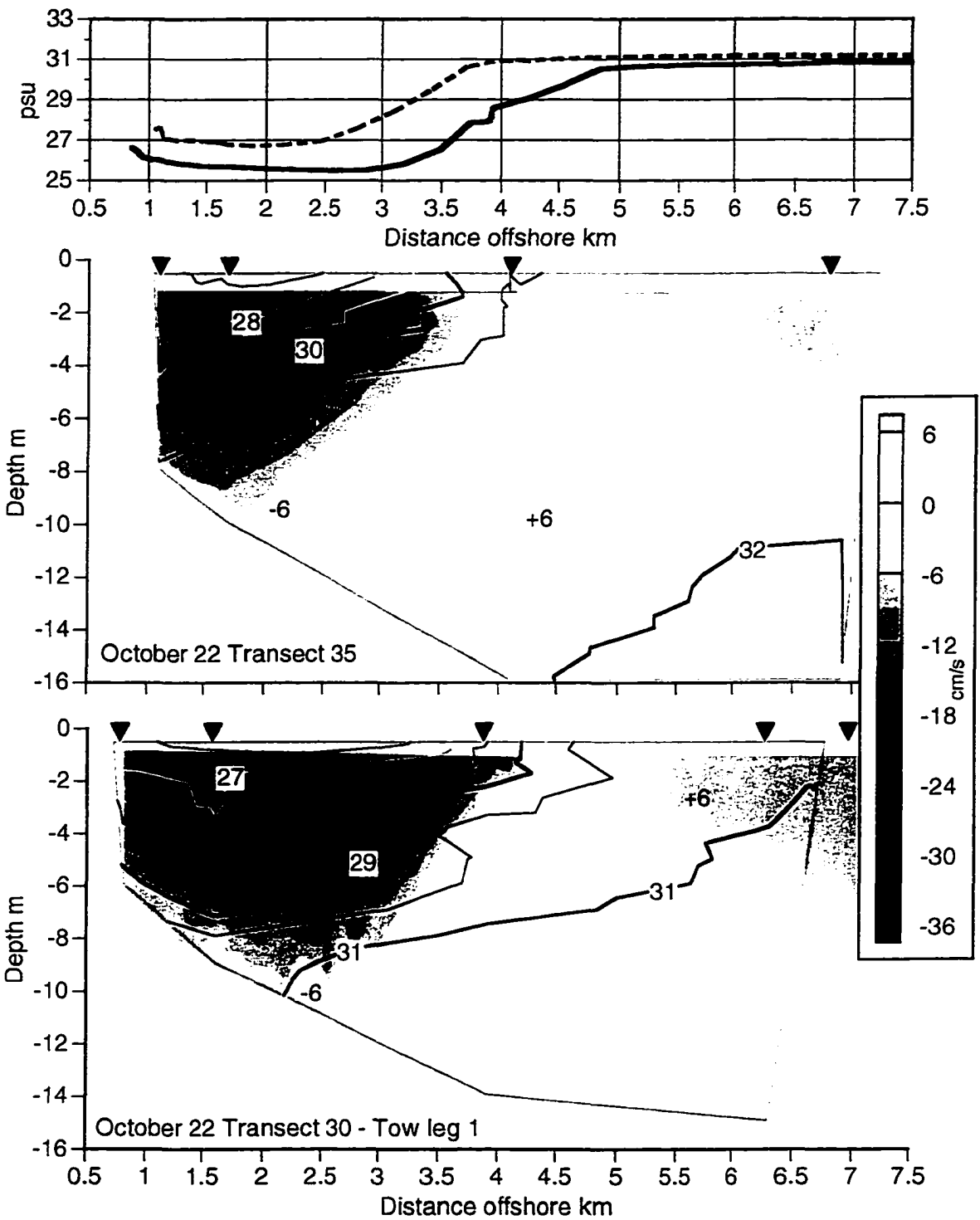


Figure 3.16. Upper: surface salinity cross-shore profiles from Transect 35 (dotted) and Transect 30 (solid). Middle: Alongshore component of ADCP velocity (greyscale contours) overlain with salinity contours from Transect 35. Lower: Transect 30.

Chapter 4 Plume Source

An investigation is made into the possible sources of the 2 to 8 day variability observed in the plume along the coast of North Carolina as described in the previous chapter. Inflow to the Chesapeake Bay from its tributaries fluctuates little on the time scale of a few days. However, volume flux across the Bay entrance (derived from waterlevel variations within the Bay) is strongly energetic in the meteorological synoptic or 'weather' band between 3 to 6 days. Peak periods of outflow are shown to precede most plume events by a lag of 1 to 2 days. Additional variation in the Bay volume is seen at periods of 2-3 days which corresponds to the natural seiche frequency of the Bay. Data from a 1982 NOAA current meter deployed at the mouth of the Bay is used to verify the method of computing volume flux.

Volume flux through the Bay mouth is driven by both the alongshelf and cross shelf components of the wind, but via different mechanisms depending on the time scale. At periods greater than 3 to 4 days, changes in coastal sea level driven by Ekman transport on the shelf control the volume flux across the Bay mouth, so that downwelling winds force a shoreward flux of water which results in the filling of the estuary; while upwelling-favorable winds cause a depression of coastal sea level and a decrease in estuary water volume. At higher frequencies the surface flow is frictionally driven in the local wind direction. An analytical barotropic model is used to examine the time scales and basin geometries over which these different responses can interact.

4.1 Introduction

The intermittent presence of the Chesapeake Bay plume along the North Carolina coast invites questions about the variations in the processes that control this low salinity water upstream of our study region. The moored salinity data indicate that a new plume intrusion arrived roughly every 2 to 8 days. Is the outflow from the Chesapeake Bay itself pulsed on a similar time scale and if so, what causes this? Alternatively, is a continuous estuarine outflow being at times diverted away from its downstream course? The Chesapeake plume has seldom been observed on the shelf north of the mouth, so an upstream path is unlikely. However, modeling studies (Chao, 1987, Kourafalou et al., 1996) indicate that upwelling winds could drive offshore flow of the plume waters. It is possible that strong mixing conditions could disperse the low salinity signal before it is seen in the down-coast CoOP study area. Another possible scenario involves the temporary accumulation of the outflow in the inertial turning or 'bulge' region outside of the Bay mouth, which was suggested by Oey and Mellor (1993) to trigger intermittent meanders along the outer edge of the plume. The CoOP '94 field program took very few measurements in the region near the Bay, so these latter scenarios cannot be examined.

Unfortunately, there were also no direct measurements of freshwater flux or currents at the Bay mouth during the 1994 field program. Surface salinities were profiled through the mouth at intervals no more frequent than every two weeks when the ship entered or left port. Therefore, to attempt to answer these questions, additional sources

of data were acquired. Daily values for freshwater inflow to the Bay were obtained from USGS offices in Maryland and Virginia. Hourly waterlevels in the estuary, from which the volume of water in the Bay was estimated, were available from NOS data centers. The winds recorded at the Chesapeake Light Tower, just outside of the mouth of the Bay, were used to represent coastal wind conditions. To further explore the proposed relationships between winds and Bay/shelf exchange, data were obtained from a year-long monitoring study done by NOAA in 1982 that included direct current and salinity measurements in the Bay mouth.

4.2 Freshwater Inflow to the Chesapeake Bay

Stream inflow to the Chesapeake region is monitored by the USGS on 3 major tributaries: the Susquehanna, which supplies 50% of the freshwater; the Potomac; and the James. The daily values are routinely adjusted by USGS for diversions of freshwater for municipal uses and the total inflow was computed by the method of Bue (1968) which accounts for the ungauged portions of the watershed. The inflow remained close to its seasonal mean of 1350 m³/s for most of July through October, 1994 (Figure 4.1). There were three noticeable inflow events, the largest of which occurred in mid-August, when the flow peaked at over 8000 m³/s. This resulted in the 1994 August monthly average of 2376 m³/s, which is almost three times the climatological mean for August of 850 m³/s (USGS, 1994). Flows in September and October were 900 and 1100 m³/s, which are average for that season. There was no significant variation in inflow occurring on the time scale of 2 to 8 days.

The Chesapeake Bay is a very large estuary, with a length of 290 km and an average width of 22.5 km. The average depth of the Bay proper is 8.4 m, giving it a volume at mean low water of approximately 50 km³ (Cronin, 1971). For a reservoir of this size, the depth change due to one day's average inflow of 1350 m³/s would be less than 2 cm, contrasted to a tidal range in the Bay proper of 30 to 80 cm (Fisher, 1986). Thus several days inflow could be stored before release without noticeable change in surface elevation.

4.3 Meteorological Control of Bay/Shelf Exchange

A number of studies have determined that atmospheric forcing exerts a strong control on the exchange of water between an estuary and the adjacent coastal ocean (Wang, 1979, Wong and Garvine, 1984). The most energetic and effective forcing occurs on the meteorological mesoscale, or synoptic, time scale between 3 and 7 days, which matches well with our plume event timing. Many studies of subtidal exchange rely on sea level variation within the estuary to infer volume flux, based on the continuity requirement. Measuring outflow directly is challenging largely because the tidal currents are an order of magnitude larger than the residual flows in which we are interested. There can also be strong vertical and lateral variations (Valle-Levinson and Lwiza, 1995) which would require a large number of instruments to sample adequately the outflow.

4.3.1 Meteorological Control of Bay/Shelf Exchange: Observations

Measurements of waterlevel, η , for the summer and fall of 1994 were obtained from NOAA for three gauges located within the Chesapeake Bay (Figure 4.2) : Baltimore (BALT), Lewisetta (LWST) and the Chesapeake Bay Bridge Tunnel (CBBT) and used to estimate the volume of water within the Bay. Tidal and higher frequency variations were removed from the hourly time series with a low-pass filter (see section 2.3). The transport of water through the mouth of the Bay was computed as

$$\text{transport} = -\text{inflow} + \frac{d\text{Vol}}{dt} \quad (\text{eq. 4.1})$$

where inflow is the total runoff from the tributaries. Outflow is negatively-directed transport. In a manner similar to that used by Goodrich (1988), the subtidal volume flux was computed from

$$\frac{d\text{Vol}}{dt} = A_{\text{BALT}} \frac{d\eta_{\text{BALT}}}{dt} + A_{\text{LWST}} \frac{d\eta_{\text{LWST}}}{dt} + A_{\text{CBBT}} \frac{d\eta_{\text{CBBT}}}{dt} \quad (\text{eq. 4.2})$$

where dt is 1 hour. A_{gauge} is the Bay area that each gauge is assigned to represent (Table 4.1), as illustrated by the shaded regions shown in Figure 4.2. Again, falling sea level implies negative volume flux (outflow).

Gauge	Length(km)	Width (km)	Area (km²)
BALT	131.5	10	1315
LWST	111.1	33	3667
CBBT	46.3	33	1528
Total	289	mean=22.5	6509

Table 4.1.

Size of Chesapeake Bay surface area assigned to each waterlevel gauge in order to calculate volume flux.

The resulting volume flux ($\frac{dVol}{dt}$) time series is plotted in panel a of Figures 4.3 I-III for August, September and October of 1994. The power spectrum of this time series (Figure 4.4) indicates that the most energetic fluctuations in volume flux occur on time scales of 2 to 6 days, peaking at 2.5 to 3 days. The volume flux, which does not include the river inflow, has a mean near zero ($< 0.07 \times 10^3 \text{ m}^3/\text{s}$) with an rms amplitude of $8.5 \times 10^3 \text{ m}^3/\text{s}$. This is four times the rms amplitude of the river runoff. The spectrum of the river runoff, overlaid on Figure 4.4, shows no high-frequency energy. Therefore the flow through the mouth on the dominant time scale of the volume flux (2 to 6 days) should be controlled by barotropic fluctuations, rather than freshwater flow.

Volume of water in the Bay is calculated by integrating the volume flux (exclusive of inflow) over time (Figure 4.3 I-III, panel c), arbitrarily setting the initial value to zero. The volume showed a small increasing trend during the study period of about 1%, or an overall rise of 8 cm in the Bay surface elevation. A similar volume increase was observed by Elliott and Wang (1978) who attributed it to the steric effect of seasonal warming of the coastal ocean. The average water temperature on the inner shelf off North Carolina increases from July through September, falling in October (Austin and Lentz, 1998). However, a rising overall trend in coastal sea level during this time period could also be explained by the seasonal difference in average wind stress, with summer upwelling winds changing to predominantly downwelling winds in the fall (see section 3.3).

During the study period, volume flux amplitudes of over $15 \times 10^3 \text{ m}^3/\text{s}$ occurred at least weekly. The resulting total volume change for these larger flows (over an average period of 4 days) was 1.6 km^3 ,

approximately equal to the tidal prism. The largest observed volume flux occurred during the waning phases of the northeaster of mid-October, with a transport of over $25 \times 10^3 \text{ m}^3/\text{s}$. Preceding that outflow, the rise in volume resulting from this entire storm was close to 3 km^3 , which is about 6% of the total volume of the Bay. Storm-driven volume exchanges of up to 10% of the total Bay volume have been reported by Boicourt (1973) and Goodrich (1988).

Note that some level of baroclinic exchange driven by the gravitational circulation pattern at the mouth of the estuary can be occurring at all times, and not be reflected in this barotropic calculation of volume flux. It would be preferable to be able to identify freshwater flux, which occurs preferentially towards the surface and the southern side of the Bay mouth (Valle-Levinson et al., 1994). The purpose here is to identify moments of large barotropic outflow events from the Bay; assume that this estuarine water will be significantly fresher than the shelf water; and determine if these events correlate with plumes observed far to the south.

The time series of salinity recorded at the J1 sensor (or the FRF pier for the time period before 7 August) is repeated in the panel **b** of Figures 4.3 I-III with the plume events labeled as in chapter 3. Nearly all sharp decreases in salinity, which indicate the arrival of an intrusion, follow a peak in $\frac{dVol}{dt}$ of at least $-7 \times 10^3 \text{ m}^3/\text{s}$. These moments of strong outflow are marked in Figures 4.3 I-III with arrows. With the exception of the outflow prior to event "J", all the peaks in $\frac{dVol}{dt}$ which precede plume events have a magnitude larger than $7 \times 10^3 \text{ m}^3/\text{s}$, and average over $14 \times 10^3 \text{ m}^3/\text{s}$. Outflows of this size occurred approximately every 3 to 4 days. The time interval between the drop in the salinity signal at J1 and the preceding

large peak in outflow from $\frac{dVol}{dt}$ averaged 1.1 days, or 27 (+/- 8) hours, comparable to the lag anticipated from the observed along-coast propagation speeds of the intrusions (see section 3.4). This relationship was clearest for the August events, and became more complicated in the fall.

In Table 4.2 the time of each peak outflow that precedes a plume event is given, and the lag in hours is determined. From this the average intrusion speed from the Bay to the northern part of the study region can be computed (column 5).

Event (date of arrival at FRF)	Peak of $\frac{dVol}{dt}$ (decimal day)	Peak of $\frac{dVol}{dt}$ (decimal day)	Arrival @ J1 (decimal day)	Hours to J1	Intrusion Speed (cm/s)	Ambient Shelf current (cm/s)
P 8/07	218.05	218.05	218.71	16	-117	
A 8/16	227.34	227.34	228.33	24	-79	4.7
B 8/20	230.83	230.83	231.84	24	-78	-8.0
C 8/23	234.58	234.58	235.38	19	-98	-15.9
D 8/28	238.96	238.96	240.41	35	-54	1.7
E 8/31	241.88	241.88	243.00	27	-69	7.6
F 9/02	244.67	244.67	245.54	21	-89	-8.5
G 9/09	250.54	250.54	251.63	26	-72	3.6
H 9/19	261.46	261.46	262.46	24	-78	-6.2
I 9/30	271.38	271.38	272.91	37	-51	12.5
J 10/04	275.08	275.08	276.66	38	-49	-4.1
K 10/11	283.38	283.38	284.12	18	-105	-31.6
L 10/18	289.88	289.88	290.96	26	-72	-27.5
M 10/22	292.88	292.88	294.66	43	-44	8.1
N 10/26	297.13	297.13	298.50	33	-57	1.1
			average =	27	-74	-4.9

Table 4.2.

Times in decimal Julian days of peak in volume flux and arrivals of low salinity intrusion at the northern-most sensors along the 5-m isobath in the CoOP study region.

The salinity decrease on 13 September, which was attributed previously to an onshore movement of fresher water, rather than an intrusion moving along-coast, was not preceded by a strong outflow peak. On the other hand, several cases of strong outflows, such as those observed on 29 July, 25 August, and 23 September, did not result in any expression in the downstream salinity signal. These counter-examples will be discussed in section 4.3.7.

In Figure 4.5 this data is used to extend the comparison of frontal position versus time which was previously shown in section 3.4 (Figure 3.9). In this case the observed speeds over ground, C_{obs} , are considered, rather than the speeds adjusted for ambient shelf flow, C_{adj} (as were used in Figure 3.9), which reduces the scatter. The average C_{obs} between sensors J1 and the FRF pier for all plume events was 55 cm/s. A linear extrapolation of this intrusion speed back in time is a good predictor of a peak in outflow, although the best prediction speed (average observed intrusion speed between peak in $\frac{dVol}{dt}$ and arrival at J1) is higher (average of 74 cm/s), as expected from the results in section 3.4 that show the intrusion slowing as it moves farther from its source.

In comparison to these intrusion speeds, the ambient shelf water moved substantially more slowly. The ambient flow is represented in the right-most column in Table 4.2 by the along-shore current measured at the 20-m mooring @ 6m depth, averaged over the time interval from column 2 to 3. Considered over all plume events, the shelf water moved southwards at less than 5 cm/s, and indeed for some events, flowed to the north. Such low ambient speeds would seem to preclude the possibility that the observed low salinity outflow could have been carried southwards

by the general shelf circulation, but must be traveling as a baroclinic current as proposed in the previous chapter.

As noted in section 3.6, the general inner shelf circulation is primarily wind-driven. The currents' response to the wind in these depths is fully established within 6 to 7 hours, as seen in the lag of the maximum correlation between along-shore wind stress and along-shore flow at the 13-m mooring (Figure 4.6). However, the lag of the maximum correlation between wind stress and salinity occurs at 31 hours (see Figure 4.6), a time scale more compatible with that previously determined for an the intrusion propagating down from the Bay mouth at linear internal wave speeds. This suggests that the salinity signal is probably more related to the baroclinic plume events, rather than advection.

The time scale of the observed volume fluctuations (2 to 6 days) falls largely within the synoptic band, indicating that meteorological variations could be the forcing mechanism, although additional energy is being supplied in the higher ($T < 3$ days) frequencies. The power spectra of the coastal wind stress components (overlaid on Figure 4.4) indicate that over 80% of the wind stress variance is contained in periods longer than 4 days. The synoptic weather patterns over the Middle Atlantic Bight during the summer and fall of 1994 have been characterized by Austin and Lentz (1998) as dominated by the passage of atmospheric low pressure centers to north of the region. These low pressure systems occurred every 6 to 7 days, and propagated in an east-northeast direction, so that the trailing cold front passed over the study site. This caused a rapid change in wind direction from predominately north-northeastward to southwestward behind the front. This pattern is consistent with the conclusions of Mooers et al. (1976), who described the regional

meteorology as a succession of extra-tropical cyclones on about a 5 day interval.

In the observations, the energy in the north-south component of the wind stress was larger than in the east-west (Figure 4.4) as expected from the patterns described above. An examination of the wind vectors during the study period (Figures 4.3 I-III, panel d) shows that periods of downwelling winds (south or southwestward) are associated with increasing volume within the Bay (panel c); while peaks in outflow ($-\frac{dVol}{dt}$) can be seen to occur at times of decreasing along-shore wind stress (where positive stress is directed northward). The time rate of change of the north-south component of the wind ($dWindV/dt$) is overlaid on the volume flux plot in Figure 4.3 I-III panel a, where the strong correspondence between the two time series, particularly for large negative peaks, is evident. These moments of rapid decrease in along-shore wind stress can be due to a complete reversal of wind direction, as the frontal passage seen on 6 August; or to a transitory let-up during northward winds (e.g. 29 August). The Bay outflow responds very quickly to the diminution of northward wind stress, with peak outflow lagging $dWindV/dt$ by 3 hours. The time relationship between along-shore wind stress and salinity at the mooring off Duck noted above (Figure 4.6) can now be seen as indicative of the same process as that producing the observed lag between $\frac{dVol}{dt}$ and downstream salinity (Table 4.2), i.e., the release of estuarine water which propagates down the coast as a buoyancy current.

4.3.2 Meteorological Control of Bay/Shelf Exchange: Background

The downstream arrival of low salinity water is likely related to meteorologically-forced events of barotropic outflow from the Chesapeake Bay. But how exactly does the wind control the exchange between an estuary and the adjacent coastal ocean? The waterlevel inside the estuary can be forced remotely by variations in the coastal sea level, which is driven by Ekman transport due to the along-coast component of the wind. Through this mechanism, fluctuations in estuary/shelf exchange are 180° out of phase with the wind: upwelling winds (positive wind stress) would cause an emptying of the estuary (negative volume flux), while downwelling conditions (negative wind stress) fill it up (positive volume flux). Alternatively, winds blowing directly into and up the estuary could cause it to fill through frictionally-driven currents. Given the geometry of the Chesapeake Bay basin, which, except for the lower 30 km, is nearly aligned with the coastline north of the mouth, remotely-forced flow will be in the opposite direction of locally wind-driven flow (Figure 4.7).

Previous work by Elliott and Wang (1978) and Wang (1979), suggest that these different mechanisms dominate within the Chesapeake Bay at different time scales. Their results showed that at low subtidal frequencies (periods of 6 or more days) the remote forcing dominated, so that coastal sealevel controlled the direction of the exchange across the mouth. For shorter time scales ($T < 4$ days) the Chesapeake Bay was seen to respond directly to surface stress in the local wind direction.

A barotropic analytic model was developed by Garvine (1985) to examine the coupled system of a 1-D estuary and 2-D coastal ocean under varying geometry and forcing frequencies. The angle of the estuary to the

coastline can be varied in the model, which allows the local forcing to either enhance or oppose the remote (coastal) forcing. Evidence for opposing effects was observed in Delaware Bay, which is the similarly aligned to the Chesapeake, (Wong and Garvine, 1984) where energetic subtidal currents were observed flowing against the local wind. The key parameter that emerges from Garvine's analysis is a comparison of the time that it takes a barotropic signal to propagate through the system ($\frac{L}{\sqrt{g h}}$, where L is the estuary length) versus the time scale of the atmospheric forcing, $\frac{2\pi}{\omega}$, where ω is the frequency of the wind variation. The barotropic response time of most estuaries is less than half a day, much shorter than the synoptic wind scale. Garvine's solutions show that the local wind effect on the surface elevation and, thereby on the barotropic current variations, is smaller than the remote effect by $O(\frac{\omega L}{2\pi\sqrt{g h}})$. Therefore, for low subtidal frequencies, the barotropic waterlevel fluctuations in most estuaries will be dominated by the remote shelf response.

This conclusion was verified in the Chesapeake Bay by Valle-Levinson (1995) using data from moorings deployed during the summer of 1993. Surface-to-bottom inflow was measured following strong upwelling periods, as the depressed waterlevel in the lower Bay rebounded. Barotropic outflow occurred during the waning phases of several downwelling events, which had caused elevated waterlevels in the lower Bay. No evidence for flow in the direction of the wind was discerned, and given the rapid response observed for the lower Bay waterlevel to along-coast wind forcing, Valle-Levinson suggests that the remote effect is dominant at all subtidal time scales. This contrasts to the study of year-long records of wind and waterlevels by Wang (1979), whose analysis separated out the contributions of the wind components and

coastal sea level in different frequency bands for different seasons. Wang's analysis concluded that the local wind effect in the Chesapeake Bay should be even more prevalent than the remote during the summer for time scales between 3 and 7 days. Wang emphasized the direct frictional driving role of the lateral (east-wind) wind which was coherent with Bay waterlevels at all frequencies.

Wang also pointed out the peak in volume flux energy at about 2.5 days (which is present in the 1994 data, see Figure 4.4), and identified it with the first mode of the $\frac{1}{4}$ -wave seiche present in the Bay. With the node at the mouth, and anti-node at the head of the 290 km-long basin, the natural period of oscillation would be (Pond and Pickard, 1983, p.271). The effective long wave phase speed C_0 has been determined, by observing the phase propagation of the M2 tide within the basin, to be approximately 6.2 m/s (Elliot and Wang, 1978), which is about 70% of the inviscid phase speed $C = \sqrt{gh}$. This yields a period of about $T=52$ hours or 2.2 days.

A study presented by Chuang and Boicourt (1989) analyzes two events of oscillatory barotropic outflow that were measured at the mouth of the Chesapeake Bay in the spring of 1986. The first event appeared to be straightforward: locally forced seiche motion correlated with fluctuations in the north-south wind at a similar 2-day period. The second set of even larger oscillations had a somewhat higher frequency and were correlated only with the latitudinal wind component. This suggested a more complicated model where the lower reaches of the Bay, being oriented at 45° from the north-south coastline, is frictionally forced by the east-west wind, which can then excite a free seiche in the upper (north-south oriented) portion of the basin. When the east-west forcing is in resonance with the natural frequency of the upper portion, strong oscillatory flows

can occur. If the longitudinal wind turns southward during the falling half of a seiche oscillation, the combined effect produces a large surge of outflow.

4.3.3 Meteorological Control of Bay/Shelf Exchange: Spectral Analysis

The literature in summary presents a complex and occasionally contradictory picture of the relationship between Bay/shelf exchange and the wind. It is an interaction that varies with the time scale of the forcing and possibly with the season. For the CoOP study period from August through October of 1994, the coherence and phase from the cross spectra between the wind stress components and volume flux are presented in Figure 4.8. The volume flux is coherent with the east-west component of the wind for all frequencies (Figure 4.8, panel b), whereas it is more coherent with the north-south component (panel a) for shorter periods ($T < 3.5$ days). Note that the two wind components are themselves coherent (not shown), especially for long periods ($T > 7$ days). For the low frequencies, the north-south wind leads the volume flux by 200 to 210° , meaning that northward (positive) wind stress produces outflow (negative volume flux) after a 25° lag (about 12 hours at a period of 7 days). This is the relationship expected for a remotely forced response, where upwelling- or downwelling-favorable winds cause a sea level change at the mouth which then propagates up the Bay. In contrast, the north-south wind is approximately in quadrature with the volume flux within the "seiche" band ($3 > T > 2$ days). This matches the proposed locally forced seiche scenario where wind would be in phase with the surface slope, and lead

the current by 90° . This relationship was noted in section 4.3.1 in the time series of Figures 4.3 I-IIIa, where the time rate of change of the along-shore wind ($d\text{Wind}V/dt$) is seen to predict the volume flux ($\frac{d\text{Vol}}{dt}$) very well for much of the study period. Almost all peaks in outflow (negative volume flux) are aligned with a similar peak in decreasing wind stress during August and September, whereas in October, the time series are more frequently misaligned. At low frequencies, the cross-shore wind and the volume flux were also out of phase (Figure 4.8, panel b): offshore (positive) wind stress forces outflow. This is most likely a local, frictionally-driven response, as the cross-shore wind is ineffective at causing coastal setup or setdown.

To explore these relationships further, there is available data from a long-term mooring that was maintained by NOAA at the Bay mouth from 1981 into 1983. This mooring 'Stn40' was sited directly between the Capes (see Figure 4.2) on the north flank of the main deep channel through which much of the volume exchange should flow. Current meters and CTDs were mounted at 4.6 m below the surface and 1.6 m above the bottom in 13 m of water. The component of the current that lies along the principal axis of the flow (upper meter = 128° , lower meter = 132°) was extracted (outflow being negative). Goodrich (1988) analyzed this data set in his study of meteorologically induced flushing of the estuary, and established the direct response of the salinity at the mouth to subtidal volume in the Bay. He did not, however, attempt to specify the mechanisms or time scales of the response.

A section of the sub-tidal currents from this mooring data taken during the summer of 1982 is shown in Figure 4.9. This site displays a net outflow (negative in this orientation) with a subdued baroclinic nature --

the bottom current being more directed into the Bay. On top of that baroclinic pattern is superimposed large fluctuations producing times when both surface and bottom currents are strongly in the same direction, illustrating how the gravitational circulation is modulated by the meteorologically-forced barotropic variations. A look at the original hourly currents showed that during these periods of very strong outflow, even the flooding tide was outward directed. Estimates of volume flux were computed for 1982 in the same manner as described in section 4.3.1, using the same waterlevel gauge locations as for 1994. Then the implied average exchange current was computed simply by dividing the volume flux by the cross-sectional area of the Bay mouth (estimated to be $1.85 \cdot 10^5 \text{ m}^2$ by Boicourt (1973)). The patterns in this estimate of current (Figure 4.9) match remarkably well with the measured flows, especially during times of large outflow, confirming that the simple volume flux estimates can be a reasonable proxy for actual total exchange through the main channel of the mouth.

In Figure 4.10, the spectrum of volume flux ($\frac{dVol}{dt}$) computed for the late summer/early fall for 1982, is compared to that of the measured currents and salinity from that time. The very high coherence between volume flux and measured current (panel b) again supports the method used to compute $\frac{dVol}{dt}$ (eq. 4.2). The current and salinity at the mouth are coherent for all but the lowest frequencies (panel c), and current leads with a phase difference near 90° , as would be expected for variations that are due to advection of a longitudinal salinity gradient. Both the surface (solid line, panel b) and bottom (dashed line) currents respond together with $\frac{dVol}{dt}$ for periods shorter than $T < 5$ days. This would imply that the flow through the main channel of the mouth appears locally barotropic,

with outflow occurring from the surface to the bottom of the water column. At lower frequencies, the bottom current is less coherent with the top and with $\frac{dVol}{dt}$; and becomes less in phase with the top current, as the response on longer time scales displays a more baroclinic nature, recovering the gravitational circulation pattern classically associated with partially-mixed estuaries.

The energy (Figure 4.10, panel a) for both current and volume flux suggests a separation into two peaks: one at $T=4$ days (the 'cyclone' band) and one centered at $T=2.5$ (the 'seiche' band), a separation that was less noticeable in the 1994 spectra for the same season (Figure 4.4). This is most likely due to enhanced energy for those frequencies in the wind components for 1982 (Figure 4.11, panel a). The phase difference described above for the 1994 data shows up more clearly here: there is a change from an inverse relationship for the low frequencies, to one nearly in quadrature for higher subtidal frequencies. The change occurs abruptly at a period of 3 days (Figure 4.11, panels b & c).

The spectra of the individual waterlevel gauges (Figure 4.12) at the head (BALT) and mouth (CBBT) of the Bay help us understand how the volume flux behaves so differently in the two frequency bands. Variations in CBBT are seen to be much stronger at low frequencies, which confirms Wang's (1979) finding that the sea level at the mouth is relatively unresponsive to high frequency forcing. The amplitude of these low frequency fluctuations, which are driven by changes in coastal sea level, diminishes as they propagate up the Bay, so that the variation in BALT is damped at low frequencies. On the other hand, the amplitude of higher frequency fluctuations are much larger at BALT than at CBBT,

demonstrating the effectiveness of wind at these shorter time scales to drive setup towards the head of the Bay.

For higher frequencies, then, as CBBT fluctuates little, $\frac{dVol}{dt}$ is controlled largely by the variation of waterlevel at the head of the Bay. This behavior allowed Boicourt, in Berger et al..(1995), to use a simple height difference between BALT and CBBT (or surface slope) as a proxy for volume in the Bay. They found a relationship between the time rate of change of the Bay's surface slope (which they termed a "surge index") and currents measured on the inner shelf of the North Carolina coast, which they interpret as evidence of significant buoyancy forcing. In a similar finding for the 1994 observations, the outflow index used here ($\frac{dVol}{dt}$) is significantly coherent with the salinity signal recorded at the North Carolina study site J1 (Figure 4.13) for periods between 2.2 to 3 days. Over this frequency range, the phase between the two signals exhibits a positive linear slope indicative of a 15 hour lag of the J1 salinity to the outflow index.

4.3.4 Barotropic Linear Model of Estuary/Ocean Interaction

With two mechanisms proposed as dominant at different time scales, there must be interaction occurring at intermediate frequencies. An exploration of this interaction is made here through the use of the analytic model developed by Garvine (1985) and discussed in section 4.3.2. This model incorporated a variable θ_c that describes the angle between the estuary main axis x and the coastline, which allows the interaction between the remote and local mechanisms to vary (Figure 4.14). When θ_c

is close to 90° , they are nearly independent. For estuaries whose axis is nearly aligned with the coastline, both effects will be proportional to the along-shore wind. The remote and local effects will combine for a small angle, and oppose each other at angles close to 180° . The Chesapeake Bay geometry is an example of the latter case. The interaction of these effects creates complex varying behavior in spite of the underlying simplicity of the 1-layer linearized physics of the model. Garvine focused on the behavior of the solutions for wind forcing with a period of 7 days within a basin of 100 km length, and concluded that the remotely forced motions dominated. Here parameters representative of the Chesapeake Bay geometry and meteorology will be used to examine how the behavior varies with the frequency of the wind forcing ω and with θ_c .

The governing equations of the model assume a linear and barotropic system for the subtidal current u and subtidal sea level η :

$$\frac{\partial u}{\partial t} = -g \frac{\partial \eta}{\partial x} + \frac{\tau_w^x - \tau_b^x}{\rho h} \quad \text{and} \quad \frac{\partial u}{\partial x} = \frac{1}{h} \frac{\partial \eta}{\partial t} \quad (\text{eq. 4.3 a,b})$$

where the bottom stress τ_b^x is represented by $\tau_b^x = \rho r u$. The linear bottom friction parameter r is set to 0.0003 m/s, a value similar to that used by Garvine, which results in an elevation response at the head of the basin consistent with the level of variation observed at the BALT gauge. The surface wind stress is imposed as $\tau_w^x = \tau \cos \theta e^{i\omega t}$ with the wind blowing at an angle θ from the estuary axis and varying over frequency ω . In this section note that the x axis is along-estuary (see Figure 4.14).

The remote effect of coastal sea level is imposed by the boundary condition at the mouth ($x=0$) by

$$\eta(0,t) = \frac{\alpha \tau}{f} \cos(\theta - \theta_c) e^{i\omega t} \quad (\text{eq. 4.4})$$

where α is an empirical parameter that gives the sensitivity of coastal sea level to the along-shore component of the wind. Garvine uses a value of $\alpha = 5 \times 10^{-4} \text{ m}^2\text{s/Kg}$, citing a sea level response of 0.5 m to a wind forcing of 0.1 Pa (Wong and Garvine, 1984). Sea level data from the CoOP study period from both the mouth of the Bay (CBBT in Figure 4.12) or from the coastal gauge at the FRF indicate a much less responsive system, with 0.1 Pa causing only a 0.1 m rise or fall. Theoretically, the elevation at the coast should grow linearly in time as $\eta(t) = \frac{\tau t}{\rho \sqrt{gh}}$ (Csanady, 1982, p.44) until a balance is reached between the along-shore current and bottom friction. Given a frictional time scale of 10 hours (Beardsley and Boicourt, 1981), and an average shelf depth of 30 m, the resulting sea level change for a 0.1 Pa wind would be about 0.2 m, a 2:1 transfer relationship, being equivalent to $\frac{\alpha}{f} = \frac{2}{.1}$ or $\alpha = 1.8 \times 10^{-4} \text{ m}^2\text{s/Kg}$ for local value of $f = 9 \times 10^{-5} \text{ s}^{-1}$. This will be the value for α used below.

The other boundary condition is that of no flow at the head of the estuary ($x = L$). The non-dimensionalized equations were then solved by Garvine, yielding solutions that can be separated into the remote and local contributions. These are, when restored to dimensional units, the real parts of:

$$\eta_{\text{rem}}(x,t) = \frac{\eta(0,t) K \cosh(K \frac{\omega}{c}(L-x))}{K \cosh(K \frac{\omega}{c}L)} e^{i\omega t} \quad (\text{eq. 4.5a})$$

$$\eta_{\text{loc}}(x,t) = \frac{W \cos(\theta) \sinh(K \frac{\omega}{c}x)}{K \cosh(K \frac{\omega}{c}L)} e^{i\omega t} \quad (\text{eq. 4.5b})$$

$$u_{Rem}(x,t) = \frac{c i \eta(0,t) K \sinh(K \frac{\omega}{c}(L-x))}{h K^2 \cosh(K \frac{\omega}{c}L)} e^{i\omega t} \quad (\text{eq. 4.5c})$$

$$u_{loc}(x,t) = \frac{c i W \cos(\theta) (\cosh(K \frac{\omega}{c}L) - \cosh(K \frac{\omega}{c}x))}{h K^2 \cosh(K \frac{\omega}{c}L)} e^{i\omega t} \quad (\text{eq. 4.5d})$$

where L is the estuary length; $c = \sqrt{gh}$; $W = \frac{\tau}{\rho \omega c}$; and K contains the bottom stress parameterization as $K = \sqrt{-1 + i \frac{\Gamma}{h \omega}}$.

In Figure 4.15, the elevations and currents due to the remote and local effects of an along-shore harmonic wind stress of amplitude 0.1 Pa with a period of $T = 7$ days on an estuary whose main axis is oriented at 160° from the coastline are shown for two different estuary lengths. Case A (the top panels of each set) has a length of 100 km, the dimension used by Garvine (1985). Case B (the bottom panels) has a basin length of 290 km, closer to the true length of the Chesapeake Bay. The ratio between the local and remote effects changes from approximately $\frac{u_{loc}}{u_{Rem}} = 0.25$ for the shorter estuary, to $\frac{u_{loc}}{u_{Rem}} = 0.73$ for the longer. The change is due not so much to the equivalent change in the ratio of the time scales, as proposed in section 4.2.2, but that the longer basin allows a larger local setup η_{loc} to develop. Theoretical wind driven setup in a narrow basin, ignoring bottom friction, should be

$$\eta_{loc}(x) = \frac{\tau}{\rho g h} x. \quad (\text{eq. 4.6})$$

Therefore setup at the head for case B would be 2.9 times larger than case A. The remote coastal sea level effect (shown in blue in the upper panels of Figure 4.15) is the same for both basins; and, for such long time scale forcing, there is little phase or amplitude difference between the head and the mouth. Since the setdown due to the coastal sea level does not vary

much over the length of either estuary, the surface slope is due almost entirely to the local wind setup (shown in green). Flow (u) driven by continuity considerations alone will be dominated by the larger temporal changes of $\int_0^L \eta_{loc} dx$ and $\int_0^L \eta_{rem} dx$, or, over the period T , the area bounded between the solid and dashed lines for each color. Given the basin geometry and assumptions for the value of α , these terms are of nearly the same magnitude for case B, the longer estuary. So, for the Chesapeake Bay, it appears that the opposing effects of local and remote forces tend to balance each other. If the basin was either shorter, or aligned more perpendicularly to the coastline, the remote forcing due to coastal sea level would dominate. And for an estuary sited so that the local effects combined with the remote forcing, one would expect significantly enhanced exchange across the mouth.

4.3.5 Model Behavior with Varying Parameters

The effect of varying the time scale of the forcing is examined in Figure 4.16, again using a wind stress amplitude of 0.1 Pa. The amplitude of the surface elevation (Figure 4.16a) at the head of the Bay increases as the forcing frequency approaches seiche resonance. For low frequencies the remotely-forced surface elevation at the head of the Bay is in phase with the wind (Figure 4.16b), i.e. changing in phase with the elevation at the mouth. The locally forced surface elevations at the head are, of course, out of phase with the wind (Figure 4.16b green line - note second y axis), given this alignment of the estuary axis (Figure 4.14). Since these oppositely directed responses are in near anti-phase, they balance, and the

amplitude of the total resultant current (Figure 4.16c) is low. With increasing forcing frequency, the head elevations increasingly lag behind the wind, with the remotely-forced elevation lagging further than the locally-forced (Figure 4.16b). They become increasingly unbalanced, so that the amplitude of the resulting combined flow (Figure 4.16c) grows with frequency more rapidly than required to account for the volume exchange over shorter periods, especially where the seiche-enhanced amplitudes amplify a small mismatch in phase. The ratio $\frac{U_{loc}}{U_{Rem}}$, overlaid on Figure 4.16c, shows that the contribution of the local forcing changes from about three-quarters that of the remote, to almost equal within this subtidal frequency range.

So, while the contribution from local forcing increases somewhat with higher frequencies, there is no strong shift in dominance displayed between the two mechanisms. However, here the model was run assuming that α (the parameterization of the effectiveness of an along-shore wind in causing coastal sea level changes) was invariant with frequency. Given the large dropoff in energy in the coastal sea level spectrum at shorter periods (see Figure 4.12, CBBT), one could propose α as a decreasing function of frequency. This is represented in the transfer function of the cross-spectrum of the along-shore wind stress and the coastal sea level CBBT (Figure 4.17), which decreases by about half between the 10-day and 4-day time scales. The response of waterlevel at the head of the Bay (BALT) is similar to the coastal response at long periods, at a value of approximately 2:1, confirming the original choice for α . But in contrast to CBBT, BALT is increasingly sensitive to the north-south component of the wind at higher frequencies, with its transfer function peaking in the seiche frequency range. To simulate this

behavior, the model was rerun, using an α that decreased linearly with frequency (as illustrated by the dotted line in Figure 4.17) up to a period of 3 days, after which it was held steady at a value that is one half the original α . Figure 4.16d shows the results of this experiment: the increasingly smaller remote contribution leaves the local effect unbalanced, resulting in an exchange at the mouth over twice as large (note the expanded y scale). In this case the ratio of $\frac{u_{loc}}{u_{Rem}}$ shows that the flow regime changes from being controlled by the remote effect to a regime where the locally-forced flow is twice that of the remote. The values of $u_{total}=u_{Rem}+u_{local}$, the parameter that can be compared with a measured index of exchange through the Bay mouth (either $\frac{dVol}{dt}$ or U_{top} from 1982), increases as the forcing period shortens from the longer synoptic periods towards the seiche frequency (see Figure 4.4 or 4.8). The amplitude of u_{total} ranges from 8 to 20 cm/s for periods shorter than 3 days. This matches well with the subtidal flow through the Chesapeake Bay mouth observed during the 1982 NOAA deployment, which had an rms fluctuation of 9 cm/s, with peak flows occasionally over 20 cm/s.

4.3.6 Contribution of the Cross-shore Wind Component.

Results from previous studies, together with the high coherence found between $TauX$ and volume flux in the CoOP data (Figure 4.8b), suggest that the cross-shore wind component can play an important role in promoting Bay/shelf exchange. We have seen that the along-shore wind provokes opposing (nearly balancing) motions for this model geometry (estuary axis offset 20° from the coastline). If the estuary basin is not exactly aligned with the coast, it will experience an additional local

(frictional) response due to the cross-shore component of the forcing. This cross-shore component does not contribute effectively to the remote coastal setup. Examining the model response under varying wind directions can help illustrate the possible interactions between remote and local, along-shore and cross-shore forcing. Figure 4.18a shows the resultant total current at the estuary mouth for a fixed $\alpha = 1.8e-4$. The remote effect is at a maximum for a purely along-shore wind and is zero for a purely cross-shore; the locally forced maximum is of a similar amplitude, but is offset 20° , peaking at a purely along-estuary wind and disappearing when the wind is cross-estuary. In this case, the total current resulting from a combination of these two competing effects turns out to be at a maximum (amplitude = 14 cm/s) at shorter periods when the wind is close to directly cross-shore, i.e., when the seiche-enhanced local flow is not opposed by any coastal sea level effects. These model examples illustrate the unexpected possibility of maximum exchange under the less effective cross-shore winds. And in reality, the more complicated basin geometry of the Chesapeake Bay, where the lower Bay axis is angled from that of the upper Bay, could increase the effectiveness of cross-shore winds. For the scenario where α decreases with frequency (as proposed in the last section), which emphasizes the local response, the resultant total current is larger (amplitude of 25 cm/s) and at a maximum when the wind is directed nearly along the estuary (Figure 4.18b).

The wind-forced exchange across the mouth is seen to be controlled by the particular size and orientation of the Chesapeake Bay: the angle of the Bay axis to the coastline creates opposing effects, and the length of the Bay produces a local response of the same order of magnitude as the remote response, allowing them to nearly cancel out.

The most effective forcing frequency is that approaching the natural seiche frequency of the basin, where a small phase mismatch in the increasing elevations can allow a large amplitude in the total current. It is interesting to consider that a similarly sized estuary, sited at right angles to the coastline, where the effects would be independent, would regularly experience flows at the mouth 3 times that of the model solution illustrated in Figure 4.16. Furthermore, for an estuary angled so that the effects reinforced each other (e.g. downwelling winds could cause local setup) the model predicts exchange flows of over 80 cm/s for a wind stress of 0.1 Pa.

4.3.7 Meteorological Control of Bay/Shelf Exchange: Summary

In the preceding sections, it has been shown that barotropic exchange across the Bay mouth, as inferred from fluctuations of the volume of water within the Bay, is dominated on the synoptic time scale by meteorological forcing, rather than gravitational circulation or tributary input. The timing of the arrival of low salinity intrusions off of North Carolina was significantly related to patterns of large barotropic outflow events, as shown in Table 4.2. The spectral analysis revealed that the volume exchange due to long period synoptic winds displayed a response indicative of remote control by coastal sea levels. Shorter period fluctuations, which were more energetic due to enhancement by the natural seiche response of the Bay, appeared to be related directly to frictional driving by the local north-south winds.

For bay/shelf exchange induced by coastal sea level, the time of peak outflow would follow a downwelling event, or coincide with the

beginning of an upwelling period. The low salinity plume released at this moment could be transported offshore by these upwelling winds (see next chapter) and would not be observed along the inner shelf to the south. The peak in volume flux noted on 23 September (Figure 4.3IIa) is an example of this scenario. If this were the most common mode of producing a large outflow from the Bay, then low salinity intrusions would be rarely observed along the North Carolina coast.

However, both the spectra and the time series from 1994 indicate that the Bay/shelf exchange is most efficiently forced directly by the north-south wind. The analytical model, using a decreasing α , produced the largest total exchange flow for a nearly along-estuary (10° to 20° off north-south) wind. Peak flow is best observed when a waning northward wind allows the along-Bay setup to relax, as shown by the correspondence between negative peaks in $d\text{Wind}V/dt$ and in $\frac{d\text{Vol}}{dt}$ (Figure 4.3, panel a). This often occurs as an upwelling wind reverses to downwelling, a condition that was shown in the previous chapter to be optimal for the sustained presence of a buoyant jet over the inner shelf. The periods of intense outflow are brief, being cut off by the rising coastal sea level or the seiche rebound. At times, a relaxation in the northward wind can occur without complete reversal, producing an outflow surge while maintaining upwelling conditions. If the outflow is strong enough, or the northward wind weak, a southward-propagating plume can still form (see Figure 4.3Ia, events A,B ; Figure 4.3IIa, event G ; Figure 4.3IIIa, event M). But with strong continued northward winds, the outflow must be dispersed offshore, as happened to the outflow of 29 July (Figure 4.3Ia). On occasion, a peak in $\frac{d\text{Vol}}{dt}$ occurs without an accompanying decrease in along-shore wind stress, e.g. on 25 August and 4 October, perhaps due to a

free seiche oscillation. In both these cases, no evidence of a low salinity water mass is seen, suggesting that both volume flux and wind changes must occur together to allow the formation of an intrusion.

When the Bay is stratified into a two-layer system, as during the summer, one would anticipate a baroclinic response with the longer time scale, $\frac{L}{\sqrt{g' h}}$, closer to that of the atmospheric forcing. From the model solutions, it is clear that that local response would be enhanced (larger W in eq. 4.5b & d, section 4.3.4). In addition, in a stratified bay, the local wind-forced setup and relaxation should preferentially store and release the fresher water held above the seasonal thermocline. It has been shown that the lateral pycnocline across the Bay normally tilts upwards towards the eastern shore in geostrophic response to the typical estuarine circulation of down-Bay flow in the surface waters and up-Bay in the deeper part. However, the pycnocline can reverse its slope during periods of strong north-northeastward winds, indicating a reverse pattern of flow in the vertical (Frizzell-Makowski, 1996). That study included current profile observations from the upper Chesapeake Bay from June, 1993 that showed a reverse pattern of along-estuary flow during up-Bay winds, which changed to outflow throughout the water column as the northward wind stress diminished. This down-Bay flow of 30 to 40 cm/s was maintained for over 10 hours. With this scenario, the above-pycnocline source of the surging outflow would enhance its buoyancy. This may explain the better relationship between the volume flux and the observed plume events during August, before the autumn destratification of the Bay.

The simple modeling exercise illustrates how the opposing mechanisms create a complex response to changing wind frequency and direction. In particular the flow patterns at the mouth undergo dramatic

changes as the seiche frequency is approached as the phase difference between the remote and local responses increases while the elevations are enhanced. A cross-shore wind component is seen to enhance the exchange by affecting the local response.

Wind components produced by coherent mesoscale meteorological patterns are themselves correlated (see section 3.3), making it difficult to separate out the responses in observations. On the east coast of the US, northward wind patterns tend to rotate clockwise (see Figure 4.I:IIIId) as cyclonic lows formed along the juncture of warm land and cool ocean propagate north or northeastward (Austin and Lentz, 1998). This causes decreasing northward wind stress to be usually accompanied by an increasing offshore wind component. Under these circumstances, both wind components reinforce each other, producing the enhanced outflows observed following most upwelling periods.

4.4 Down-coast Freshwater Flux

The timing of occurrences of low salinity plumes observed off the North Carolina coast is clearly controlled by the meteorological patterns that control the variability of the source estuarine exchange. The question remains how much of the freshwater flowing out of the Bay is delivered directly southward over the inner shelf by these distinct intrusions. There are several possible approaches that would provide a rough estimation of the freshwater flux present in the plume intrusions off of Duck. First the prevailing ambient shelf salinity with which the intrusions are mixing must be established. This is best represented by the mid-water column salinities observed at the 25m mooring, which were not directly

influenced by distinct low salinity water masses. These series all displayed a similar decrease with time, and the ambient shelf salinity is adequately represented by

$$S_{\text{ambient}} = 34.77 - 0.025 * (\text{days since Aug 1}^{\text{st}})$$

determined as described for S_{maxplume} in section 3.3. The ambient salinity averages from over 34 psu in August, down to 32.5 psu by the end of October. The percentage of freshwater is then computed as

$$\% \text{Fresh} = 1 - \frac{S_{\text{observed}}}{S_{\text{ambient}}}$$

CTD transects were taken at least once across most of the plume events. A contoured salinity cross section of this data (e.g. Figure 3.4) allows the quantification of freshwater volume per unit coastline. This was done with all events for which a transect was available (Table 4.3).

Event	Area m ²	FreshVol m ³ /m	Cobs cm/s	FreshFlux m ³ /s
P 8/07	45375	5510	58	3196
A 8/16	21250	2854	59	1670
B 8/20	31062	3545	56	1985
C 8/23	61375	6359	72	4578
D 8/28	no transect		46	
E 8/31	16125	2829	52	1457
F 9/02	no transect		68	
G 9/09	30500	3496	50	1731
H 9/19	no transect		60	
I 9/30	no transect		57	
J 10/04	135500	10744	46	4889
K 10/11	135000	9110	48	4373
L 10/18	45125	4265	67	2836
M 10/22	32375	3350	43	1441
N 10/26	120000	11780		
AVERAGES	61244	5804	56	2815

Table 4.3

Estimation of freshwater flux based on CTD transects across each plume event.

The average cross sectional area (column 3) of the regions with salinities less than S_{maxplume} was 61244 m², consistent with that determined in section 3.3 based on pycnocline depths and surface salinity front locations. Using the observed along-coast propagation speed of each intrusion as the velocity with which this water mass is traveling, an estimate for freshwater flux is reached (column 5).

Alternatively, based on the cross-shore structure described in section 3.3, cross sectional areas can be assigned to each time series of salinity available from the moorings, from which, along with the co-located velocity measurements, an hourly series of freshwater flux across the central mooring line can be computed. A reasonably complete coverage of the plume region is possible only when both the 13-m and 20-m surface moorings were available, confining this method to the time period between 6 August and 4 September. This time series is compared in Figure 4.19 with the above estimates from the CTD transects. The two methods agree fairly well, with the CTD transects tending to give a slightly larger value. Since the velocities are expected to be highly sheared (see section 3.5) and surfacemost current meters are at a depth of 4 m, one would expect the flux from the mooring data to be somewhat underestimated. The average southward flux of freshwater recorded by the moorings for this time period is 1110 m³/s. The average flux observed by the CTD transects for events within this time is 2600 m³/s, which would then imply that these events were present just over 40% of the time, which is reasonably consistent with the results in Figure 3.6B. The tributaries had a mean flow of 1253 m³/s during July and 2312 m³/s during August. The exact time lag between tributary inflow and Bay/shelf exchange is not well known, but is estimated to be on the order of several

weeks to a month. It would appear then that between 50 and 80% of the freshwater input from the Chesapeake tributaries can be accounted for by the observed freshwater flux within the low salinity intrusions along the North Carolina coast.

Another estimate of freshwater flux out of the Bay can be derived from our estimates of volume flux, if a representative salinity at the Bay mouth is assumed. The shipboard underway salinity mapping system recorded values of 22 to 23 psu while transiting through the Bay mouth area during August. A similar salinity range was observed by Valle-Levinson et al. (1994) during their July and August monthly Lower Chesapeake Bay surveys. Using this %Freshness of one-third, $\frac{dVol}{dt}$ was transformed into a time series of freshwater flux, which was then lagged by 42 hours for the best match to the mooring-based flux estimates in Figure 4.19. This comparison shows that some of the freshwater outflow events are not seen at the moorings, and the mean flux determined by this method (2156 m³/s) implies that 50% of the freshwater outflow from the Bay was not observed along the inner shelf, confirming the lower end of the range given above.

Figure 4.1. Streamflow into the Chesapeake Bay during the summer and fall of 1994.

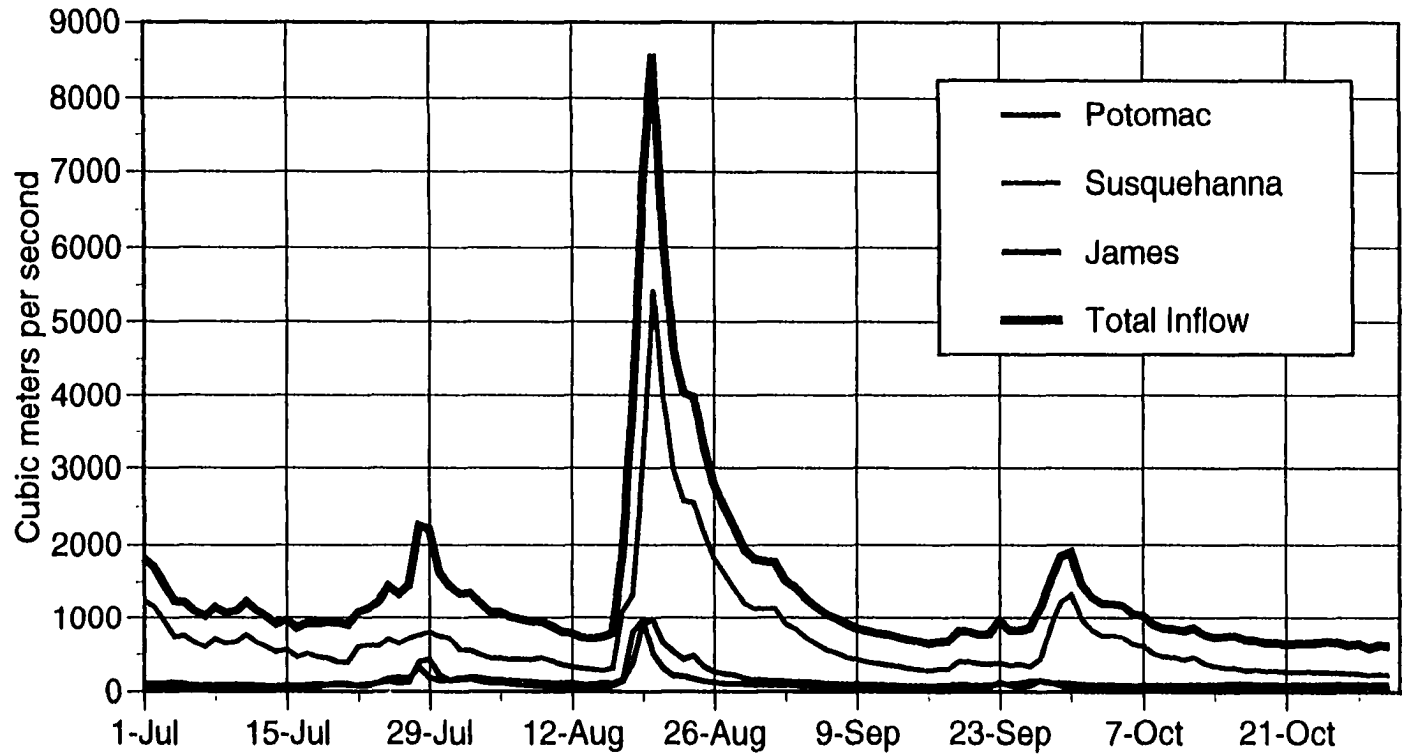


Figure 4.1. Gauged streamflow into the Chesapeake Bay during the summer and fall of 1994.

Figure 4.2 Location of water level stations and NOS current meter station 040 (1982) within the Chesapeake Bay. Shaded regions indicate area assigned to nearest water level gauge for volume flux calculations.

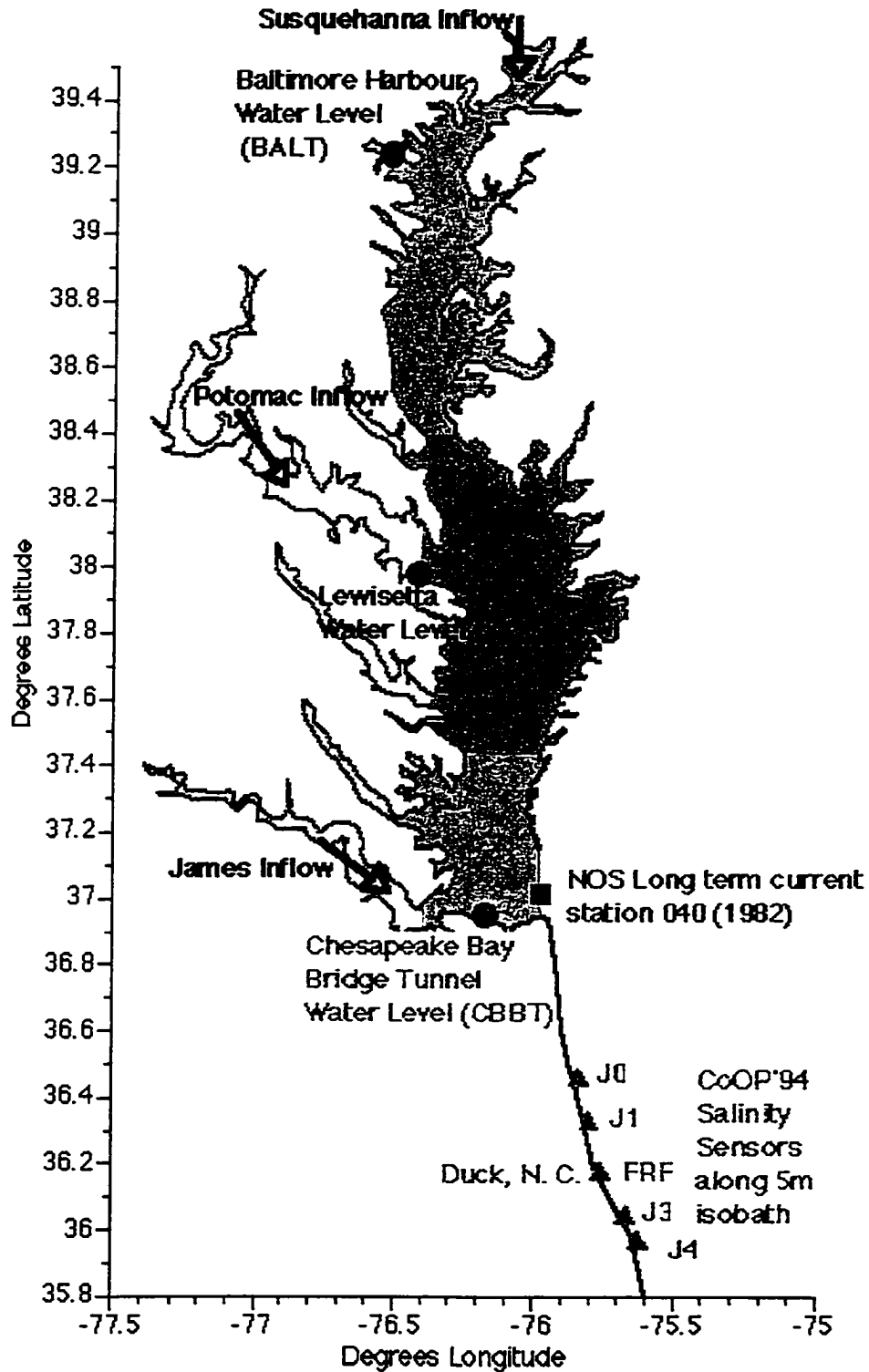


Figure 4.2. Location of waterlevel records and NOS current meter station 040 (1982) within the Chesapeake Bay. Shaded regions indicate area assigned to nearest water level gauge for volume flux calculations.

Figure 4.3 Low pass time series from I: August; II: September; III: October 1994. a) Subtidal volume flux from waterlevels in the Chesapeake Bay overlaid by time rate of change of the north-south wind component. b) Salinity recorded at FRF pier. c) Total volume (integrated volume flux). d) winds from Chesapeake Light Tower.

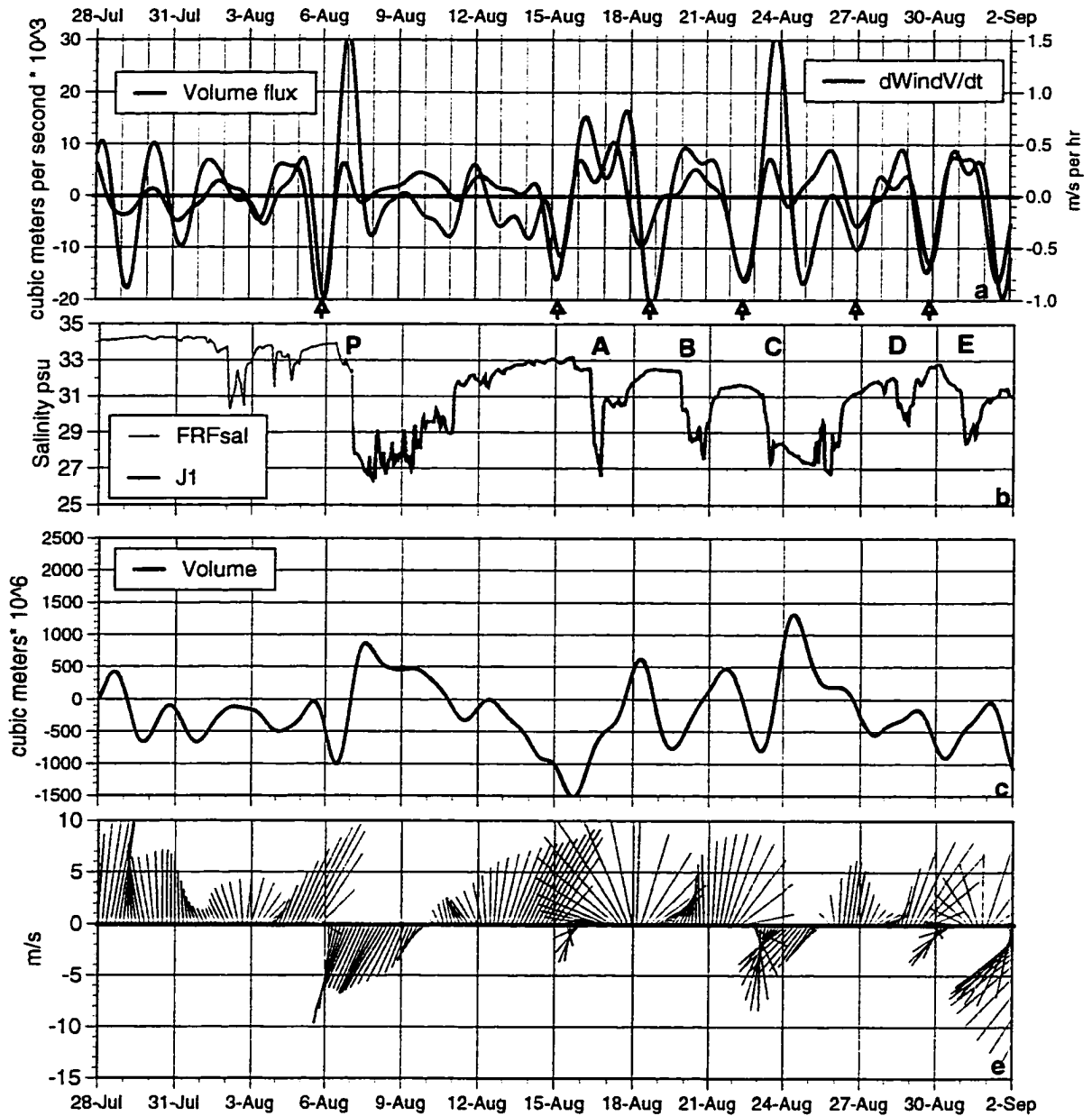


Figure 4.3 I. Low passed time series from August 1994.

- a) Subtidal volume flux from waterlevels in the Chesapeake Bay overlain by time rate of change of the north-south wind component.
- b) Salinity recorded at FRF pier. c) Total volume (integrated volume flux). d) winds from Chesapeake Light Tower.

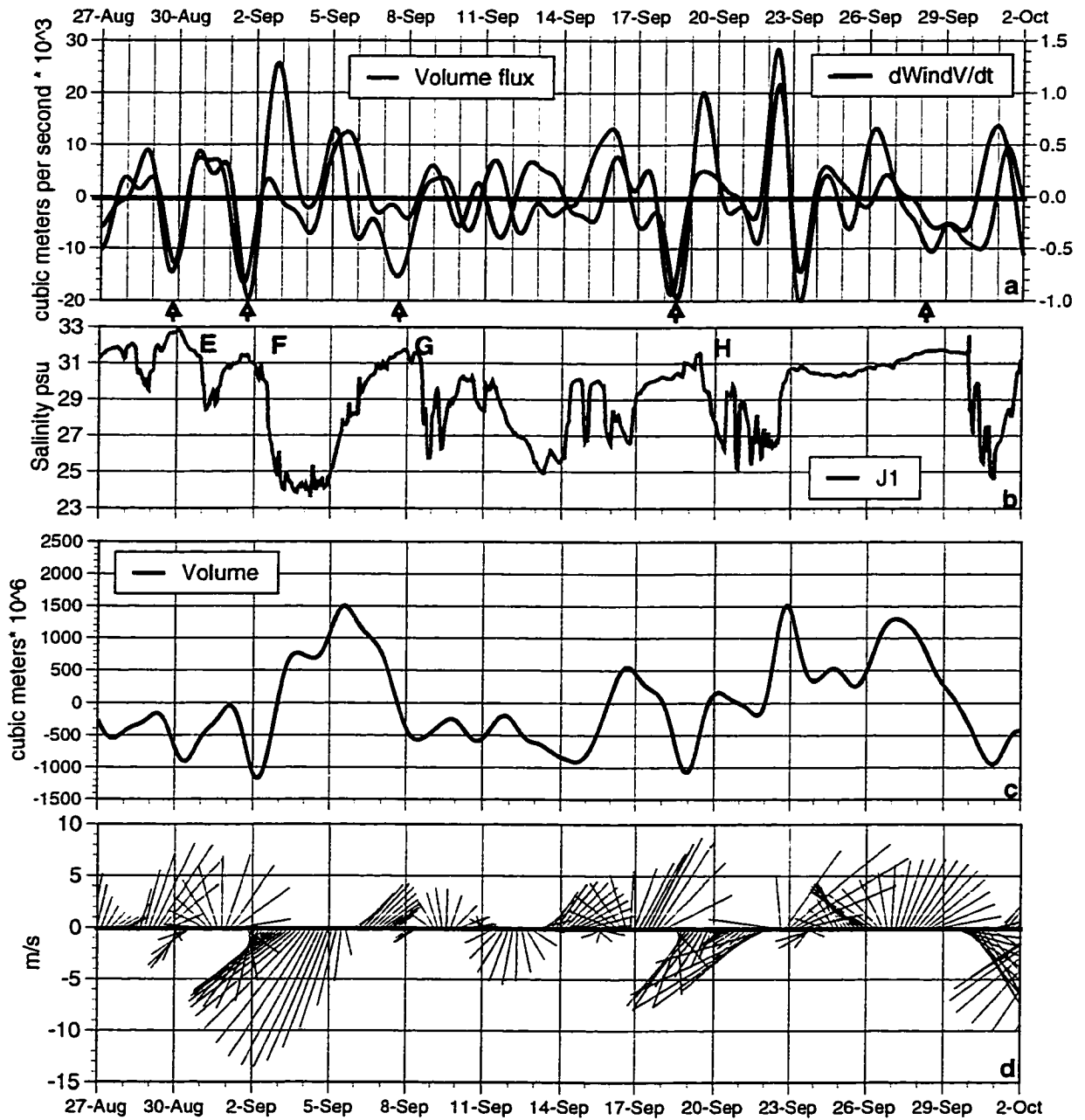


Figure 4.3 II. Low passed time series from September 1994.
 a) Subtidal volume flux from waterlevels in the Chesapeake Bay.
 b) Salinity recorded at FRF pier. c) Total volume (integrated volume flux). d) winds from Chesapeake Light Tower.

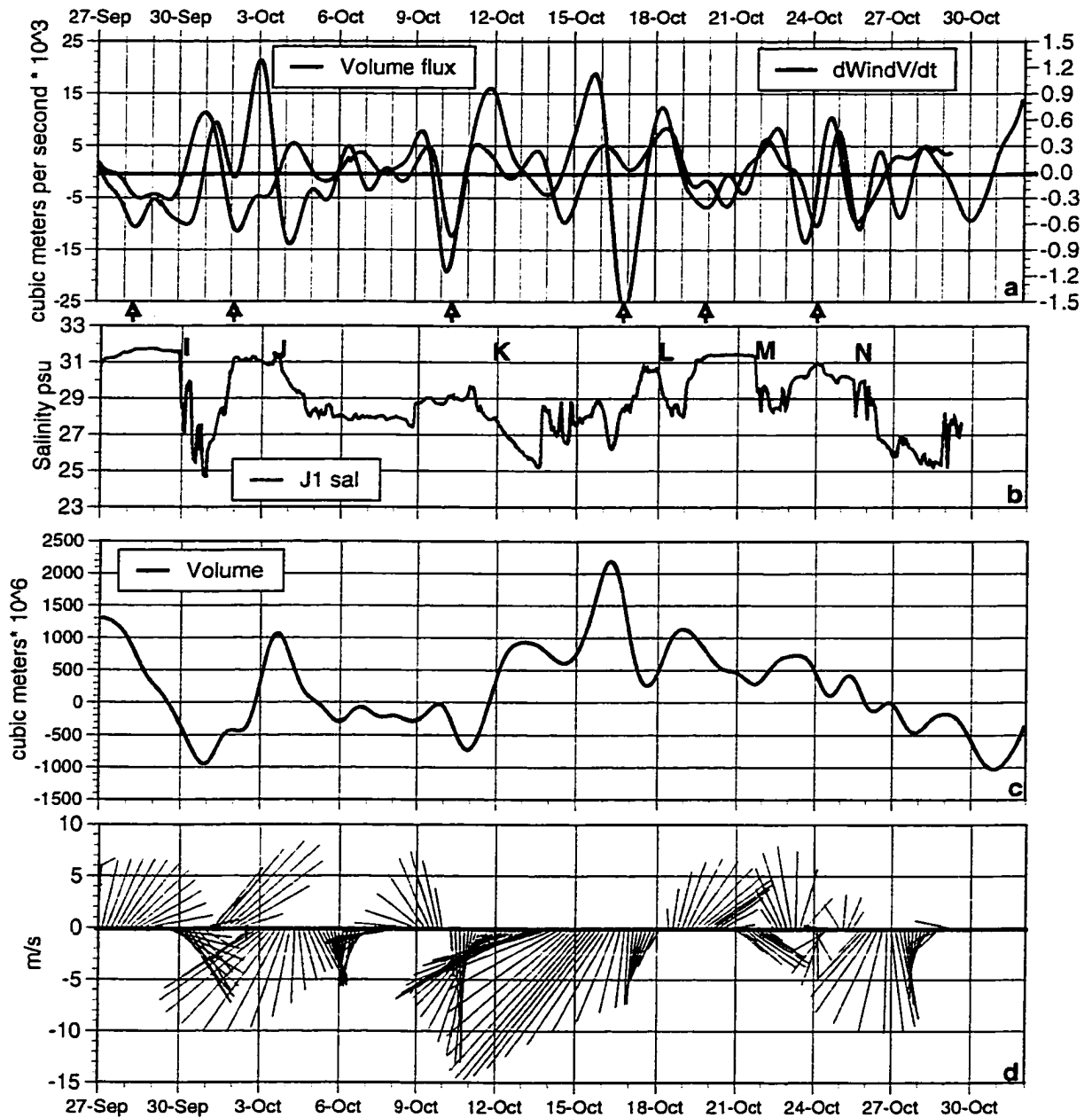


Figure 4.3 III. Low passed time series from October 1994.
 a) Subtidal volume flux from waterlevels in the Chesapeake Bay.
 b) Salinity recorded at FRF pier. c) Total volume (integrated volume flux). d) winds from Chesapeake Light Tower.

Figure 4.4. Power spectrum of volume flux as calculated from waterlevels in the Chesapeake Bay for August through early October 1994; plus the spectra of the coastal wind stress components; and the spectrum of the tributary inflow.

.

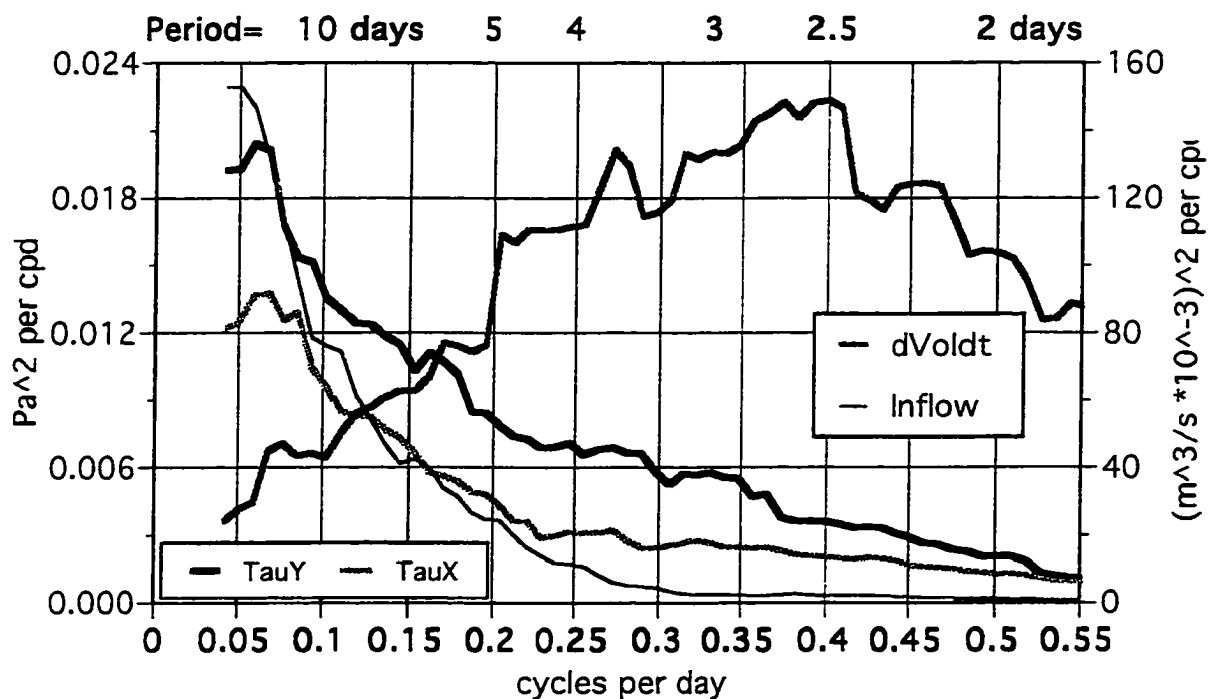


Figure 4.4. Power spectral density of volume flux as calculated from waterlevels in the Chesapeake Bay for August through October 1994, plus the spectra of the coastal wind stress components, and the tributary inflow. Degrees of freedom = 50, (= 18 for freq < .11 cpd).

Figure 4.5. Along-coast position of southward-propagating low salinity intrusion versus time in days measured from the moment of passage by sensor J1. Solid line: frontal position achieved at steady propagation speed of 55 cm/s; dashed line: 75 cm/s; dotted line: 35 cm/s.

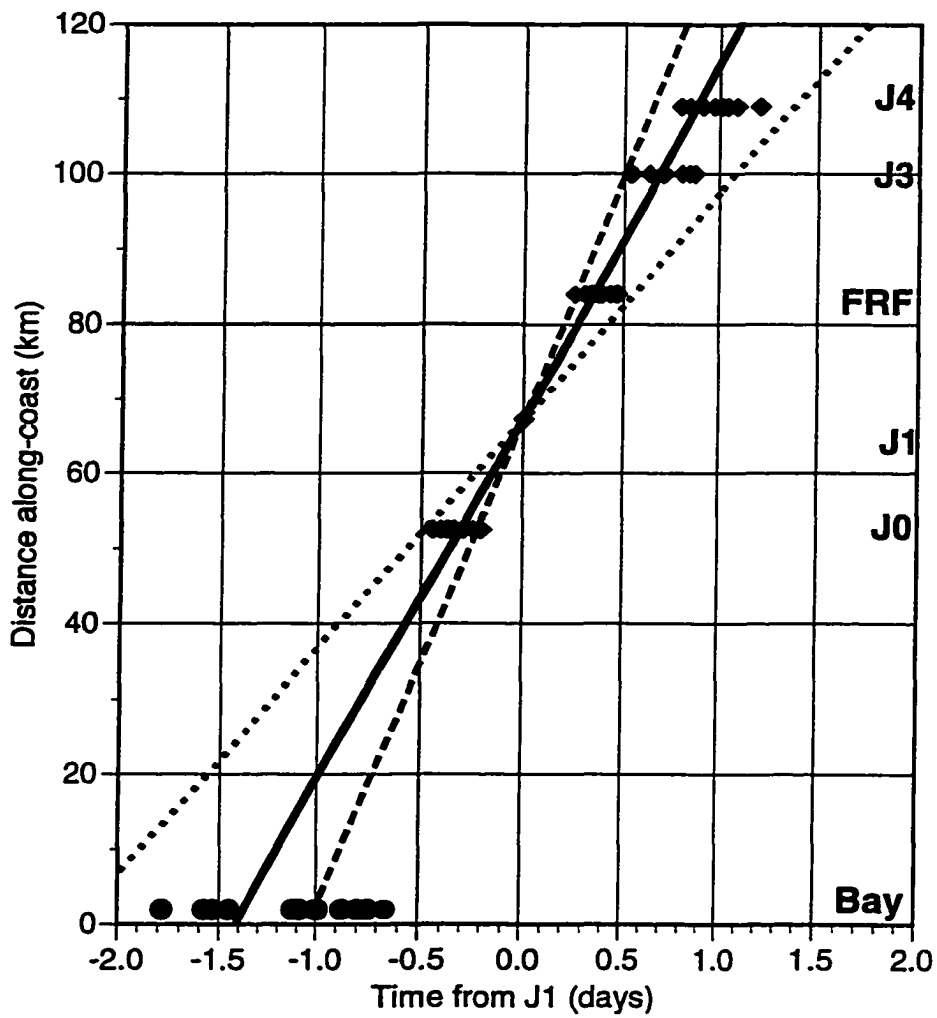


Figure 4.5. Along-coast position of southward-propagating low-salinity intrusion versus time in days measured from the moment of passage by sensor J1. Solid line: frontal position achieved at steady propagation speed of 55 cm/s; dashed line: 75 cm/s; dotted line: 35 cm/s.

Figure 4.6. Correlation between along-shore wind stress and a) along-shore current or b) salinity at the uppermost instruments on the 13-m mooring *versus* lag in hours.

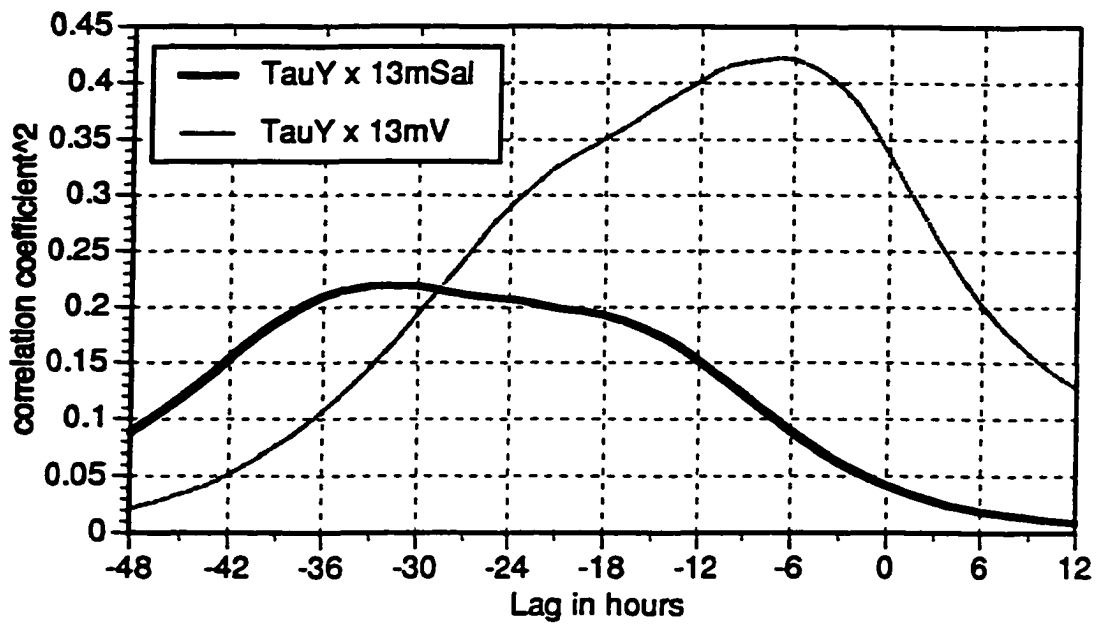


Figure 4.6 Lagged correlation coefficients (squared) between hourly alongshore wind stress and (dotted line) alongshore current at 4m depth and (solid line) surface salinity at the 13m mooring.

Figure 4.7 Diagram of remote vs local effect of meteorological forcing on the Chesapeake Bay.

Concepts for meteorological control of Bay/Shelf exchange

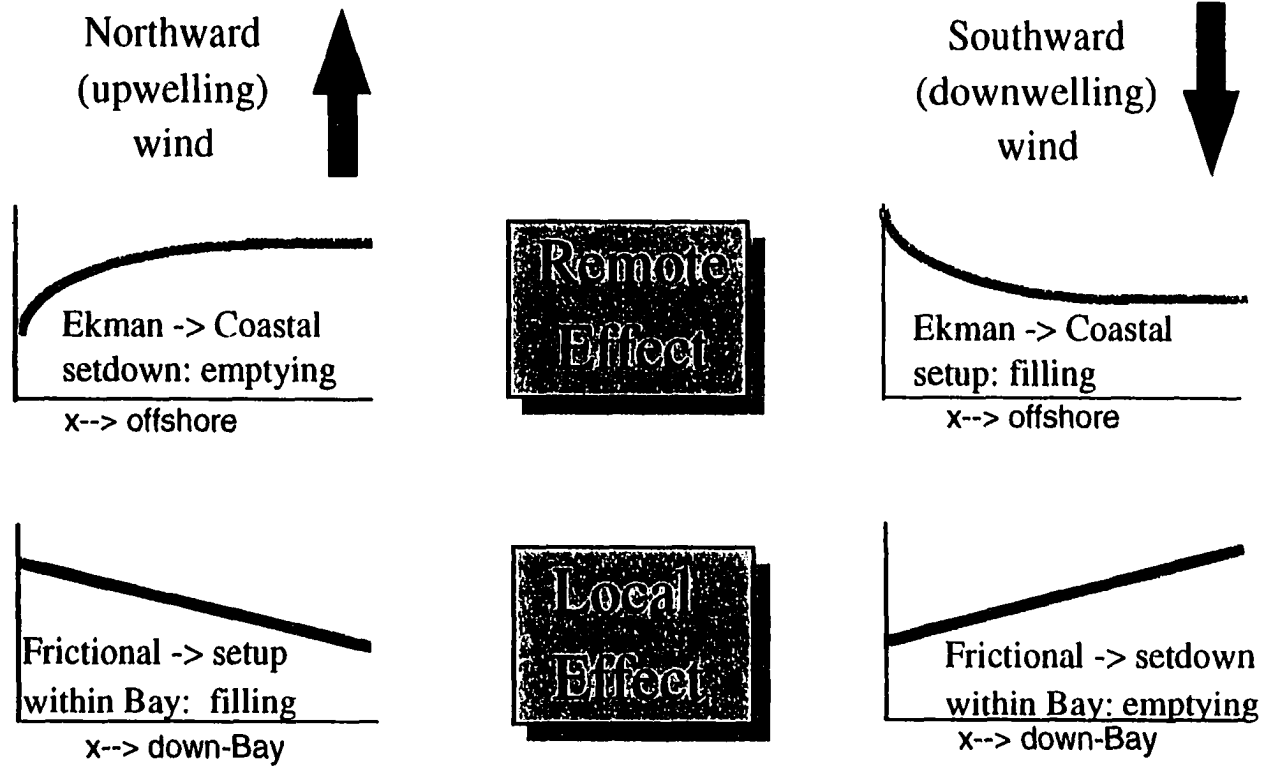


Figure 4.7 Diagram of Remote vs Local effect of meteorological forcing on the Chesapeake Bay.

Figure 4.8. Coherence and phase relationships for cross-spectra between coastal wind stress components and volume flux as calculated from waterlevels in the Chesapeake Bay for August through early October 1994.

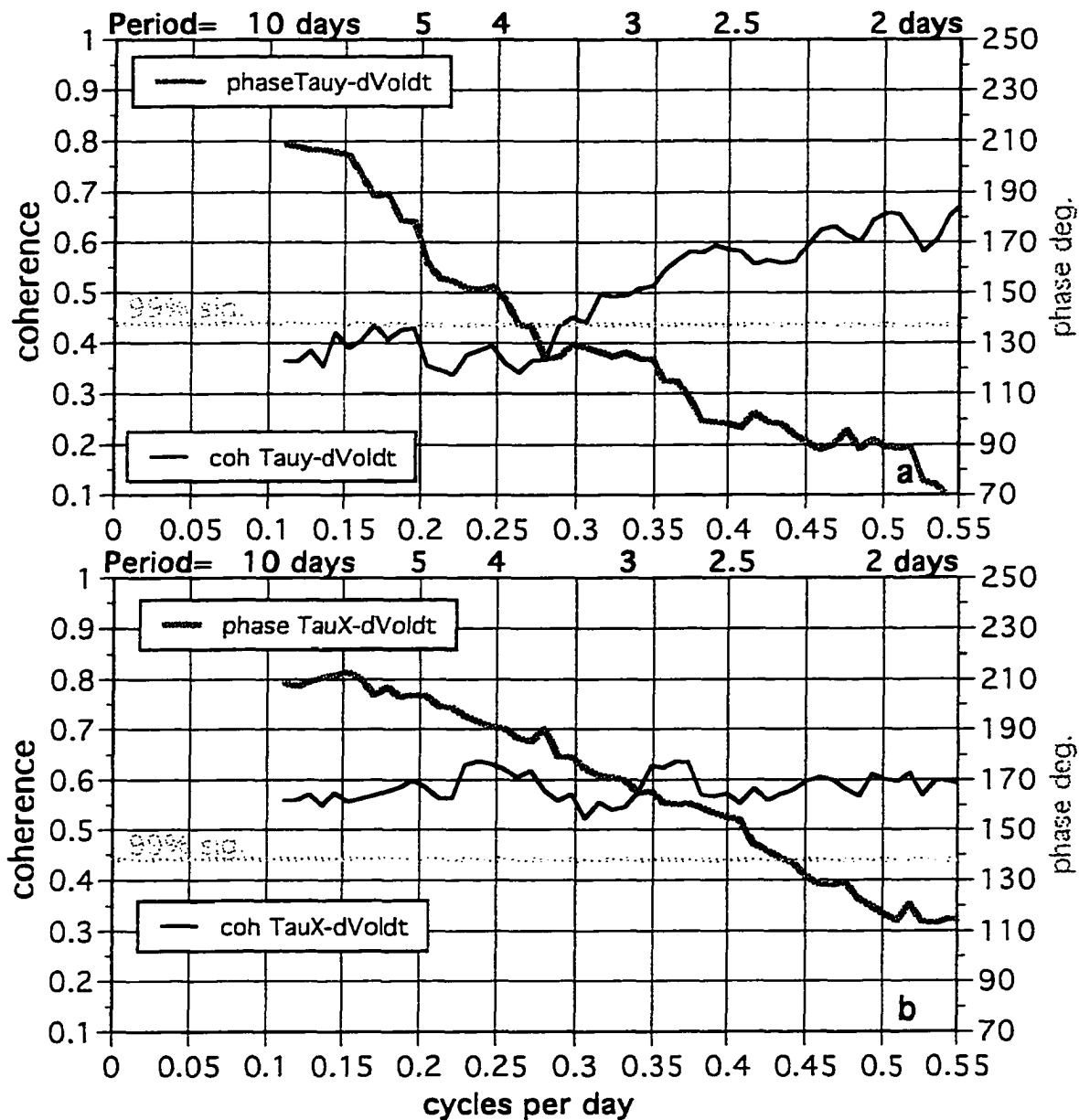


Figure 4.8. Coherence and phase relationships for cross spectra between coastal wind stress components and volume flux as calculated from waterlevels in the Chesapeake Bay for August through October 1994.

Figure 4.9. Time series of measured and estimated sub-tidal current through the Bay mouth (1982).

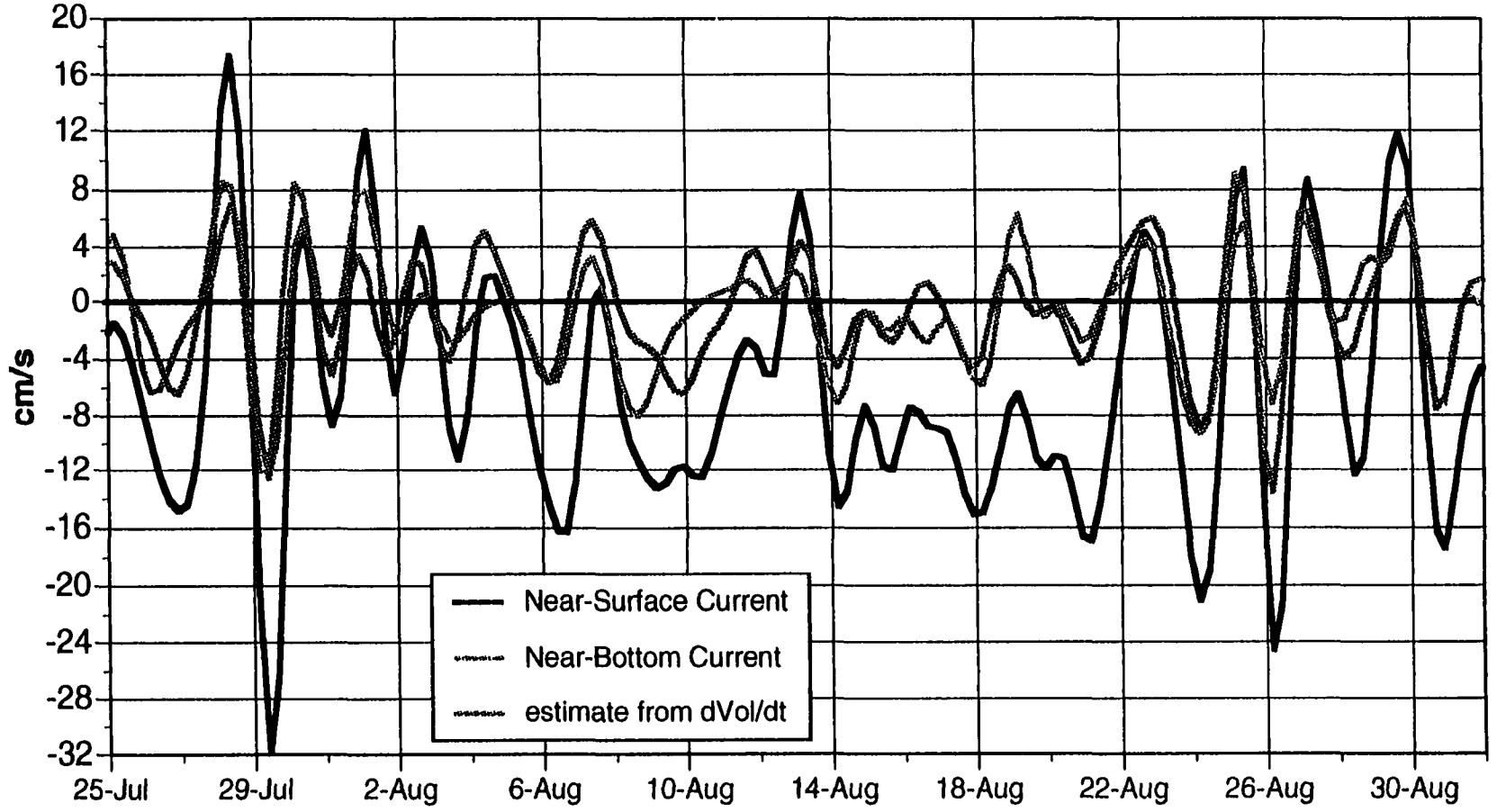


Figure 4.9. Currents from main channel at Bay mouth measured in summer, 1982 compared with estimated flow derived from volume flux divided by area of Bay entrance.

Figure 4.10. a) Spectra of volume flux computed from waterlevel variations and measured current and salinity from Stn40 for July to October, 1982. b) Coherence and phase between volume flux and top current (solid line) and bottom current (dashed line) . c) Coherence and phase between current and salinity.

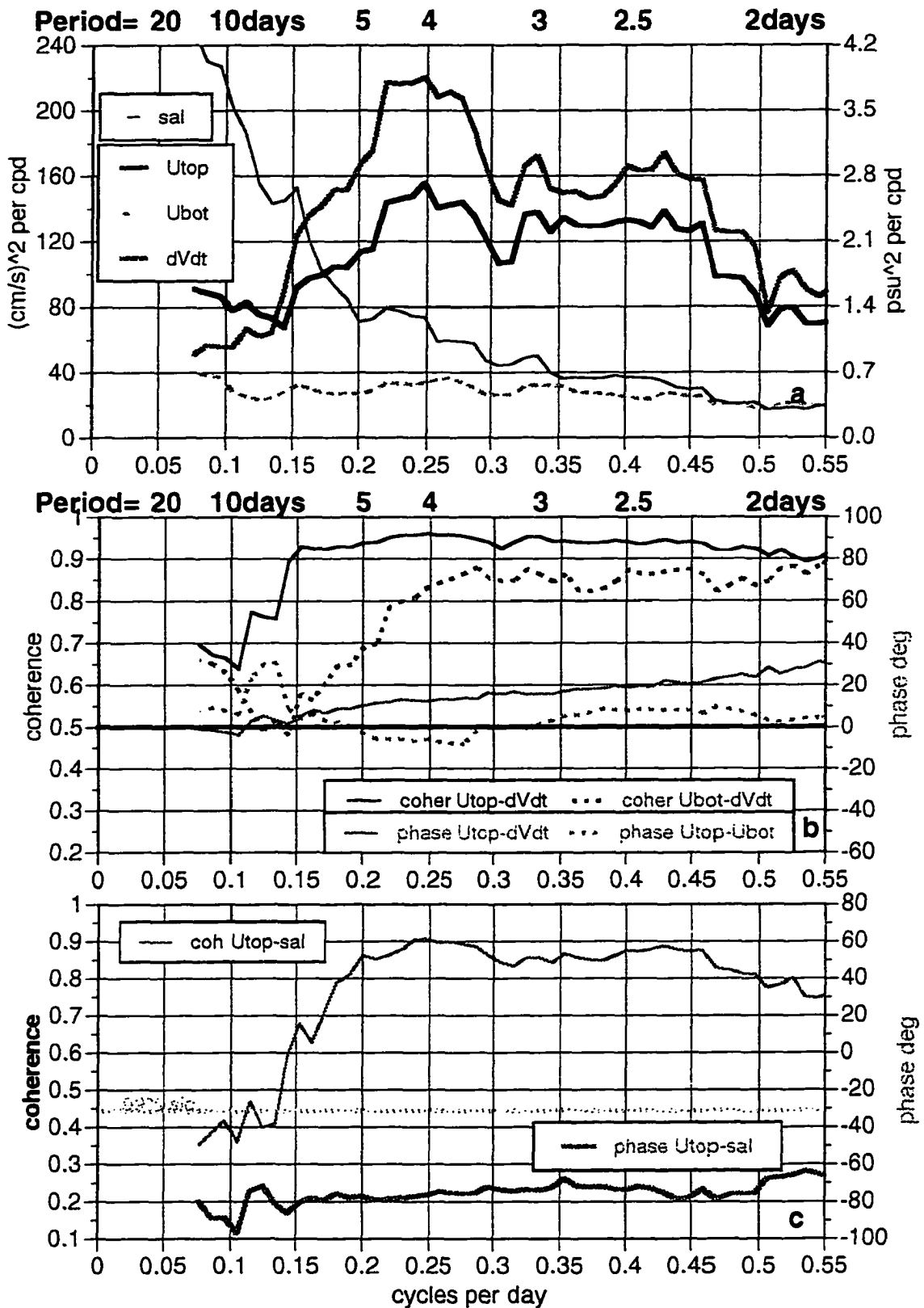


Figure 4.10. a) PSD of volume flux and measured current and salinity from Stn40. b) Coherence and phase between volume flux and top current (solid line) and bottom current (dashed line). c) Coherence and phase between current and salinity.

Figure 4.11. a) Spectra of volume flux and wind stress components from July to October, 1982. b) Coherence and phase between north-south wind and volume flux. c) Coherence and phase between east-west wind and volume flux.

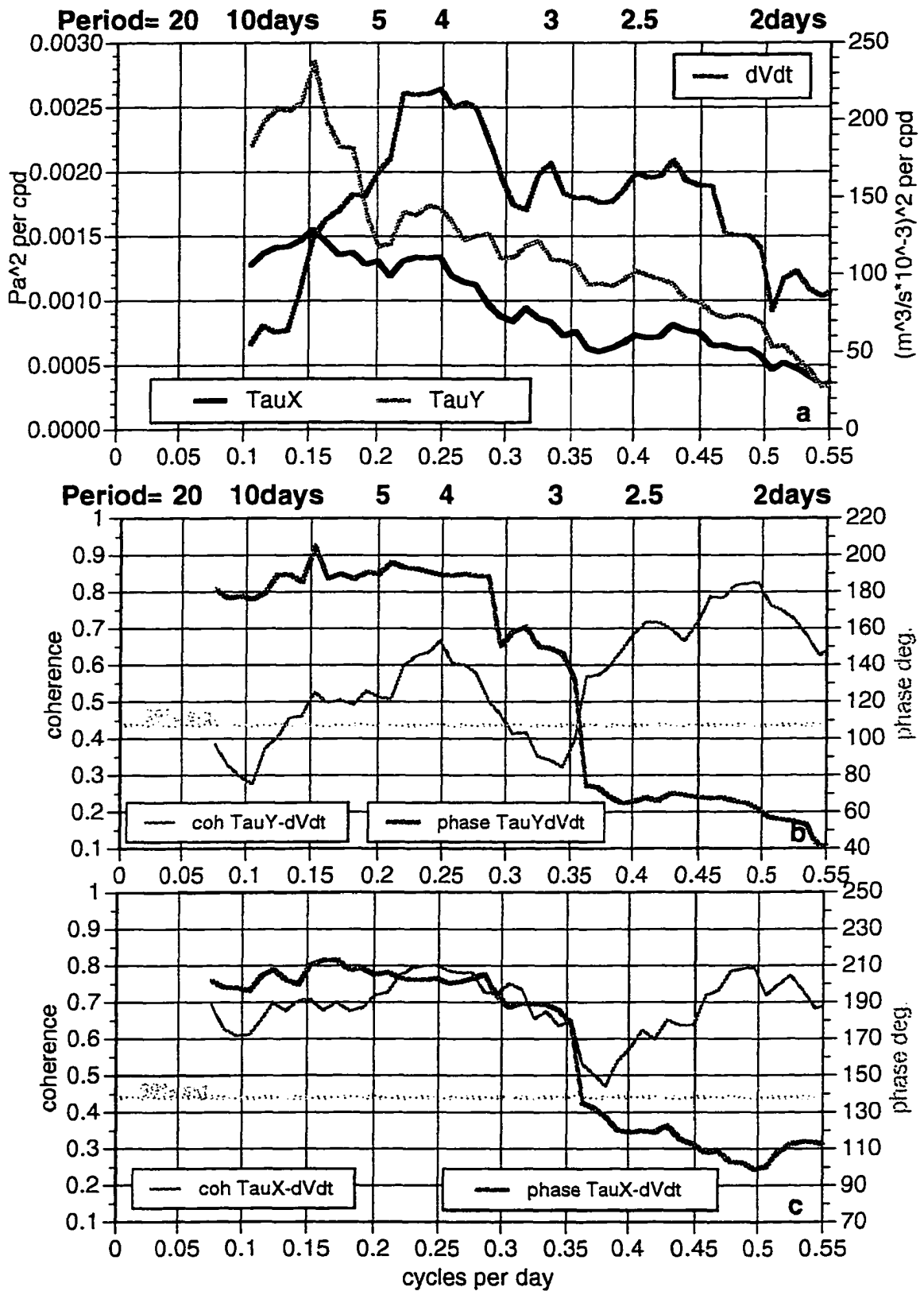


Figure 4.11. a) PSD of volume flux and wind stress from July to October, 1982. Degrees of freedom = 30. b) Coherence and phase between north-south wind and volume flux. c) Coherence and phase between east-west wind and volume flux.

Figure 4.12. Power spectra of waterlevels from the head (BALT) and mouth (CBBT) of the Chesapeake Bay for August through early October 1994.

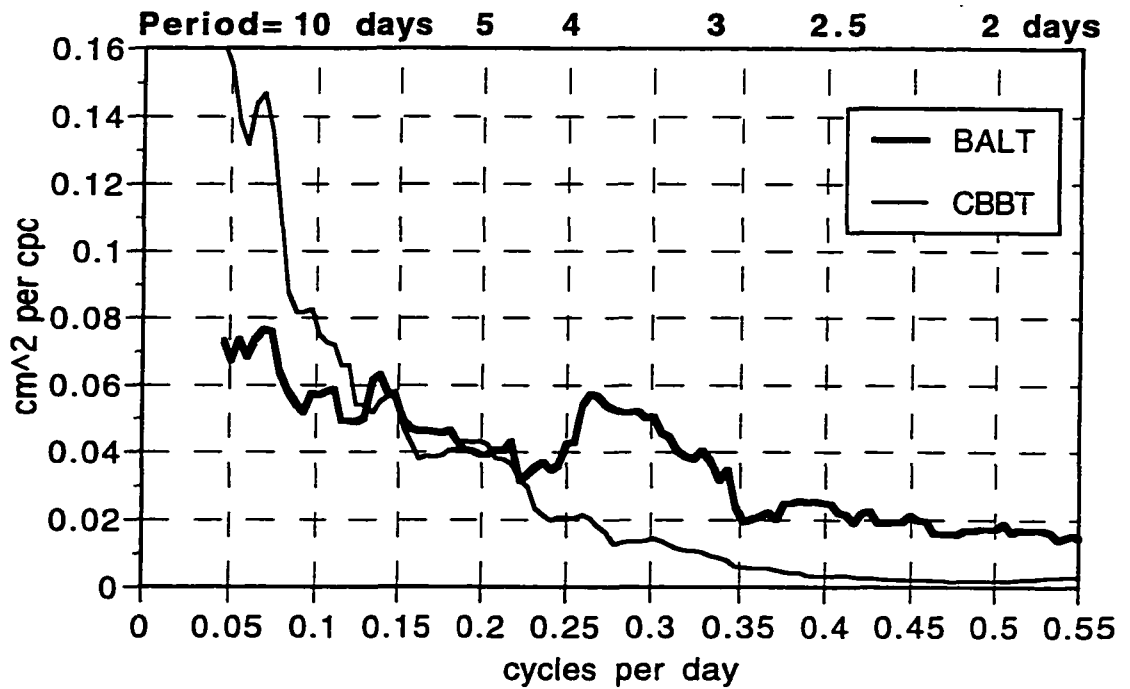


Figure 4.12. Power spectra of waterlevels from the head (BALT) and mouth (CBBT) of the Chesapeake Bay for summer through fall 1994. Degrees of freedom = 38.

Figure 4.13. Coherence and phase of cross spectrum between volume flux ($dVol/dt$) and the salinity recorded along the 5m isobath at location J1. Number of degrees of freedom is 30.

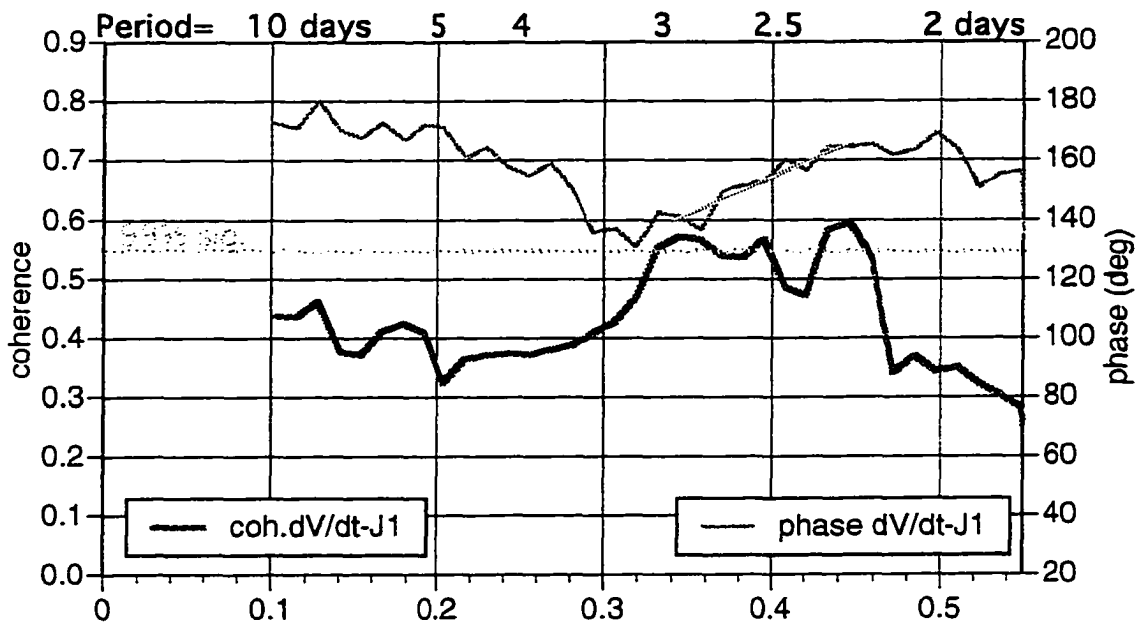


Figure 4.13. Coherence and phase of cross spectrum between volume flux (dV/dt) and the salinity recorded along the 5m isobath at location J1. Number of degrees of freedom is 30.

Figure 4.14. Diagram of analytical model geometry (after Garvine (1985), Figure 1).

Figure 4.15. Upper panels: Amplitudes of surface elevations due to along-shore wind of amplitude 0.1 Pa in a basin length of a) 100 km and b) 290 km for a forcing time scale of $T=7$ days at times when wind is maximum: $t=0$ (dashed) and $t = 1/2 \cdot T$ (solid). Response is separated into remote (blue) and local (green) effects. The combined total response is shown in red. Lower panels: Current in the two different length basins. Flow shown is maximum, occurring at one quarter cycle before maximum elevation.

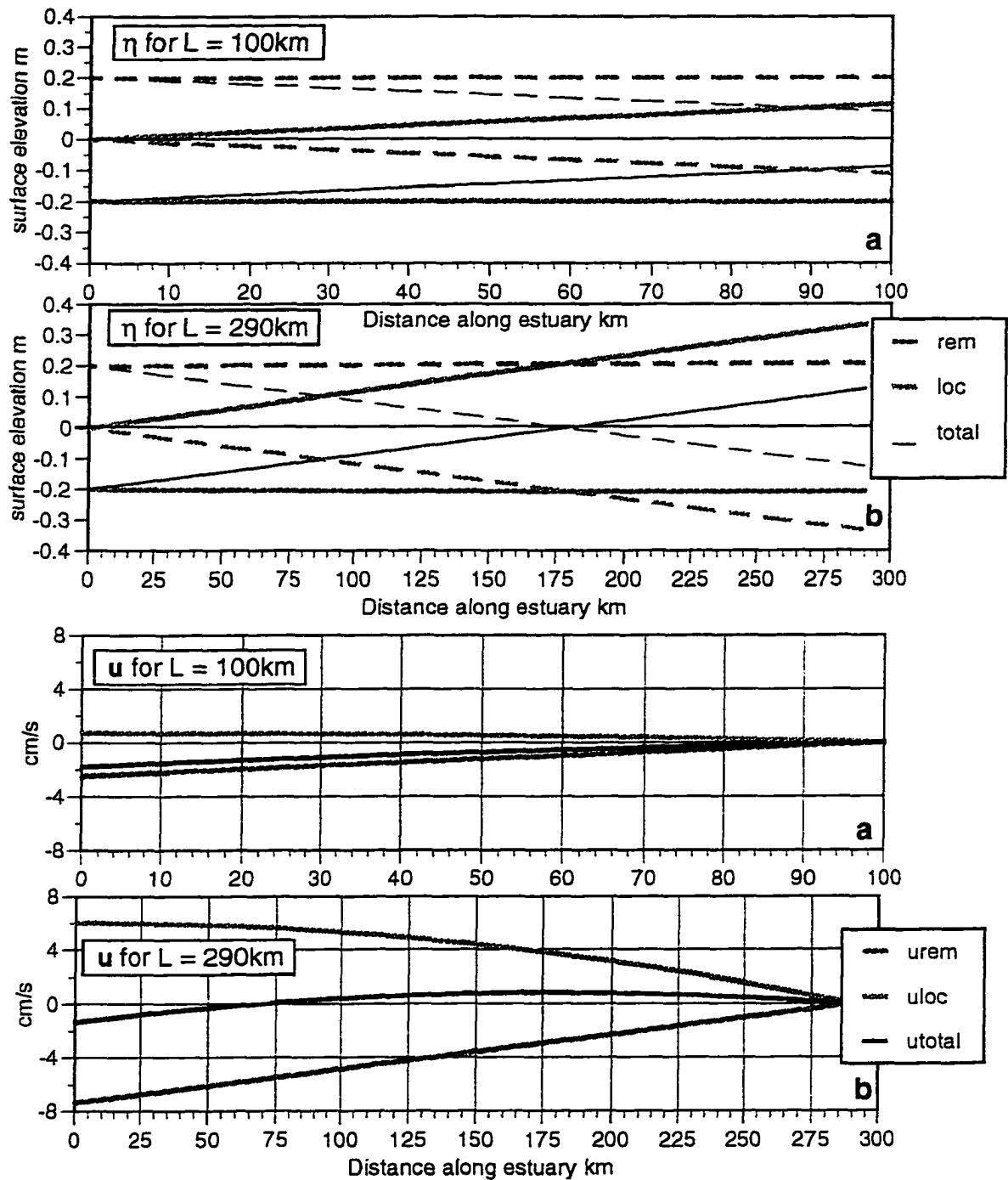


Figure 4.15. Upper panels: Amplitudes of surface elevations due to alongshore wind = 0.1 Pa in a basin length of **a)** 100 km and **b)** 290 km for a forcing time scale of $T=7$ days at times when wind magnitude is maximum: $t=0$ (dashed) and $t=1/2 \cdot T$ (solid). Response is separated into remote (blue) and local (green) effects. The combined total response is shown in red. Lower panels: Current in the two different length basins. Flow shown is maximum, occurring at $1/4$ cycle before maximum elevation.

Figure 4.16. a) Amplitude of surface elevation at head of 290 km Bay due to remote and local forcing from purely along-shore wind stress $\tau_y = 0.1$ Pa. b) Phase relationship between wind forcing and surface elevation. c) Amplitude of resultant total current at mouth due to remote + local forcing, overlaid with ratio of local to remote contributions. d) same as c for linearly decreasing α from $\alpha = 1.9e-4$ @ $T=15$ days to $0.9e-4$ @ $T \leq 3$ days.

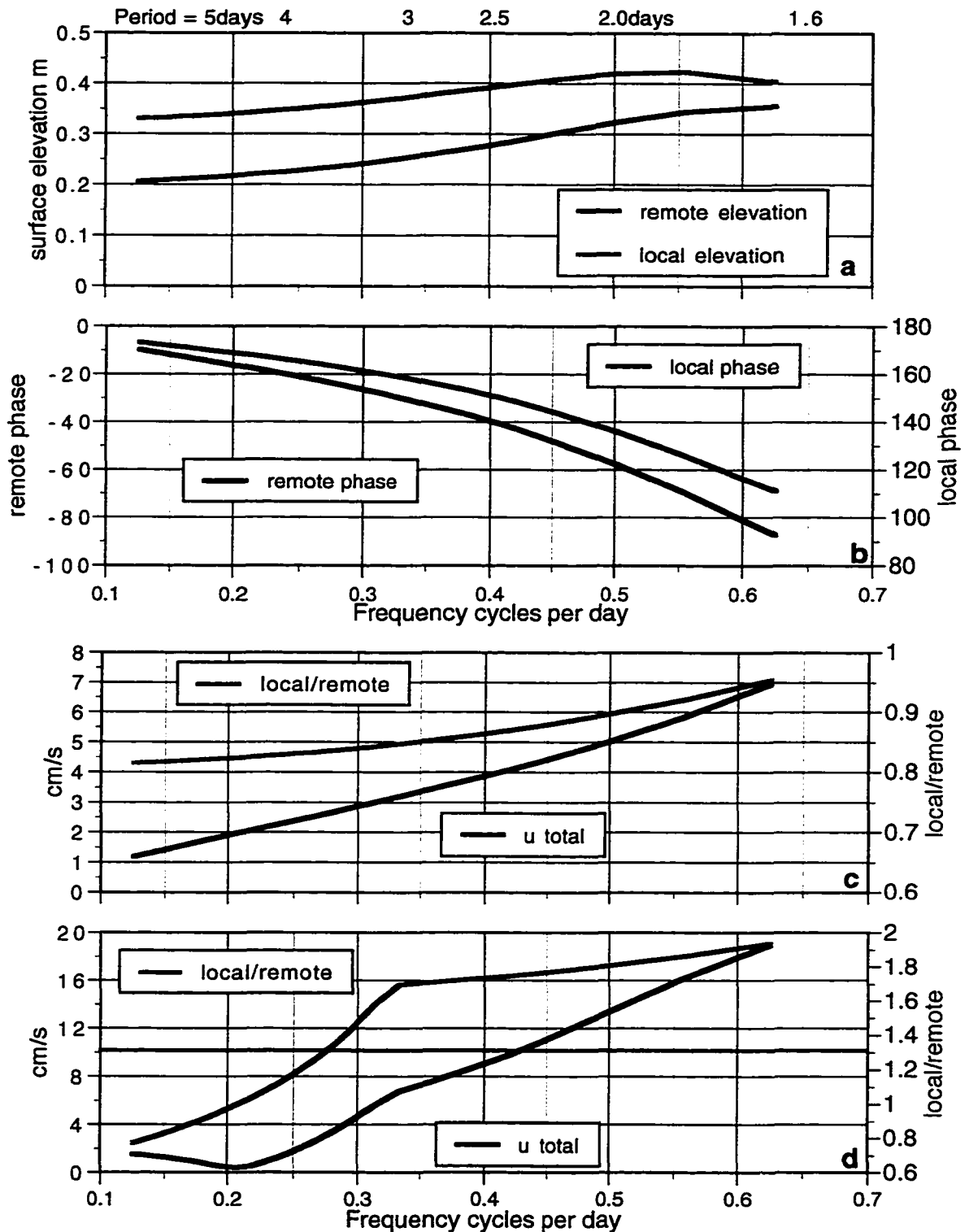


Figure 4.16. a) Amplitude of surface elevation at head of 290 km bay due to purely alongshore wind stress $\tau_y = 0.1$ Pa. b) Phase relationship between wind forcing and surface elevation. c) Amplitude of resultant total current at mouth due to remote + local forcing, overlaid with ratio of local to remote contributions. d) same as c for linearly decreasing α from $\alpha = 1.9$ @ $T=10$ days to 0.9 @ $T \leq 3$ days.

Figure 4.17. Amplitude of transfer function computed from cross-spectra of along-shore wind stress τ_y with a) waterlevel from mouth of Bay (CBBT) and b) waterlevel from head of Bay (BALT). Dotted line represents best fit of linearly-decreasing $\alpha(\text{freq})/f$ used for $0.05 < \text{freq} \leq 0.32$; $\alpha = \text{constant}$ for $\text{freq} > 0.32$.

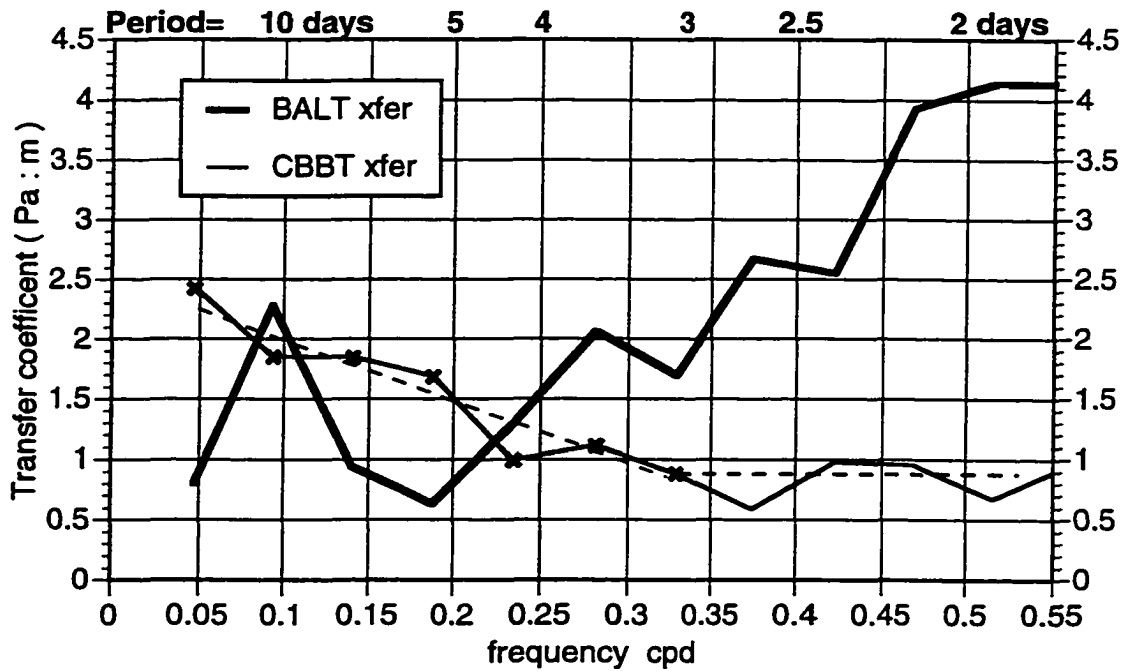


Figure 4.17. Amplitude of transfer function computed from cross-spectra of along-shore wind stress τ_y with a) waterlevel from mouth of Bay (CBBT) and b) waterlevel from head of Bay (BALT). Dotted line represents best fit of linearly-decreasing $\alpha(\text{freq})/f$ used for $0.05 < \text{freq} \leq 0.32$; $\alpha(\text{freq})/f = \text{constant}$ for $\text{freq} > 0.32$.

Figure 4.18. Amplitude of resultant total current at mouth of 290 km estuary due to combined remote + local forcing from wind stress of 0.1 Pa varied over direction θ . $\theta = 0^\circ$ is along-estuary; $\theta = 20^\circ$ is directly along-shore. a) fixed $\alpha = 1.8e-4$; b) case for decreasing α .

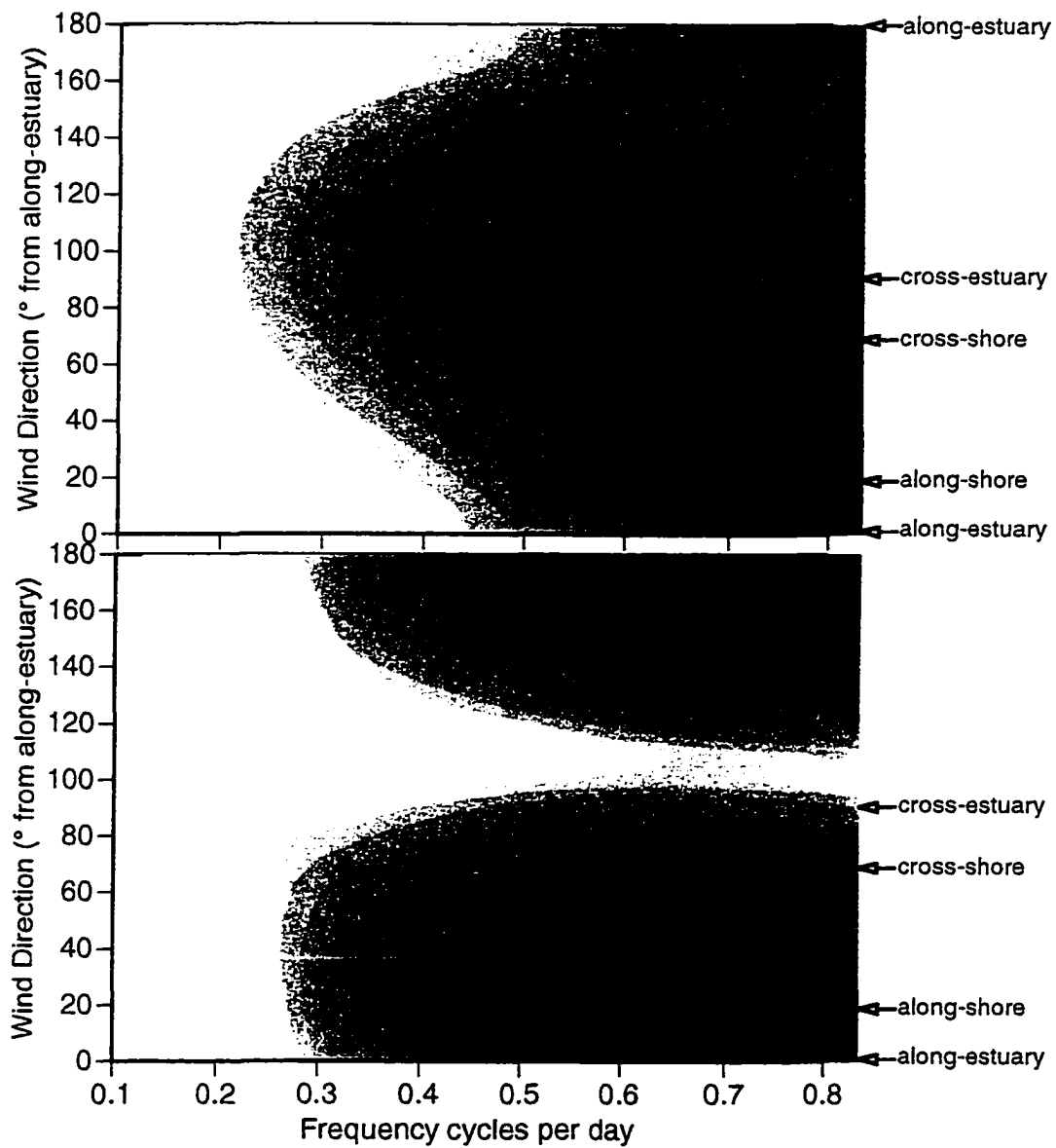


Figure 4.18. Amplitude of resultant total current at mouth of 290 km estuary due to combined remote + local forcing from wind stress of 0.1 Pa varying over direction θ . $\theta = 0$ is along-estuary, $\theta = 20^\circ$ is directly along-shore: a) case for fixed $\alpha = 1.8e-4$. b) case for decreasing α .

Figure 4.19. Freshwater flux estimates from mooring time series of salinity and along-shore velocity (blue); volume flux and Bay entrance salinity (red) lagged 42 hours; and salinity contoured from CTD transects plus observed along-coast propagation speeds (green).

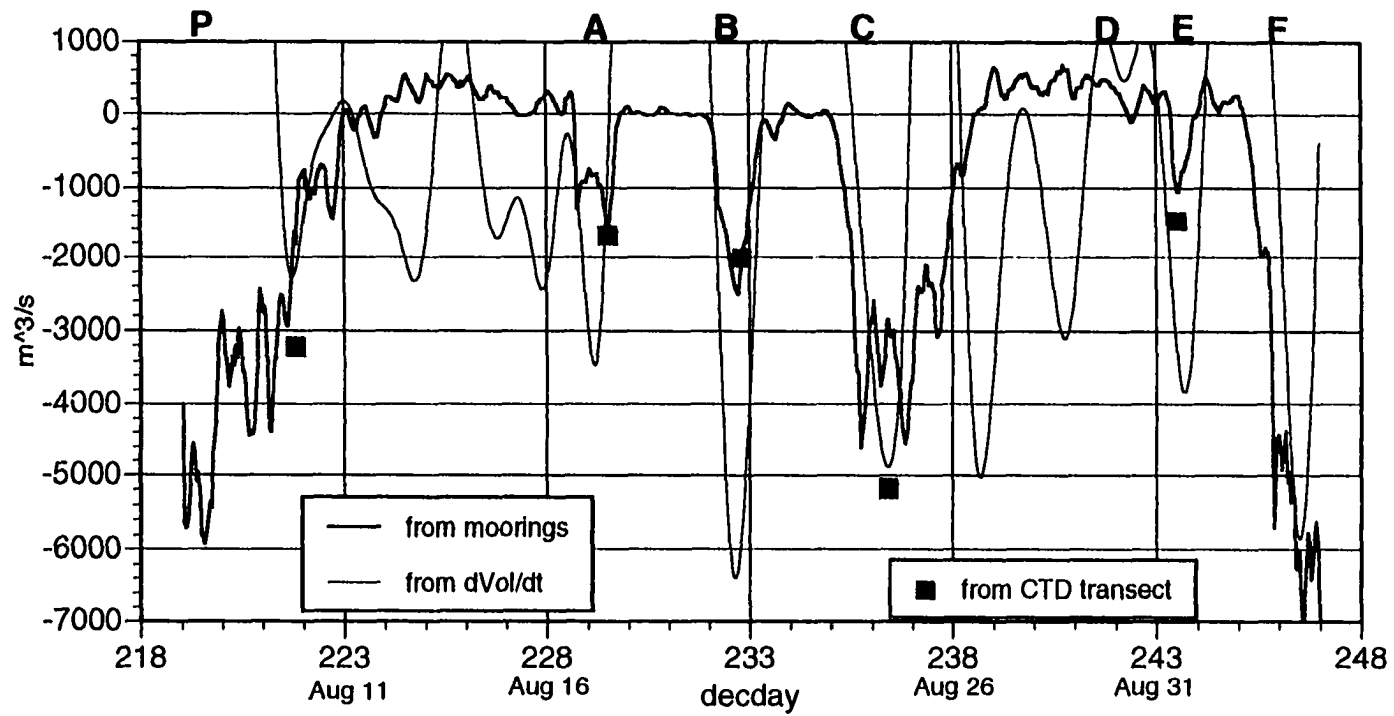


Figure 4.19. Freshwater flux estimates from mooring time series of salinity and alongshore velocity (blue) ; volume flux and Bay mouth salinity (red) lagged 42 hours; and salinity contoured from CTD transects and observed alongcoast propagation speeds (green).

Chapter 5. Plume Dispersal

The outflow from the Chesapeake Bay arrived along the North Carolina coast as distinct intermittent intrusions traveling as rotationally-trapped gravity currents. After the onset of upwelling winds, the nearshore salinities rose simultaneously all along the coast, indicating that the plume had moved offshore. The low salinity intrusion detached from the coast and formed a shallow lens floating over the ambient shelf water, which dissipated in 1 to 2 days. The lens was rarely observed to re-establish contact with the coast before considerable dilution takes place. Measurements from both the moorings and the shipboard surface mapping system show offshore motion occurring at speeds greater than 20 cm/s under very mild upwelling conditions. The theoretical response to this wind forcing is explored: Ekman dynamics in the shallow waters of the inner shelf are strongly affected by the local depth and strength of stratification. Along-shore wind stress τ_y acting on the portion of the plume occupying the entire water column, and therefore subject to bottom friction, generates more along-shore flow than cross-shore. However, where the plume is separated from the ambient shelf water by an intense pycnocline, τ_y forcing will be completely converted to across-shelf movement in the steady state. Deformation of the plume with elongation of the stratification-limited portion is expected and was observed. Additional mechanisms that aid the offshore movement of the plume, such as tides, density gradients and inertial motions are considered.

5.1 Offshore Movement of Buoyant Plumes : Background

The initial configuration of a low salinity intrusion is trapped against the coast by the Coriolis force due to its along-shore flow. What are the mechanisms that can cause the plume to spread away from the coast and mix with the offshore water? It is then that the plume delivers to the shelf at large the remainder of its lower salinity, along with any estuarine-derived biota, nutrients or possible contaminants it may contain. As was seen for the analysis of the along-shore propagation in chapter 3, the dispersal behavior of the intrusions will group into two dynamical regimes, determined by whether the plumes are in contact with the bottom, or are vertically delineated by stratification.

In the absence of wind stress, a surface trapped plume achieves and maintains geostrophic equilibrium in the cross-shore dimension, with the plume width on the order of the internal Rossby radius. The plumes that occupy the entire water column have been shown to be subject to continued widening due to the offshore advection of the fresher water by deflection of the along-shore flow in the bottom Ekman. An analysis of the non-linear effects of this density advection on the velocity led to the proposal by Chapman and Lentz (1994) that an equilibrium state could be reached after the plume front has moved offshore to the critical isobath depth where the geostrophically-balanced shear in the along-shore flow produces a change in sign in the cross-shore flow within the bottom boundary layer. However, in the analysis of Chapman and Lentz, it took a substantial period of time to reach this trapped equilibrium state; much longer than the synoptic meteorological time scale over which The Middle Atlantic Bight experiences large variation in the wind forcing. Therefore

stable plume widths for surface-to-bottom plumes are not expected due to bottom boundary-layer trapping. Garvine (1996) suggested that a stable frontal boundary could be achieved for frictionally controlled plumes when downwelling wind stress is present to balance this offshore flow.

The onset of upwelling winds can produce offshore advection in the upper water column, forcing the more buoyant plume water to detach from the bed and spread away from the coast, as modeled numerically by Chao (1987, 1988), who concluded that plume movement was dominantly controlled by Ekman drift. However, other researchers have observed that more stratified plumes travel largely in the direction of the wind stress (Stumpf et al., 1993).

An alternate approach involves the treatment of the wind as a momentum impulse into a geostrophically controlled frontal adjustment process. This model was developed analytically by Csanady (1978b) building on earlier investigations of two-layer coastal upwelling dynamics (Csanady, 1977, Cushman-Roisin, 1985). These models identify the minimum upwelling wind impulse needed to cause the pycnocline to surface on the inshore edge. This creates a detached lens of fresher water – a situation frequently observed in the CoOP data. The momentum impulse approach was extended by Ou (1984) in a numerical implementation that allowed consideration of the non-linear effects of larger pycnocline displacements. His results highlighted the asymmetry of the response in frontal movement to along-shore wind stress of different signs: downwelling impulses produce a deformation of the offshore front which can relax back to its original location; however upwelling causes an irreversible loss of freshwater from the coastal zone.

The process of offshore transport of coastal buoyancy over a shallow shelf has been extensively documented for observations from the South Atlantic Bight by Blanton and others (Blanton and Atkinson, 1983). They conclude that dispersal of low salinity water from the nearshore region occurs as a diffusive process during downwelling; whereas, during wind relaxation or reversal, the process involves advection of the surface waters. This advective process was elucidated by the results from a numerical model of that region developed by Kourafalou et al. (1996) where significant removal of fresher coastal water occurs as jetlike "streamers", or tongue-shaped regions of intensified offshore surface flow. It is such transient plume dispersal events of a largely advective nature on which I will focus within the CoOP observations.

5.2 Timing and Patterns of Offshore Movement

During the previous examination of the 5-m salinity time series displayed in Figure 3.2, the successive occurrence of decreases in salinity observed in the sensors deployed north to south was contrasted to the near-simultaneous increases in salinity at all along-coast locations. This suggested that the shoaling and movement away from shore occurred in a two-dimensional manner, with little along-shore variation.

5.2.1 Offshore Movement: Moored Salinity Time Series

In Figure 5.1 the upper salinity time series from the cross-shore array of moorings at the central line of Duck are presented for part of the

example time period from Figure 3.2, with the plume events labeled as before. Concurrent wind and coastal sea level measurements are shown in the upper panel. Again the simultaneous decreases at the pier and the 13-m mooring (1.5 km offshore) are noted, both being within the domain of the plume in its coastal configuration. The time lags in salinity decreases are seen in a cross-shore sense, with the outer edge of the plume encompassing the 20-m mooring (5.3 km offshore) a half-day or more after its arrival at the pier. The freshest water is seen at this location after the salinities inshore have risen, indicating that the plume has detached from the coast. When the plume water reaches the 25-m mooring (17 km offshore), between 1/2 to 1 1/2 days after it separates from the coast, the freshness is considerably diluted, indicating that mixing has occurred. During the continued period of northward wind stress, the salinities close to the coast are higher than the surface waters offshore, as shelf water under the plume is upwelled in the nearshore zone.

The time lag of 5 or 6 hours between when the salinity rises at the pier and at the 13-m mooring could be due both to the shoaling of the halocline as the spreading plume thins (the pier sensor is 2.5m deeper than the surface sensor on the 13-m mooring); and also to offshore movement of an upwelled halocline now defining the inshore edge of a detached plume. Estimates of cross-shore plume translation speeds were estimated using several approaches: the time between the minimum surface salinities observed at each mooring (going cross-shore) gave average speeds over time intervals of a half-day or more. When a CTD transect was available, the cross-shore salinity gradient could be combined with the temporal salinity gradient at the 20-m mooring to infer a plume translation rate. These speeds are presented in Table 5.1 along with the

prevailing wind conditions. The failure of the surface portion of the 20-m mooring in September and then the 13-m mooring in October limit the cross-shelf information for the autumn intrusions.

Plume Event	decimal day	speed (moorings or dS/dt) (cm/s)	over interval (hours)	speed from surface fronts (cms)	Along Shore wind (Pa)	Cross Shore wind (Pa)
A (T30)	229.46	15	3		0.03	0.00
A ->20m	229.53	19	5.5		0.08	-0.02
A ->25m	229.89	28	11.5		0.10	0.00
B (T45)	232.95	31	3	23	0.04	0.00
B ->20m	232.96	26	5	37	0.05	0.02
B (T40)	233.13	21	1	55	0.06	0.04
B ->25m	233.19	46	5		0.04	0.04
C (nearshore)	238.21	16	1		0.02	0.00
C ->20m	238.26	35	3		0.01	-0.00
C ->25m	239.39	12	27		0.00	0.00
E (nearshore)	244.17	12	2		0.02	0.02
E ->20m	244.21	11	10		0.02	0.02
E ->25m	244.80	23	14		0.00	0.01
F ->25m	249.70	14	32		0.01	0.03
H->25m	266.00	10	41		0.01	0.02
I ->25m	275.04	25	17		0.04	0.05
J (T40 @m25)	282.70	30	3		0.01	0.00
L (LN5)	291.90	22	2	mean of	0.01	0.00
L ->25m	292.78	20	17	16	0.02	0.02
M (T35)	296.00	13	3		0.03	0.00
M->25m	297.08	14	32		0.01	0.01
N (T40 @m25)	303.59	14	4		0.00	-0.01

Table 5.1

Speed of across-shore movement of low salinity plume based on minima or temporal gradient in salinity records from the moorings (column 3) and on observation of the location of the high gradient region in the underway surface salinity system (column 5).

The fresh water appears to move offshore at speeds larger than those commonly observed for cross-shore velocities on the inner shelf, with the estimates in column 3 averaging 21 cm/s. The cross-shore currents recorded during the entire field experiment at the 20-m mooring exceeded 15 cm/s less than 4% of the time. During these times when offshore movement of the plume was observed, the cross-shore component of velocity measured at 4.2 m depth at the 20-m mooring often do not agree with the translation speed estimates, being much smaller (or even directed onshore). This implies very high shear in the uppermost meters of the water column, a condition that was recorded during an anchor station on 26 August, as Event C moved offshore (Figure 5.2). The plume water is in the top 4 meters and velocities at 2m depth are double those at 4m. The ADCP velocities in Figure 3.4 also show high near-surface shear at the outer edge of the plume, with the cross-shore component reversing sign at 5m depth in Transect 50 (panel A).

The effective wind stress components at the time, computed using a surface drag coefficient from the bulk formulation of Large and Pond (1981), are shown in the two rightmost columns. Nearly all separations of the plume from the shore occur at times of northerly-directed wind stress (positive values in column 6), fitting the upwelling-driven proposal. In general, the near-shore salinities rise about 7 or 8 hours after the wind has turned northward. The observed stress is fairly mild, corresponding to wind speeds generally less than 6 m/s. The offshore movement of the plume is almost always aided by positive (offshore-directed) across-shore wind stress (column 7). The rise of inshore salinities occurs during falling coastal sea level for events (e.g. plume 'C') which are characterized by

downwelling and coastal setup, but the relationship to sea level variation is not noticeable for the offshore movement of the other intrusions.

5.2.2 Offshore Movement: Shipboard Salinity Observations

To validate the offshore speed estimates from the mooring records, several events are examined where the ship repeatedly surveyed a plume during its movement away from the coast. One such event was 'B' in Figure 5.1, for which the vertical cross section of salinity was shown previously in chapter 3 (Figure 3.4). This small-volume intrusion was always underlain by a strong pycnocline, and was seen to spread out from its coastal configuration (panel A, Figure 3.4) to a thin, elongated plume (panel B) which then separated from the shore to form a lens (panel C). The surface expression of the outer edge of the plume was observed as a high gradient region in salinity recorded by the shipboard underway mapping system. The cross-shore profiles of surface salinity are shown in Figure 5.3 for seven successive transects across the inner shelf, along with the cruise track. The front remained sharp, with salinity rising over 3.5 psu in less than 2 km, as it translated offshore. An interesting effect was the increasing freshness at the inshore side of the front. This tendency of the freshest water to gather at the outer edge of the spreading plume was noted in the vertical cross sections (Figure 3.4). It suggests that the very surface waters moved offshore most rapidly, consistent with the high near-surface shears noted in the previous section. Offshore translation speeds estimated from pairs of these surface frontal crossings are shown

in the fifth column of Table 5.1, and are consistent with the estimates based on the mooring observations.

Another plume that was well sampled by ship surveys occurred in mid-October and displayed a different initial configuration. Event L traveled down the coast under moderate winds towards the south, was pushed against the coast and deepened to contact the bottom as seen in a salinity section across the central line (Figure 5.4, panel A). Six hours later a survey profiled across the plume 20 km upstream (panel B). The winds at this time were light towards the northeast, and the plume has doubled its offshore extent. Sixteen hours later the central line was crossed again and the low salinity water was stretched out to over 15 km offshore and occupied only the very surface waters (panel C). Surface salinity traces (Figure 5.5) show the same fast offshore movement of the front as observed during the August event, but with evidence of increased mixing occurring. The salinity contrast across the front diminished from over 4 psu to less than 0.5 psu. In spite of extensive mixing, the sharpness of the front was maintained, implying, as above, that the very surface (freshest) water was supplied preferentially to the frontal region due to vertically sheared cross-shore flow within plume layer. The speed estimate based on frontal position matches reasonably well with the ones from the moorings (Table 5.1).

The individual speed estimates from these successive crossings show a rapid acceleration, then slowing over a time frame of less than a day (Figure 5.6), suggesting that processes such as tides or inertial oscillations may play a role in initially separating the low salinity water from the coast. The possibility of along-shore variation in the form of meanders of the front complicates the small scale analysis. However

estimates from repeated crossing of the central line allow us to be confident of the general trends.

5.2.3) Offshore Movement: Overall Statistics

Figure 5.7a extends the plot of the relationship between all observed surface salinity fronts and the along-shore wind seen previously in Figure 3.8b, by including those fronts determined to be the outer edge of a detached lens of plume water. There is a dramatic increase in width associated with positive wind stress. The position of the front observed during upwelling winds (defined by the mean of previous 6 hours of along-shore wind being > 0) averages 12.9 km offshore compared with a width of 7.1 km during winds towards the south. A comparison of frontal position with the cross-shore component of the wind (Figure 5.7b) reveals a less strong relationship over all, although separated plumes are found almost exclusively with offshore wind stress. Since the wind components are themselves correlated (section 3.3), it is difficult to determine if these are evidence of direct frictional cross-shore wind forcing or related to times of enhanced along-shore stress.

5.3. Theory for wind-driven offshore movement of coastal surface waters

The CoOP observations show that a rapid offshore movement of the low-salinity water always occurs after the local winds have turned northward. The magnitude of the winds is moderate: not usually greater than 7 or 8 m/s, and often less than 5 or 6 m/s (Table 5.1). The wind has generally been northward for 8 to 12 hours when the low salinity water is

seen to move offshore. Given the constrained nature of cross-shelf flows very near to the coast, how are we to understand the forcings and responses that bring about this movement? The short time periods over which the offshore translation were estimated (less than 12 hours on average) indicates that short time scale motions such as tidal flow as well as the time-varying aspects of wind-driven flow should perhaps be considered, rather than just the steady circulation patterns. To separate the effects, each mechanism can be examined theoretically to estimate the magnitude of its expected contribution. The inner shelf environment, with its shallow depths and proximity to the coast, is controlled strongly by the presence of these boundaries, yet our intuition of the behavior of each mechanism can be enhanced by reviewing simplified analytical solutions which may temporarily set aside some of these constraints.

5.3.1. Response to along-shore winds: Shortest time scales:

When the wind begins to blow upon the water, the initial acceleration is of the surface water in the direction of the wind. Over time, the response evolves such that the frictional layer deepens and the cross-wind component grows. The localized time-evolving solution, illustrated in Figure 5.8, is derived here from Fredholm's equations (Ekman, 1905) for a wind stress of $\tau_y = 0.5$ Pa where a constant vertical eddy viscosity is assumed. For the first several hours, the flow is contained above the Ekman layer depth, $D_{ek} = \sqrt{\frac{2A_v}{f}}$ where A_v is the vertical eddy viscosity; and f the Coriolis parameter. After six hours have passed, the cross-wind component has grown to be as large as the component in the direction of the wind, approaching the familiar deep-water steady Ekman solution

where the surface flow is 45° to the right of the wind. However, by this time, the wind-driven flow has deepened below the surface layer, so that the local bottom boundary condition on the flow will begin to control its behavior.

Since the inner shelf here is quite shallow, the total water depth, when the water column is homogeneous, is usually less than the Ekman layer thickness D_{ek} . In this case, the requirement that the flow go to zero at the bottom imposes a different distribution of the resultant motion, with nearly all of the flow remaining in the direction of the wind.

However, the presence of the plume, where it is not in contact with the bottom, imposes a stratification across some portion of the inner shelf that strongly affects the local response to the wind. The top two panels of Figure 5.4 are clear examples of how the cross-shore configuration of the plume can separate the inner shelf into distinctly homogeneous and stratified regions. Within the stratified region, the surface layer is insulated from bottom effects by the extremely diminished vertical eddy viscosity in the pycnocline. This results in depth layer of no stress. The solution with a no stress bottom boundary condition results in the total Ekman transport $U_{ek} = \frac{u_{*s}^2}{f}$, for $u_{*s}^2 = \frac{\tau_y}{\rho}$, confined above the pycnocline and flowing perpendicular to the wind direction. Figure 5.9 illustrates an example cross-shelf transect where the flow patterns within the stratified portion of the plume contrasts sharply with the circulation occurring elsewhere on the inner shelf. At this moment, a mild upwelling wind of 3 to 5 m/s has been blowing for about 18 hours: the shelf water offshore of the plume is flowing northward at 15 to 20 cm/s, while the surface plume waters are directed offshore at about the same speed. Note that at the

shallowest station, in depths less than 13 m, the flow is nearly all in the direction of the wind, indicating that it is largely depth-limited, in spite of some salinity gradients still measured in that profile.

The time-varying transport for the stratification-limited solution oscillates about U_{ek} over the inertial period, these oscillations being theoretically undamped due to the absence of bottom friction for this layer (Figure 5.10A). If the surface layer depth is on the order of D_{ek} there is very little depth variation in the cross-wind component velocities (Fig. 5.10B), which remain close to the average cross-shore velocity within the surface layer, $\frac{U_{ek}}{h_{pyc}}$. So the cross-wind velocities vary inversely with the thickness of the spreading plume, speeding up as the plume thins.

The flow pattern below the pycnocline is not specified by this 1-D solution. There is a velocity discontinuity at the pycnocline, since the frictional transfer of momentum has been 'short-circuited' by the presence of the frictionless ideal pycnocline. Of course, in this region close to the coast, any net cross-shore transport will set up a pressure gradient in a very short time, generating flow throughout the water column.

5.3.2 Response to along-shore winds: Intermediate time scales:

During the developing coastal setdown caused by the offshore transport in the surface Ekman layer, the cross-shelf pressure gradient accelerates compensating onshore flow. The pressure gradient-induced return flow is to 0th order evenly distributed throughout the water column with velocities of $\frac{U_{ek}}{h_{total}}$. This flow both opposes the offshore movement of the surface waters and creates onshore flow in the lower

layers. The return flow, or "adjustment drift", is in turn acted upon by the Coriolis force to generate an along-shore current that adjusts to a geostrophic equilibrium with the pressure gradient. The formation of this coastal jet was analyzed by Csanady (1982 p.90) for the two-layer case, which is analogous to the stratification-limited scenario discussed above, in that a strong pycnocline is postulated which confines the direct surface stress effects to the upper layer and allows separate responses in the top and bottom layers. This model attempts to describe the non-oscillatory portion of the flow patterns when the surface layer has achieved equilibrium with the wind stress, but before there is significant bottom friction induced by the developing along-shore flow in the bottom layer.

Csanady found the solutions for the top and bottom layer velocities to be for the cross-shore components:

$$u_{\text{top}}(x) = -\frac{u_{*s}^2}{f h_{\text{total}}} e^{\frac{-x}{R_{\text{ext}}}} - \frac{h_{\text{bot}}}{h_{\text{pyc}}} \frac{u_{*s}^2}{f h_{\text{total}}} e^{\frac{-x}{R_{\text{int}}}} + \frac{u_{*s}^2}{f h_{\text{pyc}}} \quad \text{eq(5.1.a)}$$

$$u_{\text{bot}}(x) = -\frac{u_{*s}^2}{f h_{\text{total}}} e^{\frac{-x}{R_{\text{ext}}}} + \frac{h_{\text{bot}}}{h_{\text{pyc}}} \frac{u_{*s}^2}{f h_{\text{total}}} e^{\frac{-x}{R_{\text{int}}}} \quad \text{eq(5.1.b)}$$

and for the along-shore components:

$$v_{\text{top}}(x) = \frac{u_{*s}^2 t}{h_{\text{total}}} e^{\frac{-x}{R_{\text{ext}}}} + \frac{h_{\text{bot}}}{h_{\text{pyc}}} \frac{u_{*s}^2 t}{h_{\text{total}}} e^{\frac{-x}{R_{\text{int}}}} \quad \text{eq(5.2.a)}$$

$$v_{\text{bot}}(x) = \frac{u_{*s}^2 t}{h_{\text{total}}} e^{\frac{-x}{R_{\text{ext}}}} - \frac{u_{*s}^2 t}{h_{\text{total}}} e^{\frac{-x}{R_{\text{int}}}} \quad \text{eq(5.2.b)}$$

The last term in the top layer cross-shore flow (eq 5.1a) can be recognized as the steady stratification-limited solution, $\frac{U_{ek}}{h_{\text{pyc}}}$, discussed in

the previous section, which in this model is approached far offshore (beyond the external Rossby radius R_{ext}). The first term in eq 5.1, which both layers have in common, represents the barotropic return flow mentioned above. The second terms, which are oppositely directed in the two layers, allow the total flow to adjust to zero towards the coast (over the internal Rossby radius R_{int}). The cross-shore flows resulting from a 0.05 Pa wind stress are illustrated in Figure 5.11A for a scenario where the pycnocline (with a typical density difference of 2.3σ) is located at 5m in a total water depth of 20 m, resulting in an internal Rossby radius of $R_{int}=3.2\text{km}$. By $2 * R_{int}$ offshore, the cross-shore velocity in the upper layer approaches the zero-order value suggested above of $\frac{U_{ek}}{h_{pyc}} - \frac{U_{ek}}{h_{total}}$.

The net cross-shore flow, which causes the sea surface setdown across the shelf, is quite small: less than 1 cm/s even for the case where the top and bottom layer depths are equal. The flow which effects the barotropic relaxation of previous coastal setup due to downwelling is the same magnitude, much too small to be an important contributor to the observed offshore translation of the plume water.

The along-shore velocities of this model (eq. 5.2) again share a barotropic term which is the portion of the along-shore current in balance with the developing barotropic pressure gradient generated by the surface elevation. This flow is in the direction of the wind and decays offshore over the width of the external Rossby radius. The second term represents the baroclinic flow in balance with the developing slope of the pycnocline which acts in the same direction as the barotropic part in the top layer, but opposes the barotropic flow in the bottom layer. These terms are important only over the width of the internal Rossby radius. Therefore, close to shore in a stratified system, in addition to the Ekman drift

discussed above, an along-shore wind generates along-shore flow that is sheared in the vertical. This along-shore current as modeled here, continues to increase linearly in time: in actuality, the developing bottom friction would soon become dynamically important, eventually balancing the surface stress. The time scale in which this was achieved on the inner shelf at Duck was in the range of 6 to 9 hours, based on the observed lags between the pressure or velocity measurements at the 20-m mooring and the along-shore wind forcing. Top and bottom layer along-shore flows representative of an along-shore wind of 0.05 Pa after seven hours are shown in Figure 5.11B. Note the level of negative shear in the along-shore current: near R_{int} offshore, the northward top layer velocities are over twice those in the lower layer.

The behavior of the flows closest to shore are not represented well by this simple model. The along-shore acceleration in the bottom layer has been achieved by Coriolis force acting on the bottom layer cross-shore flow. The assumption of small pycnocline displacement and of a flat bottom in this model cause the cross-shelf velocity in the bottom layer to drop rapidly to zero close to shore. For the case of a sloping bottom, $h_{bot} = s \cdot x$ (where a representative slope for the shelf inshore of the 20-m mooring is $s = 0.003$), an extension of this model (Csanady, 1977) shows that inflow in the bottom layer, required to match the rising pycnocline, forces an onshore velocity equal to the vertical velocity divided by the bottom slope, with a resulting increase in the lower-layer along-shore flow over the sloping portion of the bottom, and correspondingly, increased bottom friction.

Over the innermost portion of the sloping shoreface there would often be an unstratified water column, either because a deep plume had

intersected the bottom; or resulting after the separation of the plume from the coast. In this case the along-shore flow would approach the homogeneous solution, shown as x's in Figure 5.11B.

5.3.3 Response to along-shore winds: Frictional equilibrium time scales:

For times longer than 6 to 9 hours, a frictional balance should be achieved on the inner shelf between the surface and bottom stress. The along-shore current no longer accelerates: its Coriolis force completely balances the steady cross-shore pressure gradient. A bottom along-shore flow has been established, leading to a frictional bottom boundary layer whose net Ekman transport will be directed onshore. In classical deep-water solutions for fully-established upwelling, the surface frictional layer is separated by an inviscid interior region from the bottom frictional layer: the full Uek transport occurs in opposite directions within those boundary layers. In our inner shelf scenario, the pycnocline underlying the plume substitutes for the inviscid region, allowing oppositely directed balancing cross-flows to co-exist in a shallow water column. As with the surface Ekman solutions, modifying the boundary conditions for the bottom Ekman layer changes the distribution of flows, as illustrated in Figure 5.10C. The classical solution (shown in magenta) requires that the Ekman layer flow match the interior at the top of the boundary layer. In our inner shelf case, a level of no stress is imposed at some depth above the bottom before that can occur, resulting in increased cross-shore transport within the boundary layer (shown in red).

A deep plume over the shore-most portion of the inner shelf, where it fills the entire water column, would be subject to the zero flow condition at the bottom, and experience no cross-shore acceleration from an along-shore wind. In the cases where there is some stratification within the plume layer itself, the effective Ekman depth could be reduced to less than the water column depth. The response of this case, where the surface and bottom Ekman layers overlap and interact with each other, has been examined by Mitchum and Clarke (1986). Their "blocking" region of Ekman layer interaction, discussed as the region of water column depth variation between 0.2 and $2.5 \cdot D_{ek}$, could be in this case defined by the control that the plume's stratification exerts on D_{ek} . The shore-most profile in Figure 5.9 is an example of this intermediate region.

The above examination of the generation of cross-shore flow due to along-shore wind forcing, with the stratifying presence of the plume, shows that during the initial response, only small velocities should be reached in the region less than 1 to 2 internal Rossby radii within the coast; increasing to moderate velocities farther offshore. Where the plume reaches to the bottom in shallow water, almost no cross-shore current is generated. Figure 5.12 summarizes the approximate range of velocities calculated for a 6 m/s along shore wind acting over the inner shelf. This divergence in cross-shelf flows should lead to an elongation offshore of the stratified portion of the plume : a plume configured like those in Figure 5.4A or Figure 3.4A would be deformed as the portion not in contact with the bottom moved offshore more rapidly. As noted above, the velocities increase in the stratification-limited portion as the plume thins, since the unvarying Ekman transport is distributed through a smaller layer, increasing the elongation of the offshore thinning edge of

the plume. The evolution from panel A to B shown in Figure 5.4 may be an example of this process.

After the full along-shore response to the coastal setdown becomes established, offshore surface layer velocities are balanced by the shoreward flow within the bottom frictional layer. Then, the surface flow is no longer moderated by the pressure-driven return flow, increasing to the full steady $\frac{U_{ek}}{h_{pyc}}$ value. For the moderate winds observed ($\tau_y \sim 0.05$ Pa), this value starts to exceed 10 cm/s when the plume layer thins to less than 5m deep. When the overlying inertial oscillations are considered, as shown in Fig5.10A, the rate of offshore movement for this scenario reaches a maximum of over 20 cm/s, matching the average velocity from the observations in Table 5.1. (see Figure 5.12). Note that the timing of the maximum offshore velocity occurs between 8 to 10 hours after the onset of the wind -- the same time range that was observed in section 5.2.1. The importance role that inertial oscillations may play in plume separations can also be noted in Figure 5.13. Here the time-series of the amplitude of the complex-demodulated inertial frequency is shown along with the times of separations : the correspondance is particularly noticable in October.

5.3.4 Role of cross-shore winds:

In all cases discussed above, the cross-shore motion generated by along-shore wind was extremely small for the shoremost region: the area less than R_{int} from the coast, or in depths less than the plume thickness. The analysis above noted that the portion of the plume in contact with the

bottom will experience wind-driven flow aligned largely with the wind direction. In this case, the cross-shore component of the wind stress would be more effective at producing offshore transport. In over 80% of the examples, offshore winds were observed during the plume separations (column 7 in Table 5.1). Conversely, onshore winds were rarely recorded during these times.

Again, any offshore motion near the coast is opposed by the barotropic return flow due to the cross-shelf pressure gradient. Net cross-shore flows can occur where the wind-driven flow is sheared in the vertical, so there is an imbalance at that level with the essentially vertically-constant return flow driven by the pressure gradient body force. This is illustrated in Figure 5.14 for a 6m/s offshore wind, where the mismatch near the surface results in an offshore current of over 4 cm/s in the upper few meters. The actual vertical shape of the wind-driven flows will be determined by the vertical variation of the eddy viscosity, which heretofore has been assumed to be constant. A constant eddy viscosity produces a linearly sheared along-wind flow (as was seen in Figure 5.14). The use of a more realistic form of the eddy viscosity, such as the bilinear profile suggested by Madsen (1977), results in even more highly sheared flow near the surface in the direction of the wind. The velocities are still moderate, compared to the speeds seen in the stratification-limited cases discussed above, and confined to the upper few meters of the water column.

It is important to note that the wind stress levels used throughout this analysis have been based on the Large and Pond (1981) formulation for the surface drag coefficient $C_{ds} = 0.0011$, which was derived from open-ocean studies. Several studies have suggested that a larger C_{ds} is

appropriate in shallower water where short period, steeper waves predominate (Geernaert et al., 1987). The increase in C_d s is particularly enhanced for offshore winds due both to the increased turbulence from flow over land and also to the large wind-wave angle. A recent study using observations from Duck (Friedrichs and Wright, 1997) determined that the surface drag coefficient for offshore-directed winds could be four times larger than onshore winds. This alternative magnitude of cross-shore forcing is shown in Figure 5.14 where the surface current is now over 16 cm/s. This could make even a small offshore-component of the wind a significant contributor to the cross-shore flow of the near-shore water. The relationship between offshore wind strength (positive stress) and plume width (Figure 5.7b) does appear to be stronger than for the onshore winds. The shore-most (depth-limited) portion of the plume may be aided by the cross-shore wind component which move the surfacemost waters offshore, creating a newly stratified region. This strain-induced stratification then allows the along-shore wind effects that are pycnocline-limited to predominate.

5.4 Geostrophic Adjustment

In the previous sections the plume water mass has been treated as passive, being advected solely by the action of wind. But the defining characteristic of the coastal configuration of the plume is a strong cross-shore density gradient that will have an offshore-directed force of its own in the surface waters. Below the midpoint of the buoyant layer, the pressure gradient becomes directed onshore, making an cross-shore density forcing similar to the gravitational pattern in estuaries. However,

on the shelf, the gravitational circulation can be balanced by the Coriolis term of the sheared along-shore flow. This basic geostrophic balance is revealed by the “thermal wind” relationship, $f \frac{\partial v}{\partial z} = -\frac{g}{\rho} \frac{\partial \rho}{\partial x}$, which appears to be the dominant cross-shore balance in the plume’s domain, as shown in Figure 5.15. Close to 70% of the observed vertical shear in the alongshelf current is predicted by the measured cross-shelf density gradient in the upper part of the water column between the 13-m and 20-m moorings. This indicates that the geostrophy is still important on the inner shelf inspite its shallow depths. In Lentz et al. (1998) this thermal wind balance is shown to be important even in at the 8m tower.

As discussed in Chapter 3, when there is no wind forcing applied and the along-shore current is due solely to buoyancy, the density deficit $\partial\rho$ is distributed so that R_{int} defines the cross-shore width scale ∂x , and the along-shore velocity v is strongly positively sheared (with depth z considered as increasing downwards). Any reduction in this shear should result in an increase in ∂x (i.e. widening of the plume). This reduction in shear could come about in several ways: section 5.3 discussed several mechanisms whereby northward wind input negatively sheared along-shore velocities (especially note eq. 5.2 and Fig5.11B in section 5.3.2). In addition, the overall slowing of the southward baroclinic current, under the influence of bottom friction, would reduce this shear.

Csanady (1978b) developed a simple 2-layer analytic model of the geostrophic adjustment of a horizontal density front that initially reaches from the surface to the bottom. In the absence of any wind forcing, the width, as described before, scales with R_{int} : this equilibrium is illustrated in Figure 5.16, where the frontal half width a_p is found to be $a_p = 1.2R_{int}$.

An input of negative shear to the along-shore flow equivalent to the total wind stress $u_{*s}^2 t$ accelerating only the top layer is then envisioned. This vertical shear is equivalent to $v_{top}(x) - v_{bot}(x)$ in eq 5.2 (for $x < R_{int}$). During the subsequent geostrophic adjustment, the front will widen out, with the new half width a_I being found as the root of

$$\frac{a_I}{R_{int}} + \frac{u_{*s}^2 t}{C_{int} * h_{total}/2} - \coth\left(\frac{a_I}{R_{int}}\right) = 0 \quad (\text{eq. 5.3})$$

(Csanady, 1978b). The new position of the front between the two densities is illustrated in Figure 5.16 (dotted line) for a wind impulse of $u_{*s}^2 t$ equivalent to a 0.1 Pa wind blowing for 10 hours, using a density difference of 2.3 σ units in a total water depth of 16 m). The input of positive (upwelling-directed) wind stress causes the front to surface at a distance of over $2 * R_{int}$ offshore of its non-adjusted position. Conversely, the superposition of southward (negative) wind stress on the baroclinic flow will increase the vertical shear in the along-shore current, steepening the front and decreasing the frontal half width, as was shown in Figure 3.7c. When the southward wind ceases, a previously downwelled plume (such as shown in Figure 5.3A) will widen offshore as it relaxes back to the equilibrium state.

The geostrophically adjusted width of the low salinity water mass reached after a wind impulse duration of 10 hours is overlaid on Figure 5.7a for a range of wind stresses. Times of separation of the plume were observed at Duck following wind impulses of no more than $+1.8 \text{ m}^2/\text{s}$ (or about 10 hours of a wind stress of 0.05 Pa). Again considering a plume with a density difference of 2.3 sigma units, occupying half of a 16 m water column, the geostrophic adjustment model predicts that the front location will move only 2 km offshore in response to such an impulse. As can be

seen in Figure 5.7a, the observed widths are far larger for mild upwelling wind stress than the theoretical geostrophically adjusted widths.

The geostrophic adjustment model allows the computation of the minimum wind impulse necessary to cause the separation of the lighter water from the coast and the formation of a surface lens. By volumetric arguments Csanady (1978b) found that the minimum impulse is the root of

$$\frac{I_{\min}}{C_{\text{int}} * h_{\text{total}}/2} - \tanh\left(\frac{I_{\min}}{C_{\text{int}} * h_{\text{total}}/2}\right) + \frac{a_f}{R_{\text{int}}} = 0 \quad (\text{eq. 5.9})$$

when the unforced surface-to-bottom front intersected the coastline at h_{total} . In this case the solution implies that $I_{\min} > 8$, or a 0.05 Pa wind blowing for almost two days, would be required to cause the separation. Clearly, the CoOP observations indicate that much less forcing is required. The use of the wind impulse approach, which allows the analytic solution, neglects the thinning of the top layer over the time that the wind is blowing, and also distributes the velocities evenly over the top layer. Previous discussions in section 5.3 showed that the elongation and thinning of the plume layer by the higher velocities at the very surface and in the stratified portions is an essential part of the rapid offshore movement.

5.5 Tides

Given the short time periods over which these low salinity lenses have been observed to form, one might investigate the role that tidal flows could play. A harmonic analysis (using a least-squares technique) of the 3 month time series of currents from the moorings separates the contribution of the astronomical tidal constituents to the flow on the

inner shelf at Duck. The amplitude and phase of the largest 3 constituents are reported in Table 5.2 for the upper sensor from the outer two moorings, and confirm that the local tides are dominantly semi-diurnal. The tides in this region are increasingly damped towards the shore and towards the bottom. A more complete analysis of the tides during this study was described by Shay et al. (1997).

The resulting across-shore tidal flow due to these combined constituents could reach an maximum amplitude of slightly over 6 cm/s within the offshore region of the plume, with this amplitude decreasing towards the coast. The phase timing was examined for many of the plume separation periods. In some cases, offshore movement occurred during ebb tide, as might be expected in a straightforward way (see examples in Figure 5.6). However, more frequently, a rising tide was associated with the accelerating offshore phase. Given the importance of the location of the vertical stratification within the water column to the response to wind forcing, the role that the tides play in raising or lowering the pycnocline may be their primary contribution to the timing of the plume separations.

Tidal Const.	Period (hours)	Cross-shore Amp (cm/s)	Cross-shore Phase (hrs)	Along-shore Amp (cm/s)	Along-shore Phase (hrs)
25 - m					
M 2	12.42	4.27	3.39	5.31	-1.32
S 2	12.00	0.47	4.09	1.00	-0.52
K 1	23.93	2.48	4.19	1.79	-0.52
20 - m					
M 2	12.42	2.04	3.06	4.26	-2.08
S 2	12.00	0.66	3.93	1.28	-0.97
K 1	23.93	1.32	2.95	1.60	2.26

Table 5.2

Amplitudes and phases of tidal currents at the 4m current meter on the 25-m and 20-m moorings.

5.6. Summary

After determining that observations from the CoOP field program regularly revealed offshore movement of the plume waters at rates of 20 cm/s, a number of possible causal mechanisms were considered. An examination of the theoretical response of shallow coastal water reveals that offshore surface movement, as a response to moderate wind forcing, will be constrained, both by bottom friction and the coastal presence, to speeds of less than 5 cm/s. A similar magnitude was seen from the cross-shore component of the tides, as well as the additional offshore movement caused by the geostrophic adjustment of a density front in response to the input of negative along-shore shear (Figure 5.12).

Faster speeds were computed only when strong stratification, such as that provided by the halocline underlying the plume, traps all the wind momentum in the surface layer. During an intermediate time period, while the coastal jet is growing, the offshore flow speeds are reduced by the pressure-gradient return flow (Figure 5.12, green bar). However, once frictional equilibrium has been established, theoretically the entire Ekman transport can occur in the surface layer. As this plume thins, the speeds increase inversely with the depth of the layer (compare purple bar with orange in Figure 5.12). The large magnitude of the observed offshore movements can only be explained by Ekman transport in these highly-stratified, thinning plume layers. Eventually, the increasing speed and thinning must lead to mixing (note Figure 5.5) and a breakdown of the pycnocline. The offshore lenses observed a day or two after the onset of upwelling exhibited a salinity contrast of less than 1 psu and generally were mixed away prior to the next downwelling event.

The contribution of the inertial cycle overlying the steady values computed above, is highlighted by the observed timing of the plume separations, which were noted to occur between 8 to 12 hours after the onset of northward winds: the peak inertial overshoot (yellow bar in Figure 5.12) occurs after 10 hours.

Figure 5.1 Lower panel : near-surface salinities at 4 moorings across the central line during the same time period as Figure 3.4.
Upper panel : wind components with waterlevel overlaid.

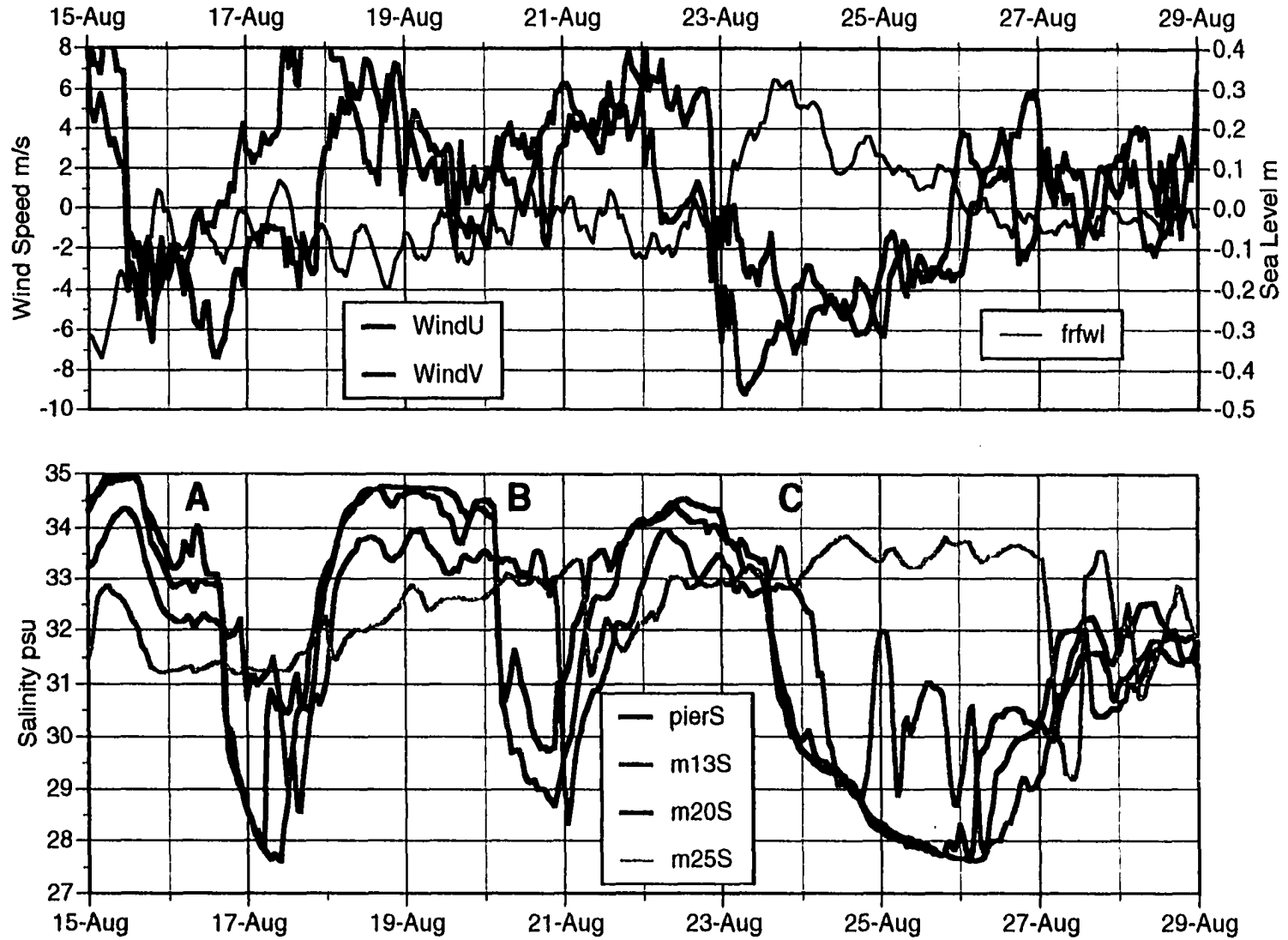


Figure 5.1 Upper water salinities at 4 moorings across the central line during same time period as Figure 3.2 (lower panel); and wind components with waterlevel overlain (upper panel).

Figure 5.2. Salinity and cross-shore velocity profiles from CTD and ADCP measurements taken during anchor station 4, 00:30 to 10:00 on August 26.

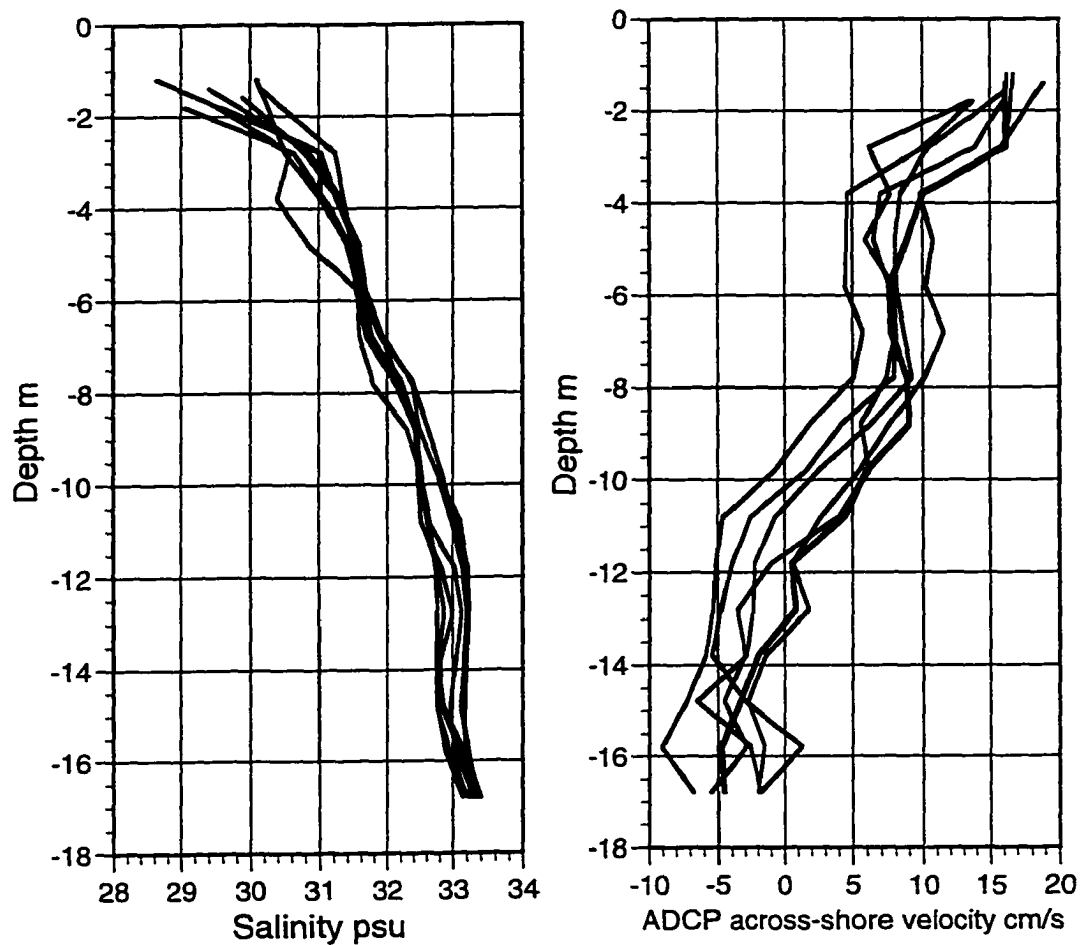


Figure 5.2 Salinity and across-shore velocity profiles from CTD and detided ADCP measurements taken during anchor station 4, 00:30 to 10:00 26 August, 1994.

Figure 5.3. Upper panel: Surface salinity traces from shipboard underway mapping system from successive crossings of the inner shelf made 20-21 August, 1994. Lower panel: Ship Track.

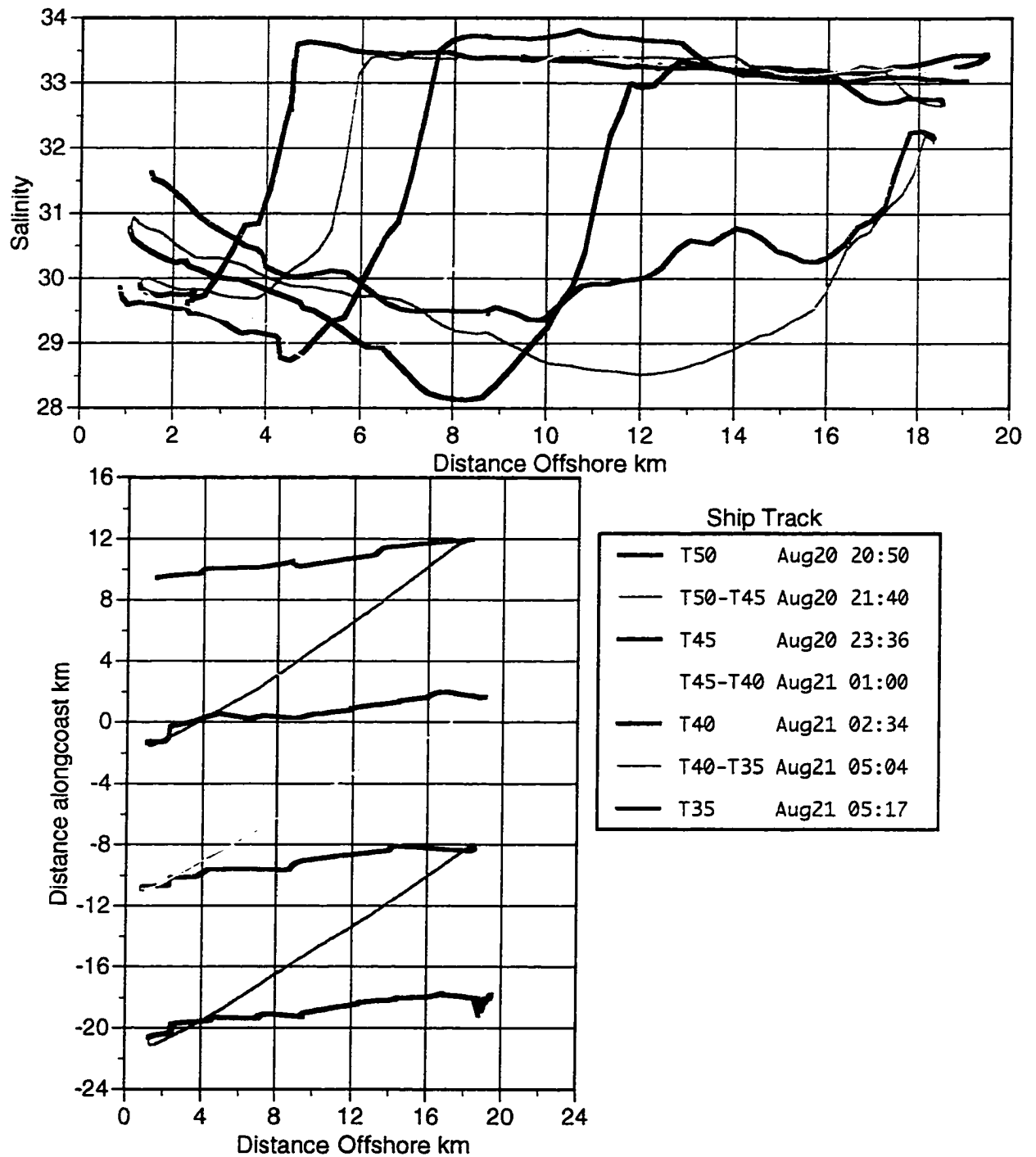


Figure 5.3. Upper panel: Surface salinity traces from shipboard underway mapping system from successive crossings of the inner shelf. Lower panel: Ship Track.

Figure 5.4 Salinity Transects from LN5 and SSB2, Oct 18 and 19.

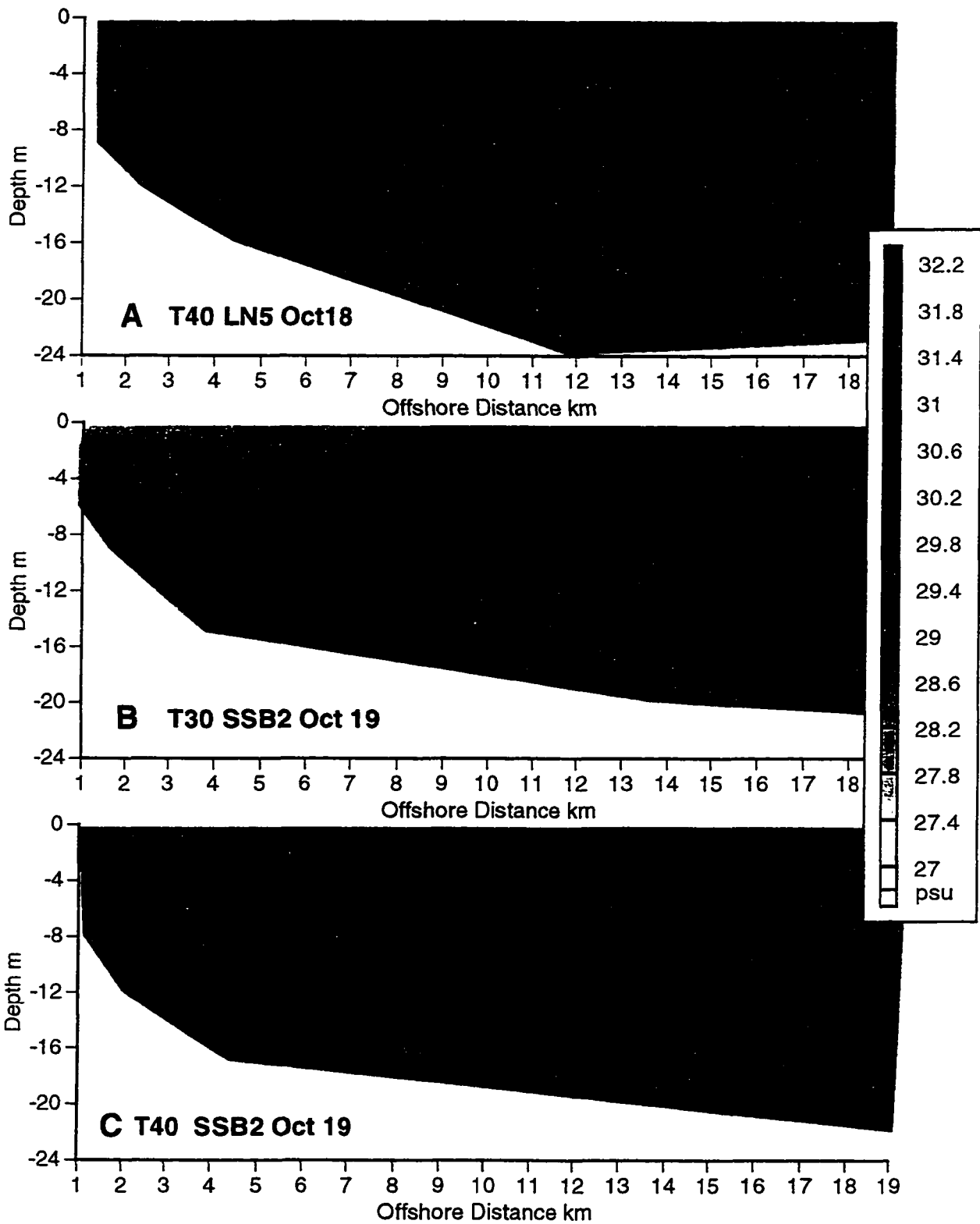


Figure 5.4 Salinity Transects from Ln5 and SB2, October 18 and 19, 1994.

Figure 5.5 Surface salinity from shipboard underway mapping system taken on successive across-shelf transects taken October 18 and 19, 1994.

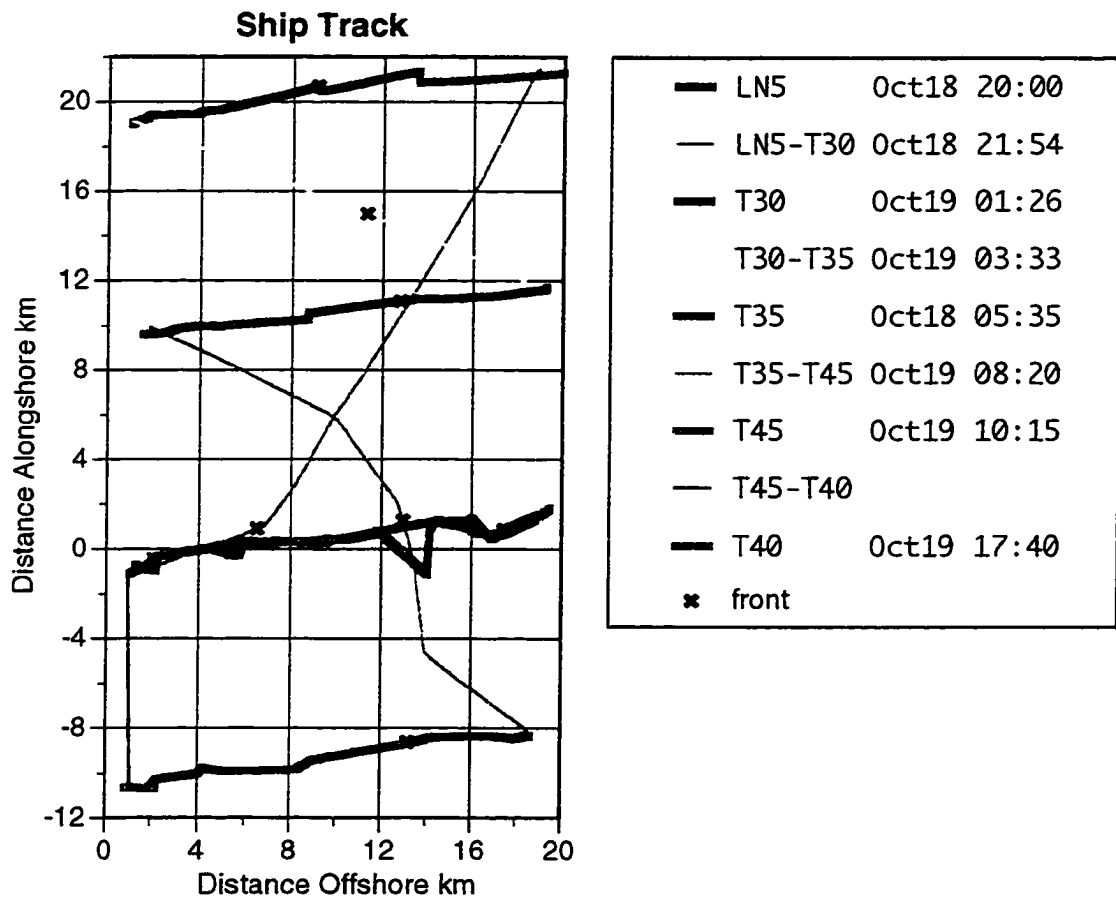
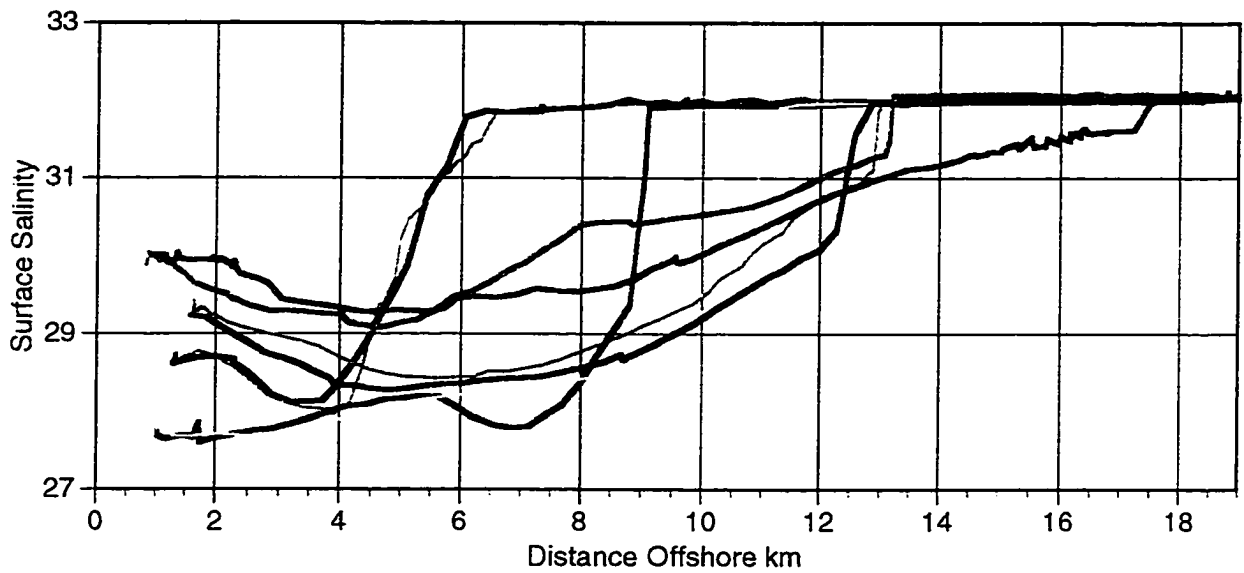


Figure 5.5 Surface salinity from shipboard underway mapping system taken on successive across-shore transects, October 18 and 19, 1994.

Figure 5.6. 20-21 August (upper panel) & 18-19 October (lower panel) offshore movement of salinity front speed estimates from shipboard underway mapping system. Diamonds indicate frontal speed estimates from mooring observations. Cyan line is calculated tides from section 5.5.

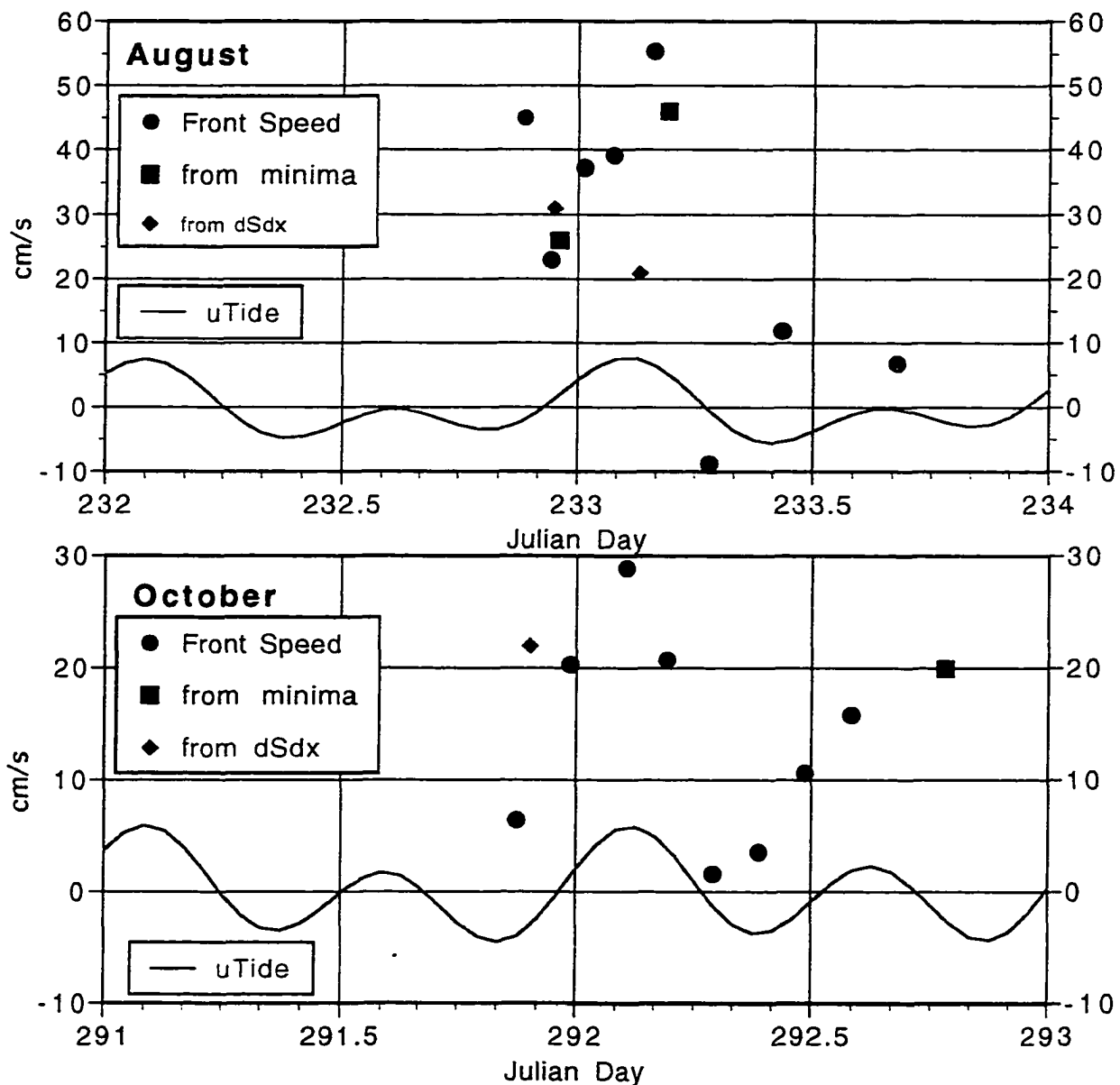


Figure 5.6. August 20-21 (upper panel) & October 18-19 (lower panel) offshore movement of salinity front. Speed estimates from shipboard underway system are dots. Diamonds indicate frontal speed estimates from mooring observations (section 5.2.1). Cyan line is cross-shore tidal current calculated as in section 5.5.

Figure 5.7. Offshore position of high-gradient region of salinity observed by shipboard underway surface mapping system versus a) recent along-shore wind stress and b) recent cross-shore wind stress.

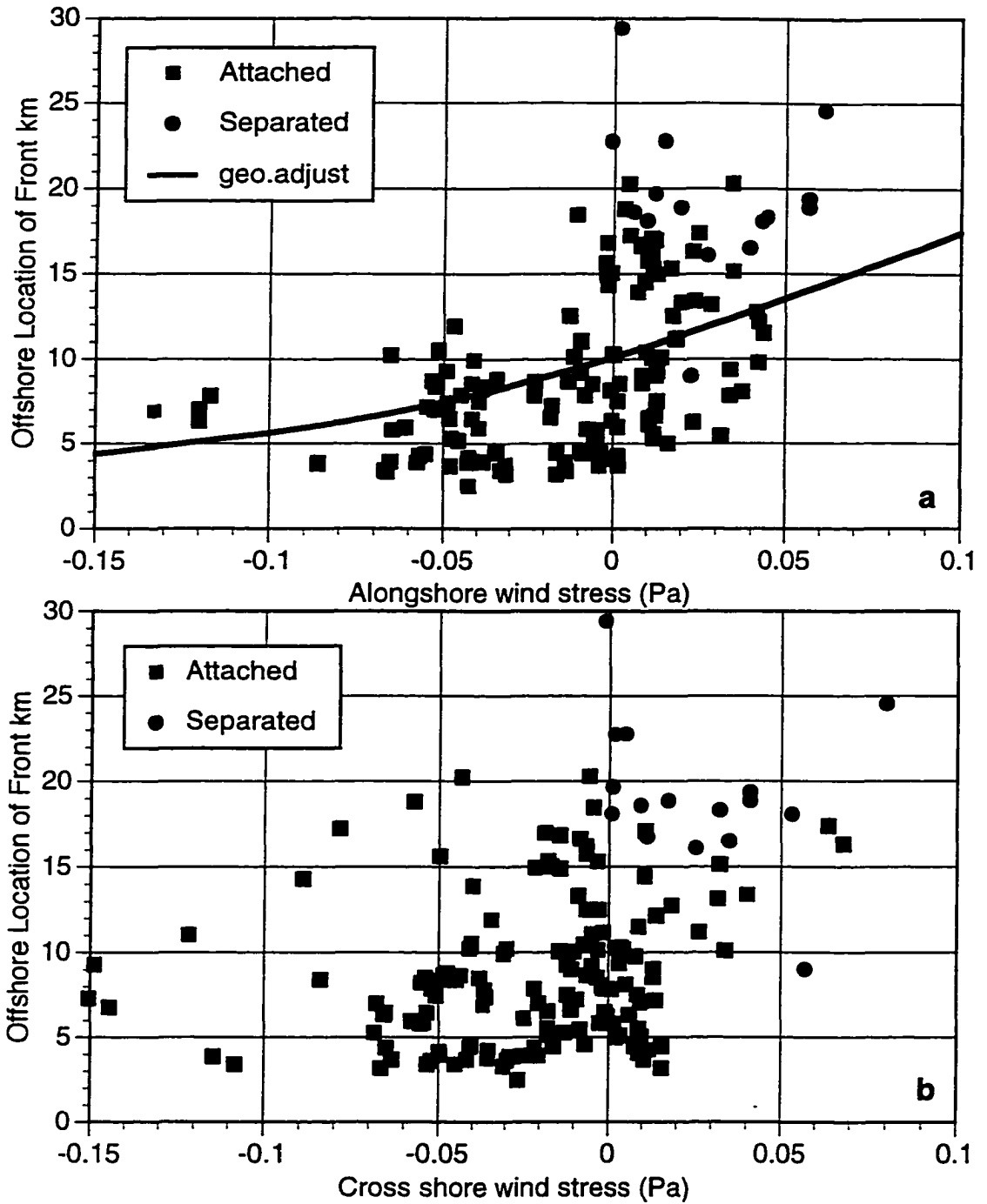


Figure 5.7. Offshore position of high-gradient region of salinity observed by shipboard underway surface mapping system a) *versus* recent alongshore wind stress and b) *versus* recent cross shore wind stress. Solid line in panel a is the theoretical width from the geostrophic adjustment model (section 5.3.6) for $\Delta\sigma=2.3$ following a wind impulse of 10 hours duration.

Figure 5.8. Time-evolving solution to along-shore wind (initial flow at time < 6 hours).

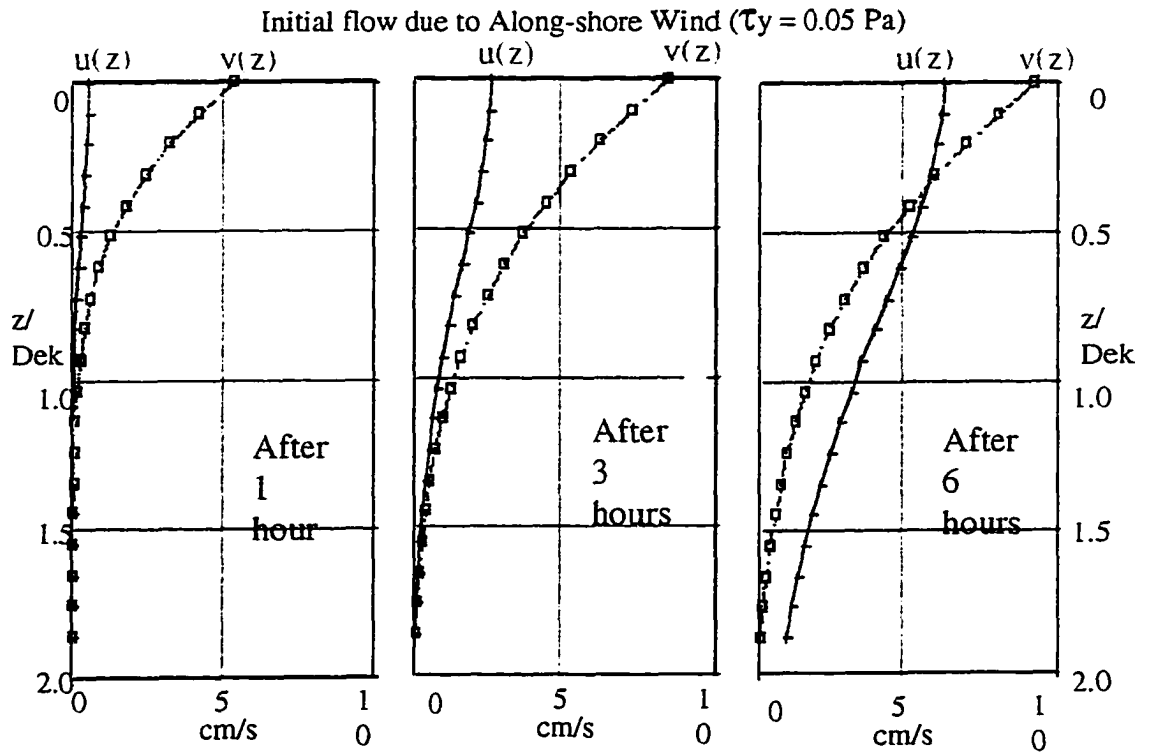


Fig 5.8 Time-evolving Ekman solution.

Figure 5.9. Salinity and ADCP velocities from transect 1 across central line, during mild upwelling winds on October 9-10. Color scale is salinity (psu). ADCP velocity vectors are oriented as map view.

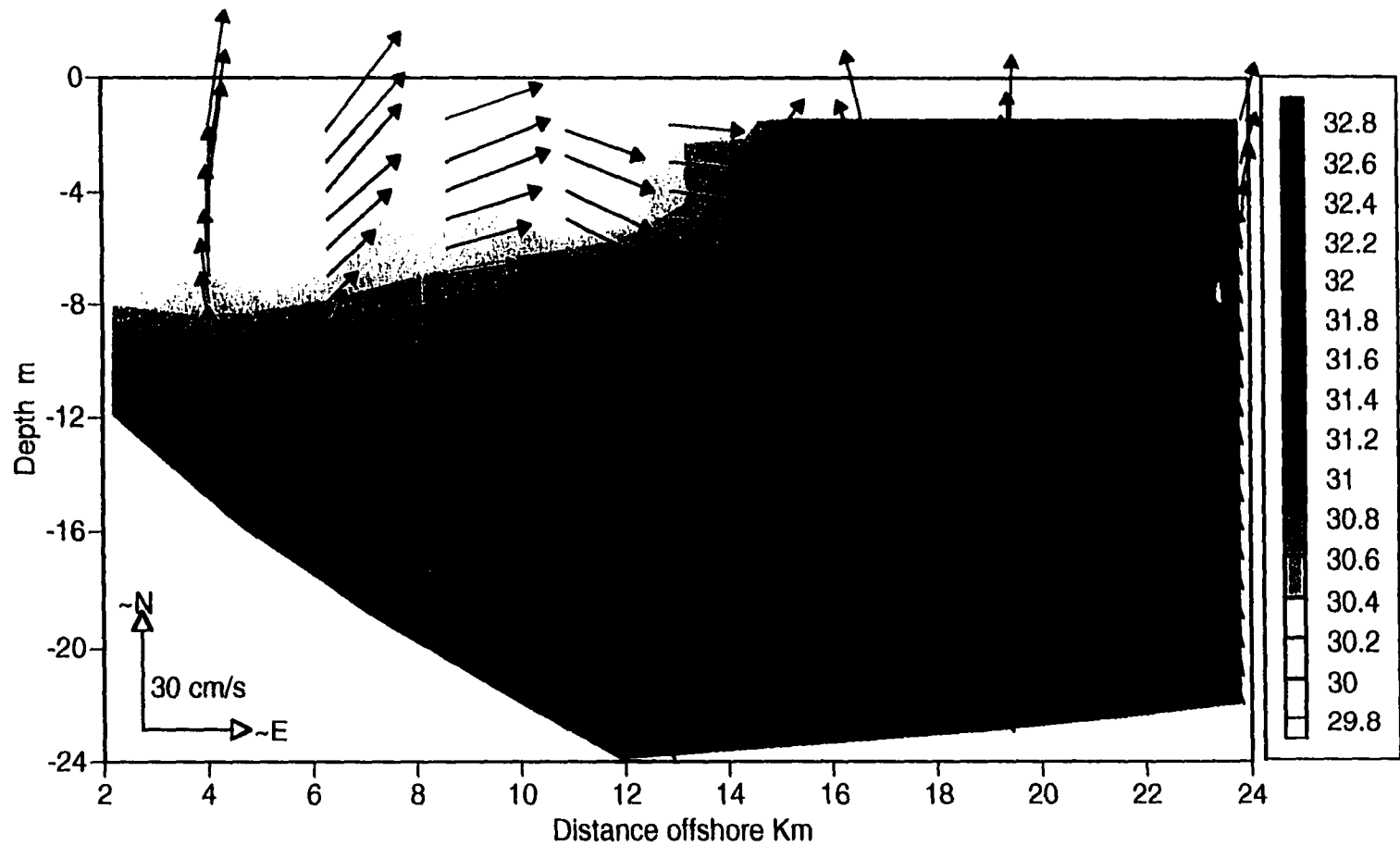


Figure 5.9 Transect Line 1 across central line on October 9-10 during mild upwelling wind. Color scale is salinity (psu). ADCP velocity arrows are plotted as map view (up = ~N (340°)).

Figure 5.10. a) Inertial oscillations in stratification-limited flow. b) steady stratification-limited flow. c) flow in bottom Ekman layer.

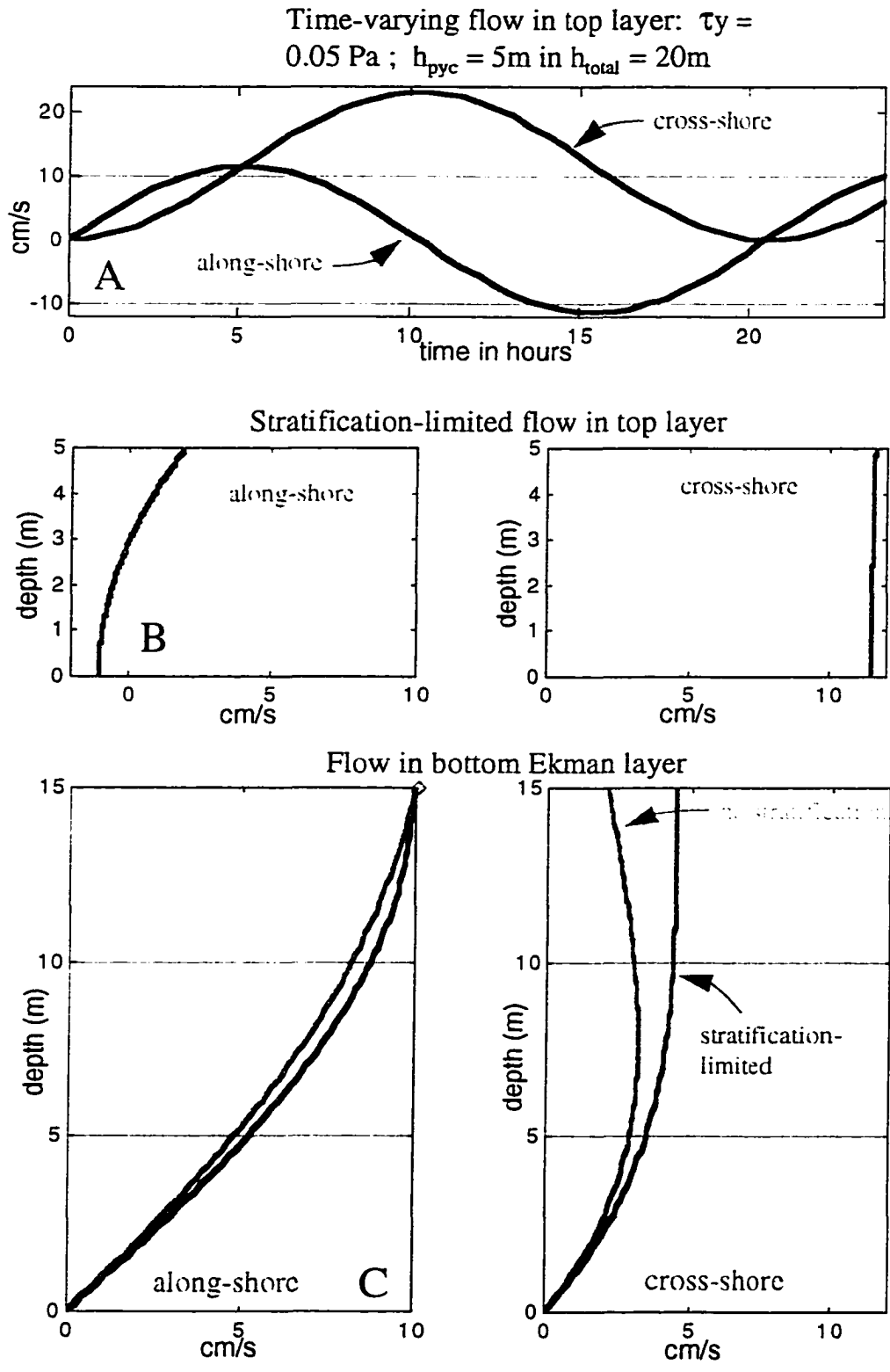


Fig 5.10 a) Inertial oscillations in stratification-limited flow. b) steady stratification-limited flow. c) flow in bottom Ekman layer

Figure 5.11. Two-layer coastal jet solution: a) cross-shore flows
b) along-shore flows.

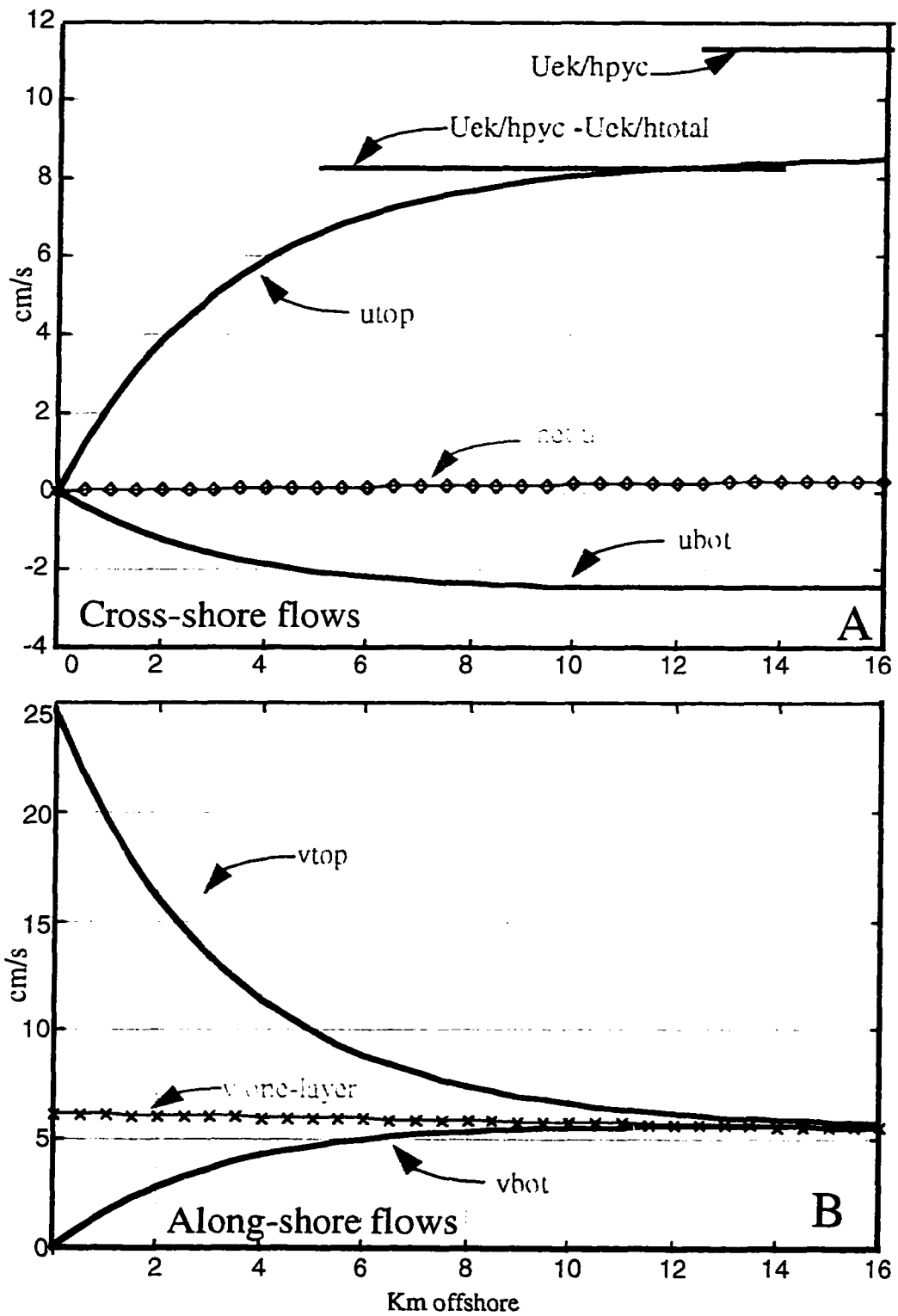


Fig 5.11 Two-layer coastal jet solution: A) cross-shore flows
 B) along-shore flows (after 7 hours of 0.05Pa wind stress)

Figure 5.12. Summary of theoretical offshore velocities.

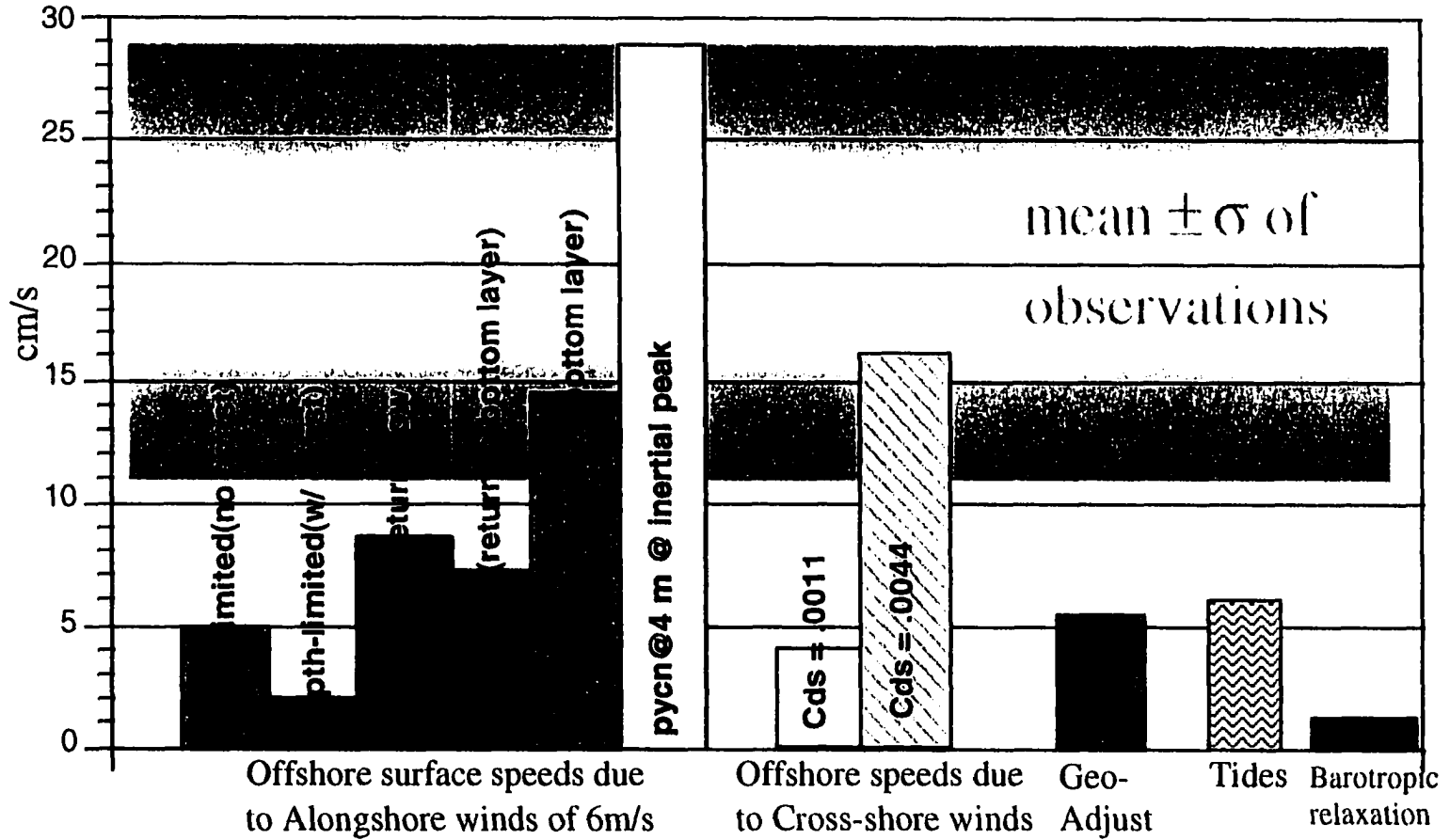


Figure 5.12. Summary of theoretical offshore velocities.

Figure 5.13. Amplitude of complex demodulated inertial frequency $2\pi/T_{\text{inertial}}$ extracted from cross-shore component of velocity at 4 m from 25-m mooring. Bars mark times of plume separations from the coast.

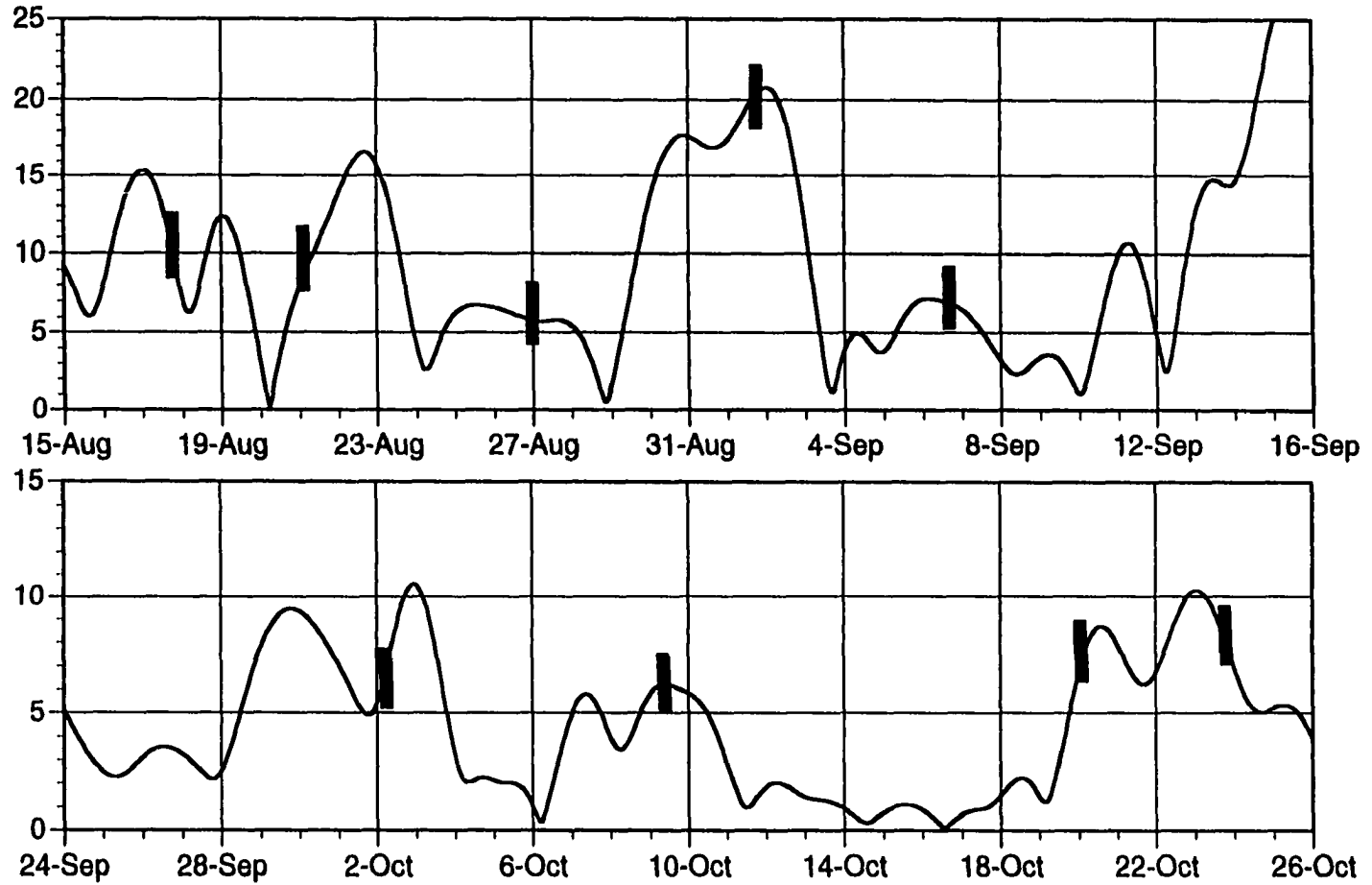


Figure 5.13. Strength of inertial oscillations: amplitude of complex demodulated frequency $2\pi/T_{inertial}$ extracted from across-shore component of velocity at 4 m depth from the 25-m mooring. Bars mark times of plume separations from the coast.

Figure 5.14. Sheared cross-shelf wind-driven flow compared with pressure-gradient flow.

Depth-limited cross-shelf flow due to offshore wind of 6 m/s
(illustrated for constant vertical eddy viscosity)

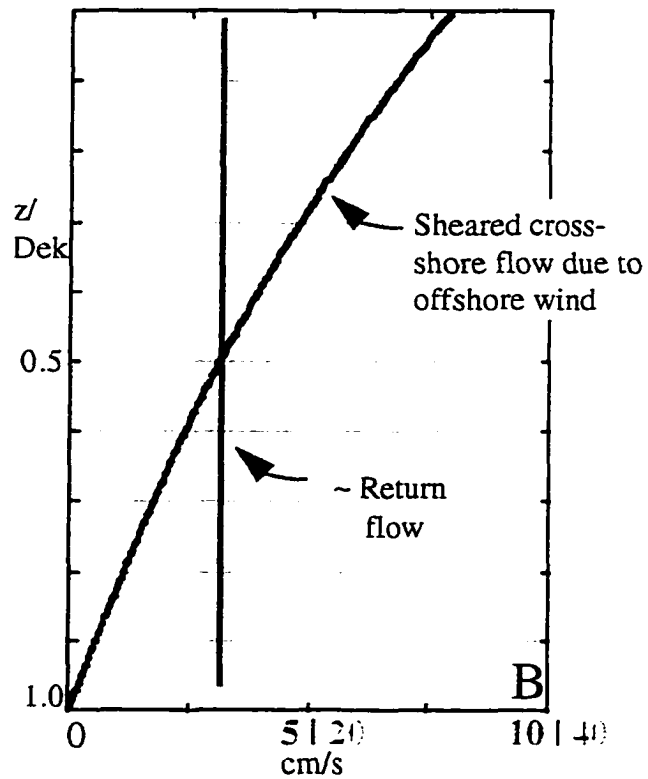


Figure 5.14. Sheared cross-shelf wind driven compared to barotropic pressure-gradient return flow.

(Magnitude for $C_{ds}=0.0011$; Magnitude for $C_{ds}=0.024$)

Figure 5.15. Observed shear *versus* predicted shear due to cross-shore density gradient (thermal wind relationship).

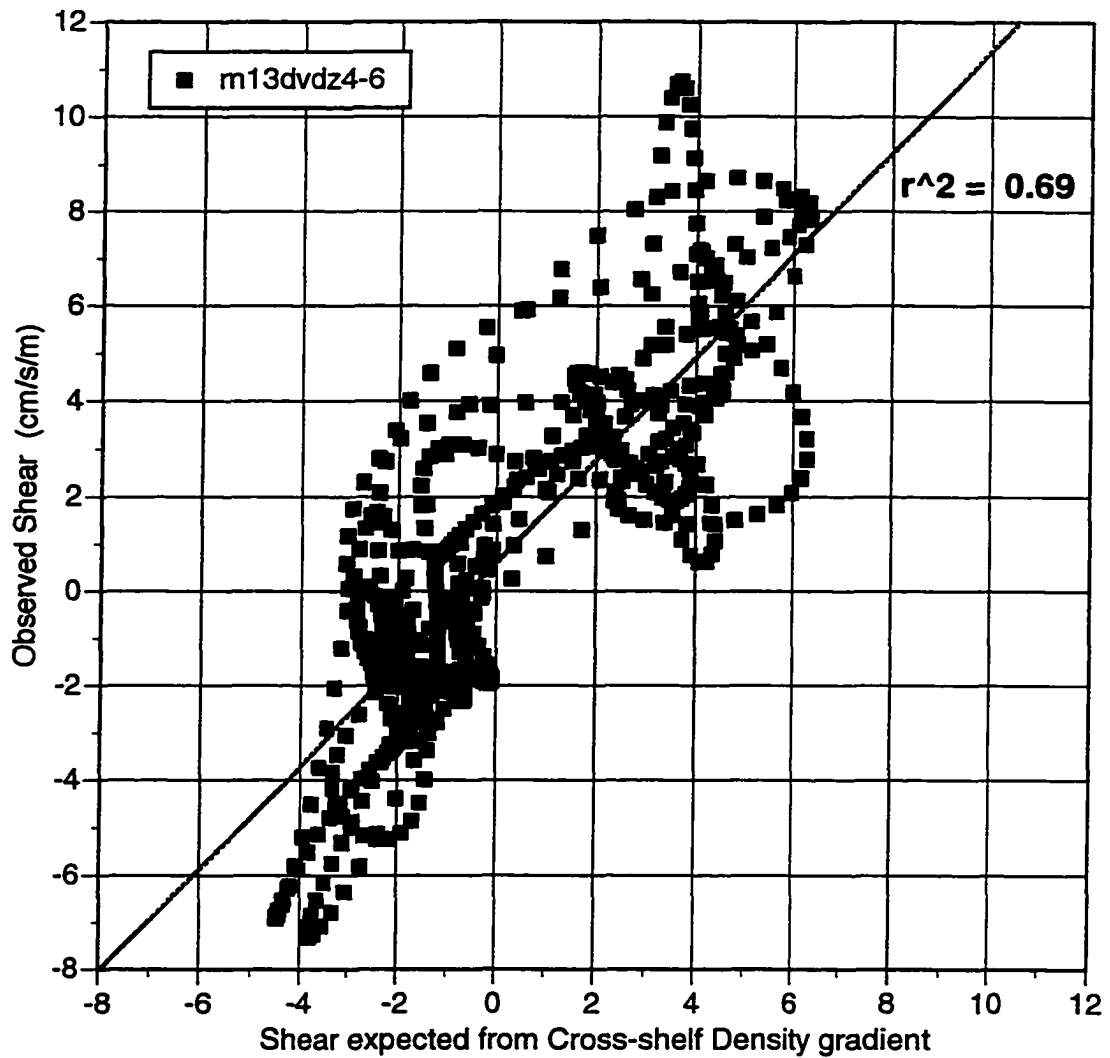


Figure 5.15. Test for geostrophic balance: observed shear at 13-m mooring compared to calculated shear due to cross-shore density gradient.

Figure 5.16. Solid line: The shape of the density front after geostrophic adjustment from an initially vertical position (dashed line) at x_0 . Dotted line : shape of the density front after upwelling-directed wind stress impulse (after Csanady, 1978b).

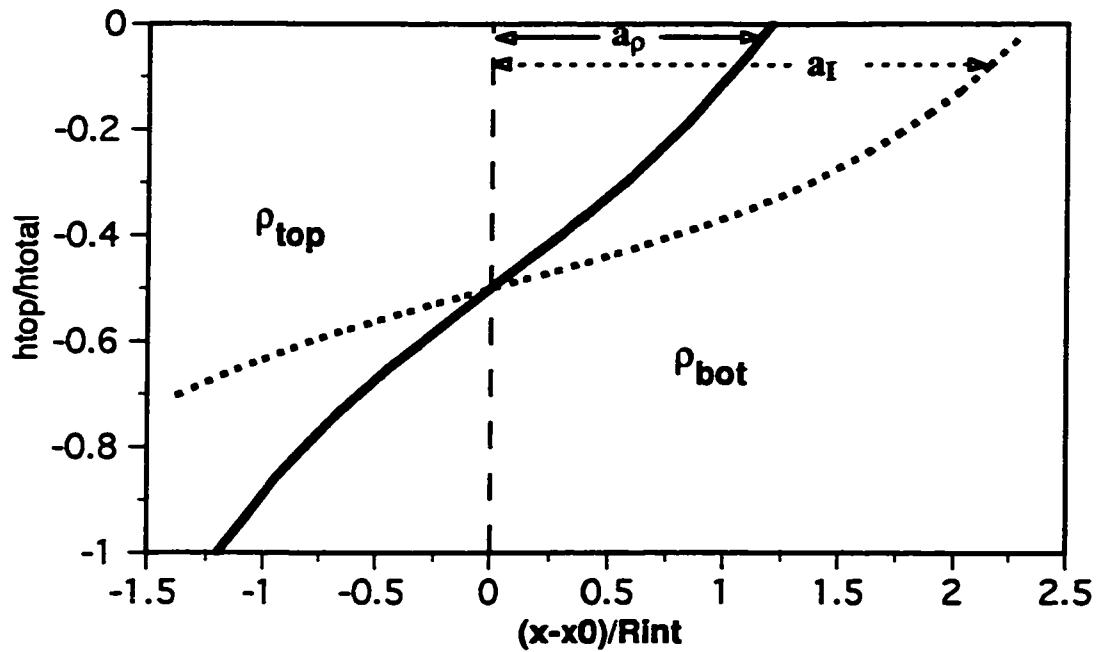


Figure 5.16. Solid line: The shape of the density front after geostrophic adjustment from an initially vertical position (dashed line) at x_0 . Dotted line : shape of the density front after upwelling-directed wind stress impulse (after Csanady, 1978).

Chapter 6. Synopsis

The characteristics and effects of intrusions of estuarine outflow along the inner shelf have been examined, based on hydrographic and meteorological observations from the late summer and autumn of 1994 obtained during the "Coastal Ocean Processes" (CoOP'94) field experiment sited off the Outer Banks at Duck, North Carolina. A synthesis of moored and ship-based measurements reveal the intermittent passage of distinct low salinity intrusions issuing from the Chesapeake Bay that initially travel southward down the coastline. These plumes of fresher water were observed every 2 to 8 days, remaining in the study area for 1 to 4 days. Under the influence of upwelling winds, these low salinity water masses were seen to spread offshore, separating from the coast to form shallow lenses of fresher water that eventually mixed away. The salinity of the ambient shelf water was decreased by 2 psu over the 3 month study.

6.1 Along-coast Propagation

The arrival of an intrusion was observed as a sudden decrease in salinity of between 1 and 4.5 psu in less than an hour. The density deficit between the average plume and the shelf water was between 2 and 3 kg m⁻³, and was due entirely to the difference in salinity, with no contribution from temperature. Analysis of the successive times of arrival of the low

salinity water masses at salinity sensors moored north to south along the inner shelf allowed the determination of the along-coast propagation speeds of the intrusions. When corrected for the ambient shelf flow, these propagation speeds averaged 38 cm/s, about three-quarters of the theoretical linear internal wave phase speed based on the average density difference.

The plumes were thicker towards the coast and thinned farther out. The underlying pycnocline surfaced approximately 9 km offshore and created a sharp front that was frequently visible to shipboard observers. The shape of the plume was strongly controlled by the wind: during upwelling winds the plume thinned vertically and widened offshore; while downwelled plumes were deep and confined to near the coast. However, the plumes influenced by strong downwelling wind stress (magnitude >0.15 Pa) contacted the bottom and displayed different behavior, propagating much more slowly and widening offshore.

The low salinity intrusion sets up a baroclinic coastal current, accelerating strong southward currents in the surface waters inshore of the 20-m isobath. High horizontal velocity shears were observed across the offshore front. The cross-shore flows inshore of this front were quite different from those just offshore, as the up- or downwelling inner shelf circulation patterns were interrupted by the imposition of the plume's strong vertical stratification. In spite of this stratification, the dilution observed during the plumes' passage through the study region indicate that about half the plumes' volume was exchanged with the ambient water. This portion of the estuarine water, and its associated nutrients and biota, is delivered to the inner shelf within 10 km of the coastline throughout a region extending over 100 km south of the source estuary,

the Chesapeake Bay. The remaining part of the estuarine outflow is mixed with the shelf waters as the plumes disperse offshore.

The innermost shelf was subject to the influence of low salinity water up to half the time during this study. The frequent presence of the plumes' baroclinic coastal current increased the net southward flow of the surface waters within 5 km of the coast to over 14 cm/s, whereas farther offshore the net flow was only 6 cm/s to the south. The proximity of such different flow regimes within relatively small spatial scales could be of importance to the biology in the region, where inner shelf larvae may manipulate their behavior to exploit the contrasting environments.

6.2 Source Variability

The episodic nature of the observed intrusions invited an exploration of possible mechanisms for pulsed outflow from the Chesapeake Bay on the time scale of several days to a week. Estimates of barotropic Bay/shelf exchange, as derived from temporal variations of waterlevel measurements within the Bay, exhibited strongly peaked or surge-like fluxes occurring every 3 to 4 days, which preceded most low salinity intrusions observed off the North Carolina coast by an average of 1.1 days.

Two approaches for the meteorological control of these exchanges were considered: the rise or fall of coastal sea level due to the down- or upwelling conditions over the shelf; and the direct forcing of set up or set down within the estuary by local winds. Through a simple modeling exercise, the Chesapeake Bay was shown to be uniquely situated, given its

basin length, alignment, and regional shelf response, to have these two control mechanisms oppose each other with similar magnitudes, implying a moderated level of barotropic Bay/shelf exchange. The implications of this, contrasted with other basins, may shed some light on the notable characteristics of the Chesapeake Bay region as compared to other estuary systems, and would be an interesting topic of future research.

While the analytical model used here had an over-simplified basin geometry, and an inadequate representation of the effects of bottom friction, it hinted at the complex variation of the volume flux response to varying wind patterns. A frequency analysis of the observations showed that the local set-up responded more effectively to shorter period forcing than did the coastal sea level. The volume flux peaked at a period between 2 and 2.5 days, which was identified as the natural seiche frequency of the Chesapeake basin. The larger outflow peaks in volume flux occurred at times of diminishing northward wind stress; the largest outflows happened when the reversing wind stress direction coincided with the falling edge of a seiche oscillation. The fact that Bay water can be output in concentrated barotropic pulses, rather than only as a continual lower volume surface flow, may be an important contributor to the observed bore-like nature of the intrusions' propagation, and to the gravity currents' ability to disperse the Bay effluent over farther distances downstream.

Several surges out of the Bay were not detected as subsequent low salinity intrusions along the North Carolina inner shelf. It is assumed that they were transported offshore by upwelling winds. Roughly half of the volume of freshwater input gauged from the Bay's tributaries was recorded as freshwater flux through the inner shelf study region: offshore

dispersal in the area closer to the Bay entrance must account for the rest. The question as to whether plume water that had been blown offshore of the Bay mouth could move back onshore and re-establish a coastal current could not be considered with this particular data set. In a very few cases previously separated lenses of plume water were seen to re-coalesce against the coast within the downstream CoOP study area. However, their salinity signal was weakened and no resurrection of the coastal current was discerned. A study designed specifically to examine the plume behavior in the upstream region, such as the recent ONR Chesapeake Outflow Plume Experiment (COPE), will be able to address questions concerning the plume near the mouth.

6.3 Offshore Movement of the Plume

In the last chapter, the mechanisms that cause the plume to spread offshore were considered: tides, density gradients, inertial motions, and, frictional driving by the wind. The wind forcing was determined to be the most important, while the other mechanisms contributed a smaller fraction of the observed offshore translation speeds. Once the intrusion's initial southward momentum, which kept it rotationally trapped against the shore, was overcome, the low salinity water moved offshore very rapidly, although the observed northward winds were very light. An investigation into the theoretical response to the wind forcing showed that, again, the plumes grouped into two dynamical regimes, determined by whether they filled the entire water column, and the wind energy could be transmitted to the bottom, or whether they were vertically stratified.

The structure of the solutions to a steady balance between friction and rotation, based on the different bottom boundary conditions, was contrasted. The motion anticipated by the theory for such small surface stresses was close to those recorded only for an extremely thin, highly stratified layer. This seems compatible with the shallow lenses that were formed by the separating plume. However, it appeared that a combination of the other forcing mechanisms, acting together in the same direction as the wind, would be required to explain the full offshore motion observed.

The presence of low salinity intrusions from the Chesapeake Bay are revealed to be an important influence on the inner shelf processes along the coast of North Carolina. The results were obtained during the late summer and early fall, when freshwater input to the Bay is at its annual minimum: spring and early summer conditions on the inner shelf would be subject to an increased volume of low salinity water. The offshore front formed by the surfacing of the plumes' pycnocline partially segregates the flow regime of the innermost shelf from that just offshore. This front is a region of high horizontal gradients, not only of salinity, but also of currents and stratification. The resulting gradients in bottom stress and vertical transport will be important in determining the small-scale patterns of such processes as sediment transport and biological distribution on the inner shelf.

LITERATURE CITED

- Alessi, C. A., S.J. Lentz, and J. Austin (1996) Coastal ocean processes Inner-shelf study: Coastal and moored physical oceanographic measurements, Woods Hole Oceanographic Institute Technical Report WHOI-96-06, Woods Hole, Ma., 154pp.
- Allen, J.S. (1980) Models of wind-driven currents on the continental shelf. *Annual Review of Fluid Mechanics*, 12, 389-433.
- Austin, J.A., and S.J. Lentz (1998) The relationship between synoptic weather systems and meteorological forcing on the North Carolina inner shelf. Submitted to *Journal of Geophysical Research*.
- Beardsley, R.C. and J. Hart (1978) A simple theoretical model for the flow of an estuary onto a continental shelf, *Journal of Geophysical Research* 83(C2), 873-883.
- Beardsley, R.C. and C.D. Winant (1979) On the mean circulation in the Mid-Atlantic Bight. *Journal of Physical Oceanography*, 9(1), 612-618.
- Beardsley, R.C. and W.C. Boicourt (1981) On estuarine and continental shelf circulation in the Middle Atlantic Bight. *Evolution of Physical Oceanography*, B.A. Warren and C. Wunsch, Eds., The MIT Press, 233pp.
- Benjamin, T.B. (1968) Gravity currents and related phenomena. *Journal of Fluid Mechanics*, 31, 209-248.
- Berger, T.J., P. Hamilton, R.J. Wayland, J.O. Blanton, W. C. Boicourt, J. H. Churchill, and D. R. Watts (1995) A Physical Oceanographic Field Program Offshore North Carolina, Final Synthesis Report. OCS Study MMS 94-0047. U.S. Department of the Interior, Minerals Management Service, Gulf of Mexico OCS Region, New Orleans, La. 345pp.
- Boicourt, W.C. (1973) The circulation on the continental shelf from Chesapeake Bay to Cape Hatteras. Ph.D. dissertation, The John Hopkins University, Baltimore, Md. 183pp.
- Boicourt, W.C. and P.W. Hacker (1976) Circulation on the Atlantic continental shelf of the United States, Cape May to Cape Hatteras. *Mem.Soc. Roy. Sci. Liege*, 6 (10), 187-200.

Boicourt, W. C., S.-Y. Chao, H.W. Ducklow, P.M. Glibert, T.C. Malone, M.R. Roman, L.P. Sanford, J.A. Fuhrman, C. Garside, and R.W. Garvine. (1987) Physics and Microbial Ecology of a Buoyant Estuarine Plume on the Continental Shelf. *Eos, Trans. AGU* 68(31), 666-668.

Blanton, J.O. and L.P. Atkinson (1983) Transport and fate of river discharge on the continental shelf of the southeastern United States. *Journal of Geophysical Research*, 88, 4705-4718.

Britter, R.E. and J.E. Simpson (1978) Experiments on the dynamics of a gravity current head. *Journal of Mechanics*, 88, 209-248.

Bue, C. D. (1968) Monthly surface-water inflow to the Chesapeake Bay. USGS technical report. Water Resource Division, arlington, VA.

Butman, C.A. (1994) CoOP: Coastal Ocean Processes Study. Sea Technology, January 1994, 44-49.

Campbell, J.W. and J.P. Thomas, editors (1981) Chesapeake Bay Plume Study: Superflux 1980. NASA Conference Publication 2188. NOAA/NEMP III 81 ABCDFG 0042.

Carr, M.T. and S. J. Lentz (1996) Modeling the M2 tide on the continental shelf off the Outer Banks, North Carolina. Woods Hole Oceanographic Institute Technical Report WHOI-96, Woods Hole, Ma., 27pp.

Chao, S.-Y. and W. C. Boicourt (1986) Onset of estuarine plumes. *Journal of Physical Oceanography*, 16(12), 2137-2149.

Chao, S.-Y (1987) Wind-driven motion near inner shelf fronts. *Journal of Geophysical Research*, 92(C4), 3849-3860.

Chao, S.-Y (1988a) River-forced estuarine plumes. *Journal of Physical Oceanography*, 18(1), 72-88.

Chao, S.-Y (1988b) Wind-driven motion of estuarine plumes. *Journal of Physical Oceanography*, 18(1), 1144-1166.

Chapman, D. C., and S.J. Lentz, 1994. Trapping of a coastal density front by the bottom boundary layer. *Journal of Physical Oceanography*, 24, 1464-1479.

Chuang, W-S. and Boicourt, W.C. (1989) Resonant seiche motion in the Chesapeake Bay, *Journal of Geophysical Research*, 94(C2), 2105-2110.

- Crepon, M. (1967) *Hydrodynamique marine en regime impulsional*. *Cah. Oceanogr.* 19, 847-880.
- Cronin, W.B. (1971) Volumetric, areal, and tidal statistics of the Chesapeake Bay estuary and its tributaries. Special Report 20 71-2, Chesapeake Bay Institute, The Johns Hopkins University.
- Csanady, G.T. (1976) The coastal jet conceptual model in the dynamics of shallow seas. *The Sea*, vol. 6, John Wiley, New York, 117-143.
- Csanady, G.T. (1977) Intermittent 'full' upwelling in Lake Ontario. *Journal of Geophysical Research*, 82(C3), 397-419.
- Csanady, G.T. (1978a) The arrested topographic wave. *Journal of Physical Oceanography*, 8, 47-62.
- Csanady, G.T. (1978b) Wind effects on surface to bottom fronts. *Journal of Geophysical Research*, 83(C9), 4633-4640.
- Csanady, G.T. (1982) *Circulation in the Coastal Ocean*. Dordrecht, D.Reidel. 279pp.
- Cushman-Roisin, B. (1985) Conditions for interface surfacing, upper bounds on extent of ventilation and formation of bottom lenses above topography. *Journal of Geophysical Research*, 90(C1), 889-894.
- Cushman-Roisin, B. (1994) *Introduction of Geophysical Fluid dynamics*. Prentice-Hall, New Jersey. 320pp.
- de Ruiter, W.P.M., A. van der Giessen and F.C. Groenendijk (1992) Current and density structure in the Netherlands coastal zone. In: *Dynamics and exchanges in estuaries and the coastal zone*, D. Prandle, ed. Vol 40. *Coastal and Estuarine studies*, Springer-Verlag, New York, 529-550.
- Ekman, V.W. (1905) On the influence of the earth's rotation on ocean currents. *Ark. Mat. Astron. Fys.* 2(11):1.
- Elliott, A.J. and D.P. Wang (1978) The effect of meteorological forcing on the Chesapeake Bay: the coupling between an estuarine system and its adjacent coastal waters. pp 127-145 in J.C. Nihoul, ed. *Hydrodynamics of estuaries and fjords*, Elsevier, Amsterdam.
- Fisher, C.W. (1986) *Tidal circulation in Chesapeake Bay*. Ph D. Dissertation. Old Dominion University. 255pp.

Friedrichs, C.T., L.D. Wright (1997) Wave effects on inner shelf wind drag coefficients. Proceedings of Waves'97 ASCE Third International Symposium of Ocean Wave Measurements and Analysis, B. Edge, ed.

Frizzell-Makowski, L.J. (1996) Temporal variability of the pycnocline in the mid-Chesapeake Bay. Ph D. dissertation, School of Marine Science, College of William and Mary. 121pp.

Fofonoff, N., and R. Millard, (1983) Algorithms for computation of fundamental properties of seawater, UNESCO technical papers in marine science 44, UNESCO.

Garvine, R.W. (1995) A dynamical system for classifying buoyant coastal discharges. *Continental Shelf Research*, 15(13), 1585-1596.

Garvine, R.W. (1974) Physical features of the Connecticut River outflow during high discharge. *Journal of Geophysical Research*, 79(C2), 831-846.

Garvine, R.W. (1982) A steady state model for buoyant surface plumes in coastal waters, *Tellus*, 34, 293-306.

Garvine, R.W. (1985) A simple model of estuarine subtidal fluctuation forced by local and remote wind stress. *Journal of Geophysical Research*, 90, 11945-11948.

Garvine, R.W. (1987) Estuary plumes and fronts in shelf waters: a layer model. *Journal of Physical Oceanography*, 17, 1877-1896.

Garvine, R.W. (1996) Buoyant discharge on the inner continental shelf: a frontal model. *Journal of Marine Research*, 54, 1-33.

Geernaert, G.L., S.E. Larsen, and F. Hansen (1987) Measurements of the wind stress, heat flux, and turbulence intensity during storm conditions over the North Sea. *Journal of Geophysical Research*, 92, 13127-13139.

Geyer, W.R., R.C. Beardsley, J. Candela, M. Castro, R.V. Legeckis, S.J. Lentz, R.Limeburner, L.B.Miranda, and J.H.Trowbridge (1991) The physical oceanography of the Amazon outflow. *Oceanography*, 4(1), 8-14.

Gill, A.E. and E.H. Schumann (1974) The generation of long shelf waves by the wind. *Journal of Physical Oceanography*, 4, 83-90.

Gill, A.E. (1976) Adjustment under gravity in a rotating channel. *Journal of Mechanics*, 77, 603-621.

Goodrich, D.M (1988) On Meteorologically Induced Flushing in Three U. S. East Coast Estuaries. *Estuarine, Coastal and Shelf Science*, **26**, 111-121.

Griffiths, R.W., and E. J.Hopfinger (1983) Gravity currents moving along a lateral boundary in a rotating fluid. *Journal of Fluid Mechanics*, **134**, 357-399.

Hill, A.E. and J.H. Simpson (1988) Low-frequency variability of the Scottish Coastal Current. *Estuarine, Coastal and Shelf Science*, **27**, 163-180.

Kao, T.W., C. Park and H-P. Pao (1977) Buoyant surface discharge and small-scale oceanic fronts: a numerical study. *Journal of Geophysical Research*, **82**(C12), 1747-1752.

Kao, T.W. (1978) Surface intrusion, fronts and internal waves: a numerical study. *Journal of Geophysical Research*, **83**(C9), 4641-4650.

Kourafalou, V.H., L-Y. Oey, J.D. Wang, and T.N. Lee (1996) The fate of river discharge on the continental shelf 1. Modeling the river plume and the inner shelf coastal current. *Journal of Geophysical Research*, **101**(C2), 3415-3434.

Krauss, W. (1973) Dynamics of the homogeneous and quasi-homogenous ocean., Vol. 1. Gebruder Borntraeger, Berlin.

Large, W.G. and S. Pond (1981) Open ocean momentum flux measurements in moderate to strong winds. *Journal of Physical Oceanography*, **11**(1), 324-336.

Largier, J.L., C. Greengrove, S. Rennie, and J. Brubaker (1998) Regional hydrography of the southern Mid-Atlantic Bight. In preparation.

Largier, J.L., and K. S. Millikan (1996) Coastal Ocean Processes (CoOP) Pilot project data report: August-October 1994, R/V Moby Duck CTD and underway data. SIO Reference series N0.96-29, Scripps Institution of Oceanography, Center for Coastal Studies, LaJolla, Ca.

Lentz, S.J. (1995) Sensitivity of the inner-shelf circulation to the form of the eddy viscosity profile. *Journal of Physical Oceanography*, **25**(1) 19-28.

Lentz, S.J. and R. Limeburner (1995) The Amazon river plume during AMASSEDS: spatial characteristics and salinity variability. *Journal of Geophysical Research*, **100**(C2) 2355-2375.

Lentz, S.J., T. Herbers, R. Guza, F. Federson, and S. Elgar (1998) Momentum balances on the North Carolina inner shelf. Submitted to Journal of Geophysical Research.

Luketina, D.A. and J. Imberger (1987) Characteristics of a surface buoyant jet. Journal of Geophysical Research, 92(C5), 5435-5448.

Madsen, O.S (1977) A realistic model of the wind-induced Ekman boundary layer. Journal of Physical Oceanography, 7, 248-255.

Mitchum, G.T., and A.J. Clarke (1986) The frictional nearshore response to forcing by synoptic scale winds. Journal of Physical Oceanography, 16, 934-946.

Mooers, C., J. Fernandez-Partagas, and J. Price (1976) Meteorological forcing fields of the New York Bight (First Year), Technical Report TR76-8, Rosenstiel School of Marine and Atmospheric Science, University of Miami.

Munchow, A., and R.W. Garvine (1993a) Buoyancy and wind forcing of a coastal current. Journal of Marine Research, 51, 293-322.

Munchow, A., and R.W. Garvine (1993b). Dynamical properties of a buoyancy-driven coastal current. Journal of Geophysical Research, 98, 20063-20077.

Noble, M. and B. Butman (1979) Low-frequency wind-induced sea level oscillations along the east coast of North America. Journal of Geophysical Research, 84, 3227-3236.

Noble, M., B. Butman and E. Williams (1983) On the longshelf structure and dynamics of subtidal currents on the eastern United States continental shelf. . Journal of Physical Oceanography, 13, 2125-2147.

O'Donnell, J. (1988) A numerical technique to incorporate frontal boundaries in two-dimensional layer models of ocean dynamics. . Journal of Physical Oceanography, 18, 1584-1600.

Oey, L-Y., and G.L. Mellor, (1993) Subtidal variability of estuarine outflow, plume, and coastal current: a model study. Journal of Physical Oceanography, 23, 164-171.

Ou, Hsien Wang (1984) Wind-driven motion near a shelf-slope front. Journal of Physical Oceanography, 14, 985-993.

- Pettigrew, N.R. (1981). The dynamics and kinematics of the coastal boundary layer off Long Island. Ph.D. thesis, 262pp. Mass. Inst. of Technology and the Woods Hole Oceanographic Inst., Cambridge, MA.
- Pritchard, D.W. (1956) The dynamic structure of a coastal plain estuary. *Journal of Marine Research*. 13:133-144.
- Pond, S. and G. Pickard (1983) *Introductory Dynamical Oceanography*, 2nd edition. Pergamon Press. 329 pp.
- Rey, F. (1981) The development of the spring phytoplankton outburst at selected sites off the Norwegian coast. In *The Norwegian coastal current*, Vol. 2. R.Saetre and M. Mork, ed. University of Bergen Press, Bergen, pp.649-680.
- Ruddick, K.G., E. Deleersnijder, P.J. Luyten and J. Ozer (1995) Haline stratification in the Rhine-Meuse freshwater plume: a three-dimensional model sensitivity analysis. *Continental Shelf Research*, 15(13), 1597-1630.
- Shay, L K., S. J. Lentz, H.C. Graber, and B.K. Haus (1997) Current structure variations detected by high frequency radar and vector measuring current meters, *Journal of Atmospheric and Oceanic Technology*, submitted.
- Simpson, J.H., W.G. Bos, F. Schirmer, A.J. Souza, T.P. Rippeth, S. A. Jones and D. Hydes (1993) Periodic stratification in the Rhine ROFI in the North Sea, *Oceanologica Acta*, 16, 23-32.
- Stern, M.E., J.A. Whitehead and B.-L. Hua (1982) The intrusion of a density current along the coast of a rotating fluid. *Journal of Fluid Mechanics*, 123, 237-265.
- Stommel, H. and A. Leetma (1972) Circulation on the continental shelf. *Proceedings of the National Academy of Science*, 69(11) 3380-3384.
- Stumpf, R.P., G. Gelfenbaum and J.R. Pennock (1993) Wind and tidal forcing of a buoyant plume, Mobile Bay, Alabama. *Continental Shelf Research*, 13(131), 1281-1301.
- USGS (1994). United States Geological Survey estimated streamflow entering Chesapeake Bay, *Monthly Summaries*, 8600 LaSalle Rd, Towson, Maryland.
- Valle-Levinson, A., J.L. Miller, M. Paraso (1994). *Monthly Hydrography in the Lower Chesapeake Bay, 1994 Technical Report 95-03*, Center for Physical Oceanography, Norfolk, VA.

Valle-Levinson, A. and K.M.M. Lwiza (1995) Effects of channels and shoals on the exchange between the lower Chesapeake Bay and the adjacent ocean, *Journal of Geophysical Research*, **100**(C9), 18,551-18,563.

Valle-Levinson, A. (1995). Observations of barotropic and baroclinic exchanges in the lower Chesapeake Bay. *Continental Shelf Research*, **15**(13), 1631-1647.

Wang, D-P. (1979) Subtidal sea level variations in the Chesapeake Bay and relations to atmospheric forcing. *Journal of Physical Oceanography*, **9**, 413-421.

Waldorf, B.W., J.L. Largier, S. Rennie, J. Austin, C. Greengrove (1995) Coastal Ocean Processes (CoOP) Pilot Project Data Report: R/V Cape Hatteras Shipboard Measurements; Underway, CTD, and ADCP Data, August 1994, SIO Reference Series No.95-29, Scripps Institution of Oceanography, Center for Coastal Studies, LaJolla, Ca. 419pp.

Waldorf, B.W., J.L. Largier, S. Rennie, J. Austin (1996) Coastal Ocean Processes (CoOP) Pilot Project Data Report: R/V Cape Hatteras Shipboard Measurements; Underway, CTD, and ADCP Data, October 1994, SIO Reference Series No.96-9, Scripps Institution of Oceanography, Center for Coastal Studies, LaJolla, Ca. 407pp.

Wright, L.D. and J.M. Coleman (1971) Effluent expansion and interfacial mixing in the presence of a salt wedge, Mississippi River delta. *Journal of Geophysical Research*, **76**, 8649-8661.

Wong, K.-C. and R.W. Garvine (1984) Observations of wind-induced, subtidal variability in the Delaware Estuary. *Journal of Geophysical Research*, **89**, 10589-10598.

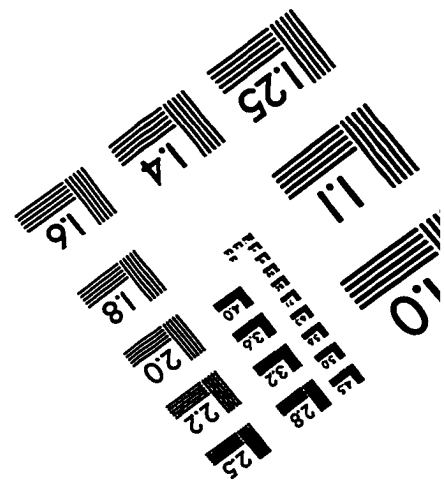
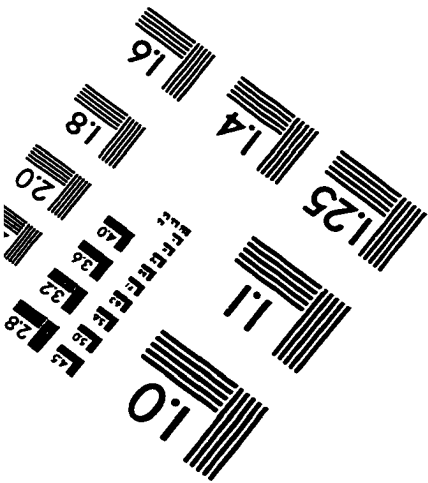
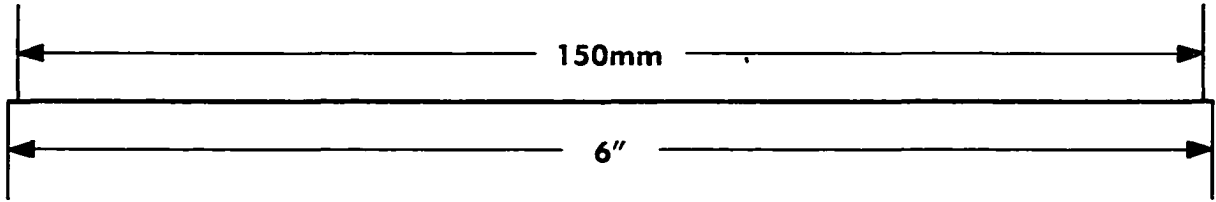
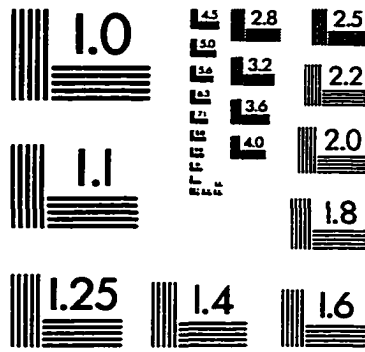
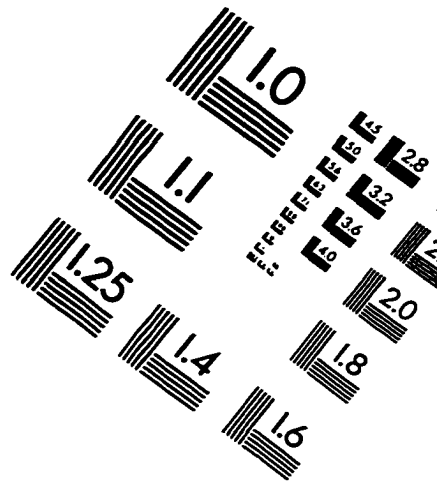
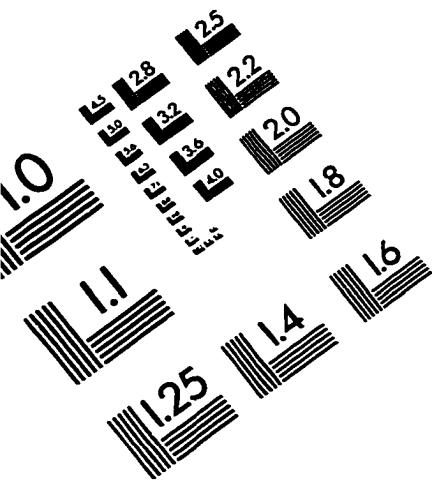
Yankovsky, A. E. and D. C. Chapman (1997) A simple theory for the fate of buoyant coastal discharges. Submitted to *Journal of Physical Oceanography*.

VITA

Sarah Elizabeth Rennie

Born at West Point Military Academy, New York on 6 October, 1955. Graduated from John Marshall High School, Richmond, Virginia in June, 1973. Received a B.A. *Magna cum Laude* in Mathematics and English from Williams College, Williamstown, Massachusetts in May, 1977 and a M.S. in Computer Science from Columbia University in the City Of New York in May, 1979. Was employed for nine years as a programmer/analyst at Lamont-Doherty Geological Observatory in the Physical Oceanography research group. Entered the Ph.D. program in the Physical Oceanography Department at Virginia Institute of Marine Science, School of Marine Science at the College of William and Mary in Virginia in September, 1991. Currently employed at the Johns Hopkins University Applied Physics Laboratory.

IMAGE EVALUATION TEST TARGET (QA-3)



APPLIED IMAGE . Inc
1653 East Main Street
Rochester, NY 14609 USA
Phone: 716/482-0300
Fax: 716/288-5989

© 1993, Applied Image, Inc., All Rights Reserved